August 2021

Electromagnetic Transitions and Beta Decays in Nuclei from the Ab initio Symmetry-adapted No-core Shell Model

Grigor Sargsyan
Louisiana State University and Agricultural and Mechanical College

ELECTROMAGNETIC TRANSITIONS AND BETA DECAYS IN NUCLEI FROM THE *AB INITIO* SYMMETRY-ADAPTED NO-CORE SHELL MODEL

A Dissertation

Submitted to the Graduate Faculty of the
Louisiana State University and
Agricultural and Mechanical College
in partial fulfillment of the
requirements for the degree of
Doctor of Philosophy

in

The Department of Physics and Astronomy

by
Grigor Sargsyan
B.S. Physics, Yerevan State University, 2014
December 2021

Acknowledgments

This thesis work would not be possible without the help of a number of people who have guided, supported, listened and inspired me during the past six years, and I am truly grateful to them.

First of all, I would like to thank my advisor Kristina Launey, who has been incredibly helpful in every aspect of my research. All of this Acknowledgements section cannot even compare to the amount of encouragement that she has given me throughout my studies. Thank you for being the best advisor I could ask for. I am also indebted to Tomas Dytrych for all the help with the software development and Jerry Draayer for his constant support and giving me the opportunity to work with the nuclear theory group at LSU before my PhD program. I owe thanks to the other members of my committee, Ilya Vekhter, Anton Zeitlin, and in particular to Scott Marley for invaluable discussions and the collaboration on one of my main projects. I also want to acknowledge my funding sources (NSF, SURA) and computational resources (LSU HPC, Blue Waters, NERSC, Frontera).

LSU professors I would like to thank include Jorge Pullin for some of the most compelling lectures I have ever attended, Catherine Deibel, for teaching me about nuclear physics, and Ravi Rau for the many discussion on broader physics topics. In particular, the informal lunch seminars for graduate students organized by Dr. Rau (commonly known as "Rau lunch") will stay as some of the brightest memories I have from my years as a Ph.D. student. I further thank my undergraduate physics professors, Anahit Balabekyan, Romen Grigoryan, Vasili Tsakanov and Razmik Margaryan for setting the basis of my nuclear physics knowledge.

A great deal of credit goes to my collaborators from LLNL, Mary Burkey, Aaron Galant and Nick Scielzo, who have had a major contribution to the success of one of my main projects. I am also indebted to Panu Ruotsalainen from the University of Jyvaskyla and Jordan Williams from the Simon Fraser University for my first two collaborations with experimental nuclear physics groups.

The support from my friends back in Armenia and at LSU has been extremely helpful. I

am thankful to my pre-LSU friends, among others, Hakob Petrosyan, Vachik Khachatryan, Torgom Yezekyan, Avag Akopov, and Tigran Ishkhanyan who would always keep in touch with me and happily listen about my work and life far from them. Many fist bumps to my rock-climbing friends, David Alspaugh, Reagan Dugan, Oscar Johnson, Michelle Lis, Frederic Marazzato, Andrew McGuffey, Marisa Myers and Charles Zimmerman onto whom I always could rely for after-work stress-relieving climbing sessions. Further, I am extremely grateful to my previous and current group mates Robert Baker, Alison Dreyfuss, Alexis Mercenne and David Kekejian who have not only been good colleagues, but also excellent friends. Other previous and current graduate students I would like to thank include Sahil Saini, Erin Good, Arshag Danageozian, Tyler Ellis, Sergio Lopez, Graeme Morgan and Alina Prigozhina for being good study and conversation companions. Additionally, Alina deserves a second mention here for her unfailing support over the latter part of my time in graduate school.

Last but definitely not least, many thanks go to my family. To my sisters and their families, who have always cheered for me regardless of success or failure. To my parents, who unquestioningly supported my decision to become a physicist and pursue a doctorate so far away from them. I hope we will be able see each other a lot more often henceforth.

Table of Contents

List of Figures

Abstract

Nuclear physics today is a diverse field, involving research that extends from the minuscule scales of neutrons and protons to the colossal dimensions of astrophysical objects in the universe. And since the *ab initio* methods in nuclear physics use realistic internucleon interactions, nuclear modeling has gained predictive capabilities that enable us to probe ever more deeply into the fundamental nature of matter. One of these models – the symmetry-adapted no-core shell model (SA-NCSM) – is capable of reaching the medium-mass region of the chart of the nuclides, by exploiting the emergent symmetries of nuclei, and is therefore well-suited for studying collective correlations and beta decay modes.

We apply the SA-NCSM to calculate beta-decay observables essential to probe physics beyond the Standard Model. One of the most challenging problems in physics today is whether the neutrino is its own antiparticle. This work sets a limit – from first principles – on the nuclear structure piece needed by experimentalists to extract the type of the neutrino (Dirac or Majorana) from state-of-the-art measurements of the half-life of the hypothetical neutrinoless double-beta decay. Furthermore, our calculations of higher-order recoil terms in the beta decay of ^{8}Li help to significantly reduce the uncertainties in high-precision experiments that study the vector minus axial vector (V$-$A) structure of the weak interaction.

In addition, to gain a better understanding of the ^{8}Li beta-decay final states, we examine their cluster substructures such as the single-nucleon and alpha cluster wavefunctions. The method is then applied to a series of Li isotopes. The single-nucleon cluster wavefunctions are used in calculations of reaction observables, which in turn paves the way for calculations of optical potentials for nucleon projectiles from first principles.

1 Introduction

1.1 Collectivity in nuclei

Nuclei are dynamical systems governed by complex interactions between nucleons. However, from these intricate internucleon interactions emerge collective modes responsible for deformation of nuclei. The *ab initio* symmetry-adapted no-core shell-model (SA-NCSM) [1,2] has indicated the universal presence of deformation-driven collective features in light to medium-mass nuclei from first principles. In particular, only a few collective shapes have been shown to dominate the structure of nuclei and their excited states [2, 3]. Hence, collective observables are vital for benchmark studies to guarantee proper consideration of the physics of nuclear dynamics in *ab initio* modeling.

Electromagnetic observables in nuclei, such as quadrupole moments and quadrupole transition strengths [$B(E2)$ strengths], are often used to probe the collectivity and spin structure of nuclei. To ensure an accurate description of the nuclear structure, we calculate electromagnetic observables in several light to intermediate-mass nuclei using the SA-NCSM. Specifically, since *ab initio* methods are generally limited to light nuclei due to the explosive growth of the computational problem with the number of nucleons in the nucleus, we use a symmetry-adapted basis of the SA-NCSM as it enables us to reach medium-mass nuclei by selecting only physically relevant states in the model space. This strategy allows us to apply *ab initio* methods to some of the most challenging problems in nuclear physics today.

1.2 Neutrinoless double-beta decay

Neutrinos are fundamental particles within the Standard Model of particle physics. They are the only leptons that are electrically neutral, which makes them a good candidate for Majorana fermions (*i.e.*, they are their own antiparticles). The discovery of neutrino oscillations [4] has made the existence of Majorana neutrinos especially compelling. This is closely connected to the problem of whether the lepton number is a conserved quantity in Standard Model processes.

A promising approach for studying the nature of neutrinos is neutrinoless double-beta

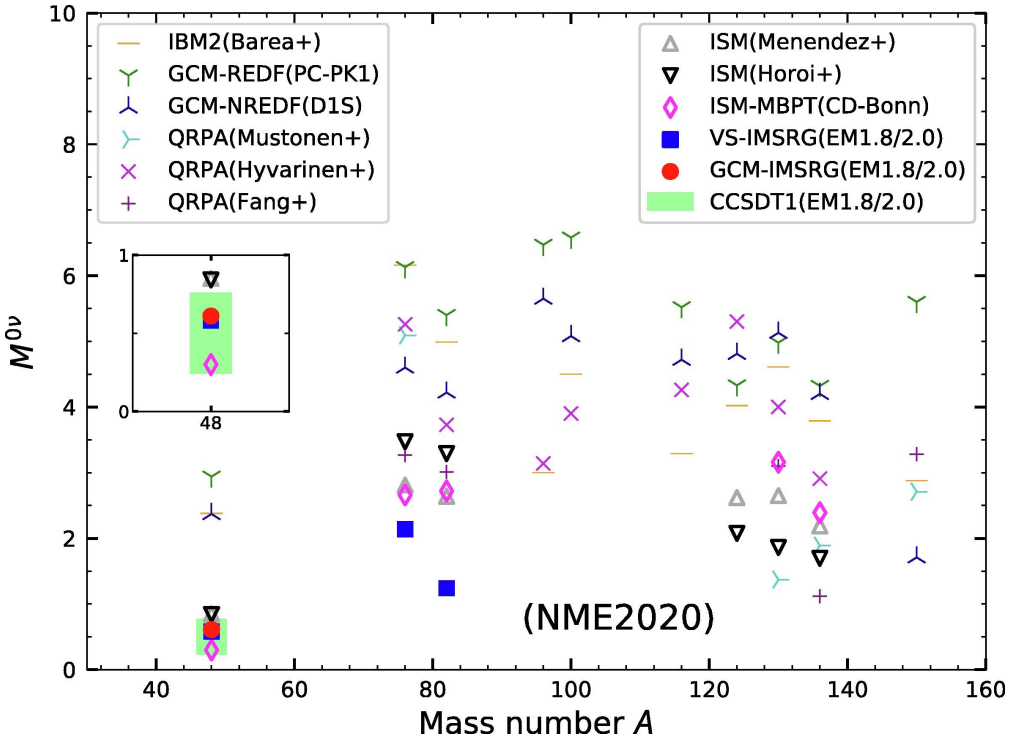

Figure 1.1. Nuclear matrix elements ($M^{0\nu}$) for $0\nu\beta\beta$ decay candidates. The results are obtained from different models: the generator coordinate method relativistic energy-density functional theory (GCM-REDF) [5], the GCM non-relativistic energy-density functional theory (GCM-NREDF) [6], quasiparticle random phase approximation (QRPA) [7–9], the interacting boson model (IBM2) [10], the interacting shell model (ISM) [11, 12], the valence-shell in-medium similarity renormalization group (VS-IMSRG) [13], the GCM-IMSRG [14] and the coupled-cluster theory [15]. Figure adapted from Ref. [16].

decay ($0\nu\beta\beta$). The discovery of this phenomenon and its further study could shed light on some of the most profound questions in nuclear physics, particle physics, astrophysics and cosmology. In particular, the observation of $0\nu\beta\beta$ would provide direct evidence that the neutrinos are Majorana particles, as well as for a beyond-standard-model process that violates lepton number conservation and constrains the neutrino mass scale [17].

Motivated by these implications, a variety of experiments[1] are searching for $0\nu\beta\beta$ using different methods and nuclides. The experiments anticipate measuring the rate of this rare process. However, the $0\nu\beta\beta$ rate depends on both the unknown mass of the Majorana

[1]Examples of currently operating experiments include GERDA II, CUORE and EXO200 collaborations. Some larger scale experiments such as LEGEND, CUPID and nEXO are in a development stage [18].

neutrino and the nuclear matrix element. A number of models have attempted to calculate nuclear matrix elements for various candidates of $0\nu\beta\beta$. Some results of these calculations are presented in Fig. 1.1. There is a significant spread in values from different models, and it has been suggested that all the models could be missing important physics [17].

To offer deeper insight into the nuclear matrix elements of $0\nu\beta\beta$, novel *ab initio* models are essential. Although often constrained to comparatively light nuclei by the exponential growth of the model space with the increasing number of nucleons, *ab initio* models are a powerful tool for studying nuclear properties. Recent preliminary results from *ab initio* studies have indicated the need for further improvements [19]. Namely, while the coupled-cluster theory [20] can provide a successful description of ^{48}Ca, calculating the $0\nu\beta\beta$ rate to ^{48}Ti is extremely challenging; another *ab initio* model, the in-medium similarity renormalization group (IMSRG) [21], uses highly renormalized interactions that might affect the final result. The SA-NCSM can be employed without the need for using effective operators and charges for calculations of the lightest $0\nu\beta\beta$ candidate, ^{48}Ca.

1.3 Beta-decay recoil effects

Another appealing problem related to the conventional beta-decay processes is the existence of tensor currents in the weak interactions. The theory of β decays assumes the vector minus axial vector (V$-$A) nature of interaction to satisfy the observed violation of the conservation of parity. This is embedded in the Standard Model of particle physics. So while the V$-$A theory remains consistent with all data, there remain strong incentives to look for divergences from V$-$A nature in β decays. In short, despite outstanding successes of the Standard Model, for many theoretical reasons, particularly those due to the number of undetermined parameters associated with the models used to describe the underpinning structure, the existence of new physics remains an expectation.

Various extensions to the Standard Model permit scalar, tensor and pseudoscalar interactions to arise [22]. Motivated by this, several experiments attempt to measure the possible effects of those interactions. In a recent experiment on ^{8}Li β decay [23] at Argonne National

Laboratory the upper limit on the tensor coupling constant was set to $|C_T/C_A|^2 < 0.011$, where C_T and C_A are the tensor and axial vector coupling constants. The results were consistent with a purely V−A interaction.

A large portion of uncertainty in the experiment came from so called recoil corrections, arising due to the recoil of the nucleus during the decay. As shown in Ref. [24] and [25] the recoil-order corrections can be theoretically quantified. For A=8 systems *ab initio* models such as SA-NCSM can perform this calculation with high precision which can further refine the limit on the tensor coupling, thus probing the validity of the V−A theory.

1.4 Towards *ab initio* reaction theory

The calculations of β-decay observables are performed between nuclei with differing numbers of protons and neutrons. In many-body calculations similar techniques are used for single-nucleon removal or addition processes such as nucleon knock-out, transfer and radiative capture reactions. These reactions play an important role in our understanding of nucleosynthesis, and how the nuclear matter is produced in the universe. The calculations of single-nucleon cluster wavefunctions are a first step towards the description of reaction observables from many-body theory. We study a series of Li+n cluster systems that are important for astrophysical processes, in particular for the inhomogeneous big bang nucleosynthesis models. Our calculated single-nucleon cluster wavefunctions from the *ab initio* SA-NCSM are used to obtain spectroscopic factors and asymptotic normalization coefficients, and compared to the experimentally deduced results. Furthermore, these wavefunctions open a new path to the construction of nucleon optical potentials ultimately applicable to calculations of reaction cross-sections.

2 Nuclear *Ab initio* Models

2.1 *Ab initio* models and realistic interactions

The microscopic description of nuclear structure appears to be a fairly difficult task, involving sophisticated computations of many-body systems. An early independent particle model (IPM) by Mayer and Jansen, the nuclear shell model [26], had great success in describing properties of certain nuclei. Based on the observation that some especially stable nuclear systems possess so called "magic numbers", it assumes that each of the nucleons is moving independently in an average field created by the interaction of all nucleons. The "magic numbers" according to the model correspond to the filling of specific quantized levels (shells) of the harmonic oscillator (HO) mean field plus a spin-orbit term. Further advancement of the model led to the construction of interacting shell model (the so-called valence shell model), which included interactions between the nucleons in the valence shell. Hence, the nucleons occupying single-particle states derived from the mean field (also referred as a single-particle basis) are divided into two groups: active nucleons in the valence single-particle states that interact with one another, and inert nucleons in the closed shells composing the core (Fig. 2.1a).

A modern version of the nuclear shell model is the *ab initio* no-core shell model (NCSM), which uses HO single-particle basis states and realistic nuclear interactions to reproduce the properties of the light nuclei up through ^{16}O. A nuclear interaction is called realistic if it fits to the nucleon-nucleon scattering data with high precision and perfectly describes the properties of the two-nucleon system, deuteron. In the recent years, much work has been done towards constructing high precision nucleon-nucleon (NN) interactions. Examples of modern NN realistic interactions include CD-Bonn [27] and Nijmegen [28], which are constructed through meson exchange theory, and N3LO [29] derived from chiral effective field theory. Additionally, the theory shows that weaker three-nucleon (3N) forces become necessary for a description of $A > 2$ systems, however, their inclusion results in an explosive growth of computational resources necessary for *ab initio* calculations. In order to overcome this

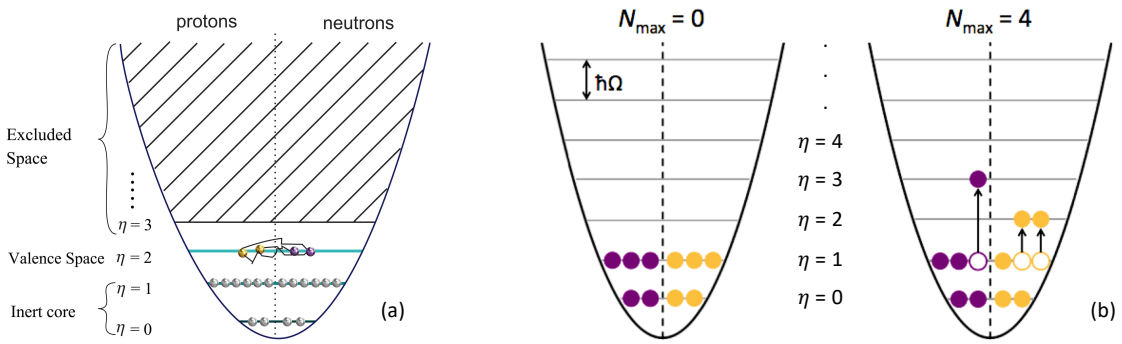

Figure 2.1. (a) Schematic illustration of the interacting shell model, (b) and $N_{\max} = 0$ and $N_{\max} = 4$ configurations in ^{10}B in a standard particle-based NCSM (a single configuration is shown in each case).

difficulty, various interactions that are purely two nucleon have been designed that partially account for 3N effects. Examples of such interactions include JISP16 [30], INOY [31] and NNLO$_{\text{opt}}$ [32]. In addition, the interactions are often renormalized ("softened") to ensure fast convergence of the low-lying eigenstates with an increase in the model space size. There are various techniques of renormalization such as Okubo-Lee-Suzuki (OLS) [33,34] and Similarity Renormalization Group (SRG) [35]. In short, these techniques transform the two-body (or three-body) Hamiltonian into an effective Hamiltonian for given A that decouples from high-energy physics, while preserving the symmetries of the initial Hamiltonian and introducing many-body effective interactions. The NCSM treats all the nucleons in the nucleus as active and limits the excitations of the particles by a so called $N_{\max}$ cutoff – that is the number of allowed HO excitation quanta above the lowest configuration for a given nucleus (Fig. 2.1b). The use of realistic nuclear interactions between the constituent protons and neutrons gives the model predictive power. Nevertheless, the model space in NCSM grows combinatorially with an increasing $N_{\max}$ cutoff and the nucleon number, thus limiting it to comparatively light nuclei.

2.2 The symmetry-adapted no-core shell model framework

The early work by Bohr and Mottelson [36] showed that deformed modes seemed to dominate the nuclear dynamics, which in turn suggested that a natural description of nuclei

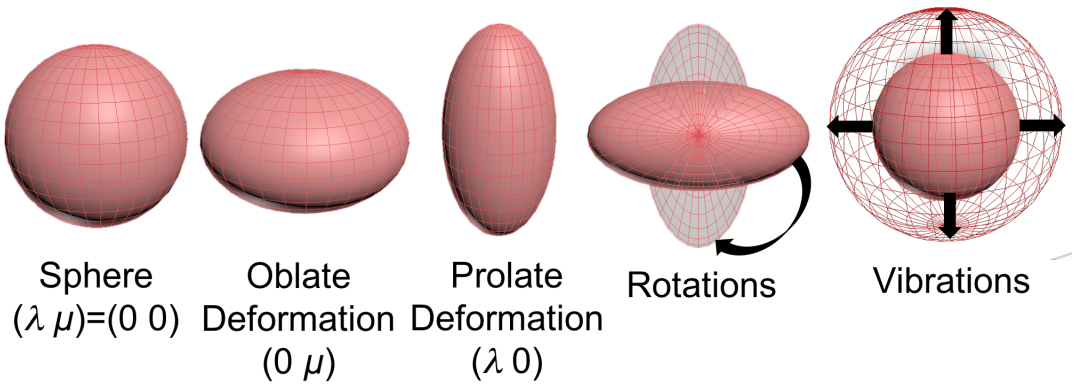

Figure 2.2. The SA-NCSM configurations that describe different equilibrium shapes, given by the SU(3) $(\lambda\,\mu)$ quantum numbers, together with their rotations and vibrations with respect to the center-of-mass-free laboratory frame.

should include shapes and the associated symmetries. And indeed, the symmetry-adapted no-core shell model (SA-NCSM) enhances the NCSM theory by choosing a basis states that reflect the importance of these special features. Unlike the NCSM, the growth of the model space in this case can be controlled by selecting only physically relevant states.

The symmetry groups used in the SA-NCSM are the SU(3) $\subset$ Sp$(3,\mathbb{R})$ groups, which are used to describe the transformations, rotations and vibrations, that preserve an equilibrium deformation (Fig. 2.2). The SU(3) group is also known to be the foundation of the successful Elliott microscopic model [37,38]. In both models, the excitations of the particles in the three dimensional HO basis in each x, y and z direction are given in terms of SU(3) $(\lambda\mu)$ quantum numbers, where λ shows the excess in z direction as compared to y and μ shows the excess in y direction as compared to x, *i.e.*, $\lambda = n_z - n_y$ and $\mu = n_y - n_x$, where n_x, n_y and n_z are HO quanta along the three respective Cartesian directions and $N = n_x + n_y + n_z$ is the total number of HO quanta (Fig. 2.2). The $(\lambda\mu)$ pairs label irreducible representation (irreps) of the SU(3) group. An example for an irrep of the familiar SO(3) group is the smallest set of states transforming among themselves under rotations.

A subgroup of SU(3) is the rotational group SO(3) with the generators of its elements being the orbital angular momentum operators L. In addition, the angular momentum pro-

jection operator M_L generates the SO(2) group which is a subgroup of SO(3). Consequently, many-body states can be classified according to their transformation properties with respect to the physical group chain

$$\mathrm{SU}(3)_{(\lambda\mu)} \overset{\kappa}{\supset} \mathrm{SO}(3)_L \supset \mathrm{SO}(2)_{M_L},$$

where κ distinguishes between multiple occurrences of the same orbital momentum L in a general irrep $(\lambda\mu)$. Thus, the set $\{N(\lambda\mu)\kappa(LS)JM\}$ labels an SU(3)-scheme basis state, with $J = L \oplus S$ being the total angular momentum and M being its projection. We should note, that this labeling scheme does not differentiate between protons and neutrons, and to do this one can introduce the isospin degree of freedom and consider protons and neutrons as different projections of an isospin-1/2 doublet. With this extension the basis state is given by $|N(\lambda\mu)\kappa(LS)JM;TT_z\rangle$, where T and T_z are respectively the total isospin of the system and its projection. In Elliott's model and in SA-NCSM, there are additional quantum numbers, related to particle distributions, that label the complete basis. These basis states are related to the NCSM basis states via a unitary transformation.

The SU(3) model of Elliott uses only valence shell configurations, namely, $N_{\max} = 0$. The higher $N_{\max}$ subspaces containing highly deformed states are neglected. The SU(3) symmetry group is used not only for organizing the many particle states, but also for the construction of the effective internucleon interaction. For the interactions that respect SU(3) symmetries, the model can be solved analytically. Yet, even for SU(3) symmetry-breaking interactions, the results show dominance of only a few most deformed configurations [1].

The symmetry-adapted no-core shell model can be regarded as a multishell ($N_{\max} > 0$) extension of the Elliott SU(3) scheme, allowing nuclear collective states to be expressed in terms of no-core shell-model configurations. The key feature of the SA-NCSM is that the physically relevant model space can be selected, starting from the largest deformation and lowest spin in a small $N_{\max}$ subspace, and add ever smaller deformation until convergence

of results is achieved. It is important to note that in both NCSM and SA-NCSM, the $N_{\max}$ cutoff in the HO basis is essential for removing the center-of-mass excitation from the low-lying spectrum. All observables may then be calculated free of spurious center-of-mass motion contributions. As the SA-NCSM requires large-scale calculations, a code called `LSU3shell` [39] is developed to carry out parallelized calculations on multicore computers.

In the SA-NCSM, the SA basis is constructed using an efficient group-theoretical algorithm for each HO major shell [40]. While we do not use explicit construction of conventional NCSM bases, for completeness, we show the unitary transformation from a two-particle JT-coupled basis state to an SU(3)-coupled state:

$$
\begin{aligned}
|\eta_r \eta_s \omega \kappa (LS) \Gamma M_\Gamma\rangle &= \frac{1}{\sqrt{1+\delta_{\eta_r \eta_s}}} \{a^\dagger_{(\eta_r\, 0)\frac{1}{2}} \times a^\dagger_{(\eta_s\, 0)\frac{1}{2}}\}^{\omega\kappa(LS)\Gamma M_\Gamma} |0\rangle \\
&= \frac{1}{\sqrt{1+\delta_{\eta_r \eta_s}}} \sum_{\substack{l_r l_s \\ j_r j_s}} \Pi_{j_r j_s LS} \langle (\eta_r\ 0) l_r; (\eta_s\ 0) l_s \| \omega\kappa L\rangle \begin{Bmatrix} l_r & l_s & L \\ 1/2 & 1/2 & S \\ j_r & j_s & J \end{Bmatrix} \{a^\dagger_r \times a^\dagger_s\}^{\Gamma M_\Gamma} |0\rangle \,,
\end{aligned}
\tag{2.1}
$$

where we use conventional labels $r(s) = \{\eta(l\,\frac{1}{2})jt = \frac{1}{2}\}$ and $\Gamma = JT$, with $\eta = 0, 1, 2, \ldots$ is the HO shell number and $\Pi_j = \sqrt{2j+1}$, and with $a^\dagger_{(\eta\, 0) l m \frac{1}{2} m_s} \equiv a^\dagger_{\eta l m \frac{1}{2} m_s}$ being the creation operator that creates a particle of spin $\frac{1}{2}$ and orbital momentum l with a projection m in a HO major shell η corresponding to an $|(\eta\, 0) l m\rangle$ state in the SU(3) basis. We use SU(3) quantum numbers, $\omega \equiv (\lambda\, \mu) = (\eta_r\, 0) \times (\eta_s\, 0)$, $\tilde{\omega} \equiv (\mu\, \lambda)$, and κ distinguishes multiple occurrences of the same total orbital momentum L for a given ω. The two states are coupled through reduced SU(3) Clebsch-Gordan coefficients $\langle ; \| \rangle$ [41, 42]. S is the total intrinsic spin of the two particle system and we use Wigner 9-j symbol $\{...\}$.

2.3 NN interactions in SU(3) basis

NN interactions can be divided into components that respect certain symmetries, such as rotational invariance. Two-body isoscalar (charge-independent) interactions are typically

given in a representation of a JT-coupled HO basis, $|rs\Gamma M_\Gamma\rangle$, that is,

$$V^\Gamma_{rstu} = \langle rs\Gamma M_\Gamma = 0|V|tu\Gamma M_\Gamma = 0\rangle\,.$$

This takes advantage of the fact that the interaction transforms as a scalar under rotations in coordinate and isospin space, that is, it is an SO(3)$\times$ SU(2)$_T$ tensor of rank zero ($J_0 = 0, T_0 = 0$).

Analogously, the interaction can be represented in an SU(3)$\times$SU(2)$_S\times$SU(2)$_T$-coupled HO basis $|\eta_r\eta_s\omega\kappa(LS)\Gamma M_\Gamma\rangle$ shown in Eq. (2.1). The corresponding interaction matrix elements are similarly given as $V^\Gamma_{(\chi\omega\kappa LS)_{fi}} \equiv \langle(\chi\omega\kappa(LS)\Gamma M)_f|V|(\chi\omega\kappa(LS)\Gamma M)_i\rangle$, with $\chi \equiv \{\eta_r\eta_s\}$ and with symmetry properties $V^\Gamma_{(\chi\omega\kappa LS)_{if}} = V^\Gamma_{(\chi\omega\kappa LS)_{fi}}$. The initial and final values of $(\chi\omega\kappa LS)_{if}$ can be different, *i.e.*, the SU(3)$\times$SU(2)$_S$ rank of V is non-zero. In addition, since $J_0 = 0$, we have $L_0 = S_0$, thus the label L_0 will be henceforth omitted. Using that the interaction can be represented as a sum of SU(3)$\times$SU(2)$_S$ tensors, $V = \sum_{\rho_0\omega_0\kappa_0 S_0} V^{\rho_0\omega_0\kappa_0 S_0}$, the matrix elements can be further reduced with respect to SU(3) and the spin-isospin space (for $T_0 = 0$), $V^{\rho_0\omega_0\kappa_0 S_0}_{(\chi\omega S)_{if};T} \equiv \left\langle(\chi\omega S)_f;T||V^{\omega_0\kappa_0 S_0}||(\chi\omega S)_i;T\right\rangle_{\rho_0}$ (see Appendix A). Here, the superscripts show the rank of the SU(3)$\times$SU(2)$_S$ tensor, and ρ_0 is the multiplicity that distinguishes between multiple occurrences of ω_0 for the same ω_i and ω_f.

The following conjugation relations hold for the SU(3) $\times$ SU(2)$_S$ tensors,

$$\begin{aligned} V^{\rho_0\omega_0\kappa_0 S_0}_{(\chi\omega S)_{if};T} &= (-)^{S_i-S_f+S_0}(-)^{\omega_f-\omega_i}\sqrt{\frac{\dim\omega_f}{\dim\omega_i}}V^{\rho_0\tilde{\omega}_0\kappa_0 S_0}_{(\chi\omega S)_{fi};T} \\ V^{\rho_0\omega_0\kappa_0 S_0}_{(\chi\omega S)_{ii};T} &= (-)^{S_0}V^{\rho_0\tilde{\omega}_0\kappa_0 S_0}_{(\chi\omega S)_{ii};T}\,, \end{aligned} \tag{2.2}$$

where

$$\dim\omega = \frac{1}{2}(\lambda+1)(\mu+1)(\lambda+\mu+2). \tag{2.3}$$

To simplify further equations, we introduce a symmetrized tensor,

$$v^{\rho_0\omega_0\kappa_0 S_0}_{(\chi\omega S)_{if};T} = (-)^{\omega_i - S_i - T}\sqrt{\dim\omega_i}V^{\rho_0\omega_0\kappa_0 S_0}_{(\chi\omega S)_{if};T}, \tag{2.4}$$

with a conjugation relation,

$$v^{\rho_0\omega_0\kappa_0 S_0}_{(\chi\omega S)_{if};T} = (-)^{S_0}v^{\rho_0\tilde{\omega}_0\kappa_0 S_0}_{(\chi\omega S)_{fi};T}. \tag{2.5}$$

We note that, in the case when $\chi_i = \chi_f$, $\omega_i = \omega_f$, and $S_i = S_f$, we will use the notation $v^{\rho_0\omega_0\kappa_0 S_0}_{(\chi\omega S);T}$.

The significance of the various SU(3) tensors can be estimated by their Hilbert-Schmidt norm, which is analogous to the norm of a matrix A defined as $||A|| = \sqrt{\sum_{ij} A_{ij}A_{ji}}$. In particular, the strength of a Hamiltonian H can be estimated by the norm σ_H constructed as [44–49]

$$\sigma_H^2 = \left\langle (H - \langle H\rangle)^\dagger (H - \langle H\rangle)\right\rangle = \left\langle H^2\right\rangle - \langle H\rangle^2, \tag{2.6}$$

where $\langle\ldots\rangle \equiv \frac{1}{\mathcal{N}}\mathrm{Tr}(\ldots)$ specifies the trace of the Hamiltonian matrix divided by the $\mathcal{N}$ number of diagonal matrix elements. In the present study, H is a two-body Hamiltonian, and $\mathcal{N}$ enumerates all possible two-particle configurations.

For given $T_f = T_i = T$ and a $|\chi^*\omega\kappa(LS)\Gamma M_\Gamma\rangle$ basis with $\chi^* \equiv \{\eta_r\eta_s\}, \eta_r \le \eta_s$, the norm $\sigma_{\omega_0\kappa_0 S_0;T}$ of each SU(3)-symmetric tensor is determined using Eq. (2.6):

$$\begin{aligned}\sigma^2_{\omega_0\kappa_0 S_0;T} &= \frac{1}{\mathcal{N}}\sum_{(\chi^*\omega S)_{f,i}\rho_0}\frac{1}{\Pi^2_{TS_0}\dim\omega_0}|v^{\rho_0\omega_0\kappa_0 S_0}_{(\chi\omega S)_{if};T}|^2 \\ &\quad -(V_c^{\omega_0\kappa_0 S_0;T})^2,\end{aligned} \tag{2.7}$$

where the number of two-particle basis states $\mathcal{N}$ and the average monopole part $V_c^{\omega_0\kappa_0 S_0} =$

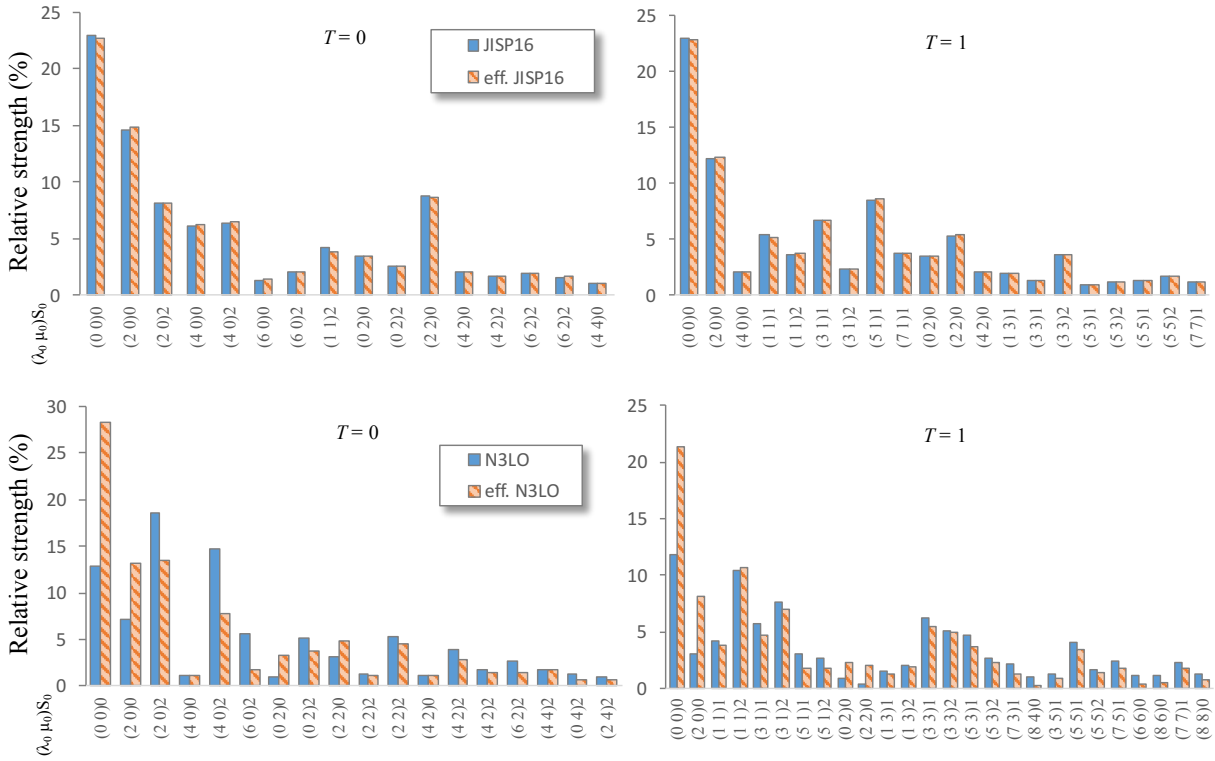

Figure 2.3. Relative strengths $\mathfrak{s}$ (in %) for the SU(3)-coupled JISP16 (top) and N3LO (bottom) NN interactions and their effective counterparts with $\hbar\Omega = 15$ MeV and 20 MeV, respectively, in the $N_{\max}$= 6 model space. The "eff. JISP16" is obtained by the OLS technique for A=12, while "eff. N3LO" is by SRG with $\lambda_{\rm SRG} = 2.0$ fm^{-1}. T is the isospin of the two nucleon system. A set of $(\lambda_0\mu_0)S_0$ quantum numbers and its conjugate correspond to each of the interaction terms. Only terms with >1% relative strength for each T are shown; there are more than 120 terms with less than 1% strength for this model space. Figure adapted from Sargsyan *et al.* [43].

$\left\langle V^{\omega_0\kappa_0(L_0=S_0S_0)\Gamma_0=0M_{\Gamma_0}=0}\right\rangle$ are given, respectively, as

$$\mathcal{N} = \sum_{\chi^*\omega\kappa LSJM_J} 1 = \sum_{\chi^*\omega S} \Pi_S^2 \dim\omega, \tag{2.8}$$

$$V_c^{\omega_0\kappa_0 S_0} = \frac{1}{\mathcal{N}} \sum_{\substack{\chi^*\omega\kappa \\ LSJ\rho_0}} \frac{\Pi_J^2\Pi_L}{\Pi_{S_0T}\sqrt{\dim\omega}}(-1)^{S_0+L+J-T-\omega} \times \begin{Bmatrix} L & S & J \\ S & L & S_0 \end{Bmatrix} \langle \omega\kappa L; \omega_0\kappa_0 L_0 \| \omega\kappa L\rangle_{\rho_0} v^{\rho_0\omega_0\kappa_0 S_0}_{(\chi\omega S);T}. \tag{2.9}$$

For a given isospin T, the strength of the entire Hamiltonian H_T is determined by the

strengths of its components, $\sigma^2_{H_T} = \sum_{\omega_0\kappa_0 S_0} \sigma^2_{\omega_0\kappa_0 S_0;T}$. We can then define a relative strength for each SU(3)-symmetric component $(\omega_0\kappa_0 S_0)$ as

$$\mathfrak{s}^2_{\omega_0\kappa_0 S_0;T} = \frac{\sigma^2_{\omega_0\kappa_0 S_0;T}}{\sigma^2_{H_T}} = \frac{\sigma^2_{\omega_0\kappa_0 S_0;T}}{\sum_{\omega_0\kappa_0 S_0} \sigma^2_{\omega_0\kappa_0 S_0;T}}. \tag{2.10}$$

Using Eq. (A.3), we can decompose any two-body interaction into SU(3)-symmetric components. The contribution of each of the components within the interaction is given by its relative strength (2.10) (see Fig. 2.3 for the realistic JISP16 and N3LO interactions). As can be seen from these results, only a small number of SU(3) tensors dominate the interaction, with the vast majority of the components having less than 1% of the total strength. The most dominant term, *i.e.*, $(\lambda_0\,\mu_0) = (0\,0)$ is the one that preserves the SU(3) symmetry, which therefore – already at the interaction level – signals the goodness of the Elliott model [37,38]. Similar behavior is observed for other interactions. It should be noted that in the JT-coupled basis, no such dominance at the interaction level is apparent. This exercise demonstrates a long-standing principle that holds across all of physics; namely, one should work within a framework that is as closely aligned with the dynamics as possible [50].

2.4 SU(3)-guided NN interaction application to ^{12}C and deuteron

The decomposition of the interaction in the SU(3) basis allows us to choose sets of major components to construct new selected interactions. These interactions can be used for calculations of various nuclear properties that can then be compared to the results from the initial interaction. In this way, we can examine how sensitive specific nuclear properties are to the interaction components.

Several selected interactions were constructed for this study. The selection is done by ordering the interaction tensors from the highest relative strength to the lowest and then including the largest ones to add up to 60 - 90% of the initial total strength. Depending on the $N_{\max}$ of the interaction the number of selected SU(3) tensors differs. For example, the JISP16 interaction in $N_{\max}$= 10, $\hbar\Omega$=15 MeV has overall 169 unique $(\lambda_0\mu_0)S_0$ tensors, out

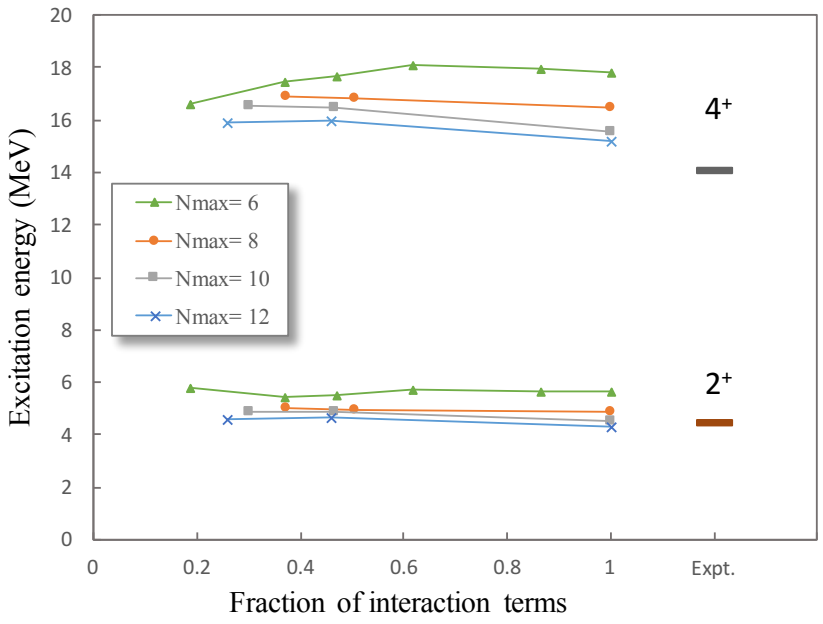

Figure 2.4. Excitation energy of the first 2^+ and 4^+ states in ^{12}C from SA-NCSM calculations (connected lines) as a function of the fraction of the terms kept in the interaction, and compared to experiment [51] (labeled as "Expt."). Results for $N_{\max}$= 6, 8, 10, and 12 are shown for various selections of the JISP16 interaction with $\hbar\Omega$ = 15 MeV. Specifically, the value 1 on the abscissa indicates the full interaction (100%) was used, while an abscissa value of 0.4 implies that only the most significant 40% of the tensors were retained, etc. Figure adapted from Sargsyan *et al.* [43]

of which the 51 largest ones account for about 80% of the total strength. After selection the total strengths are not rescaled to the initial interaction. Throughout this work we will refer to selected interactions in terms of the fraction of interaction tensors kept, that is the number of SU(3)-symmetric components in the selected interaction relative to the number of all such components in the initial interaction for a given $N_{\max}$ and $\hbar\Omega$.

Analysis of the results shows that low-lying excitation energies of ^{12}C are not sensitive to the number of selected SU(3) tensors, given that the most dominant ones are included in the interaction (Fig. 2.4). With only half of the interaction tensors the excitation energies essentially do not differ from the corresponding results that use the full interaction, and even with less than 30% of the interaction components the deviation for most of the values is insignificant. The comparatively large deviation in 4^+ energy for $N_{\max}$= 6 that happens

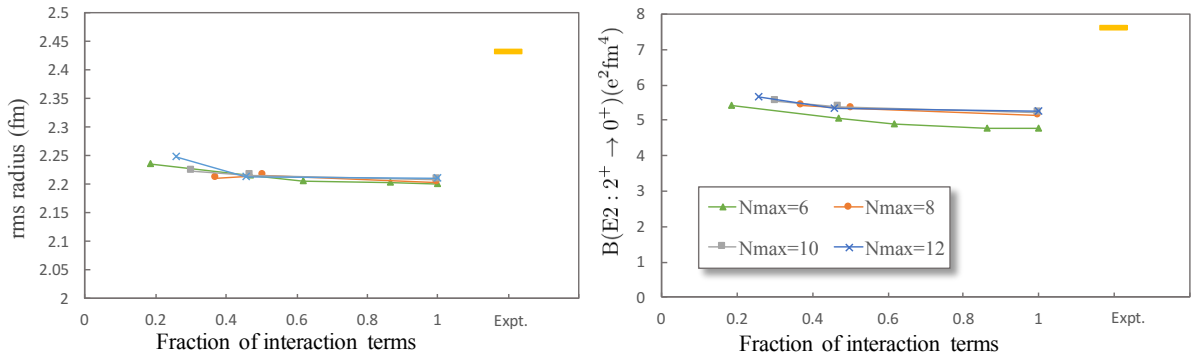

Figure 2.5. Same as Fig. 2.4, but for the rms radius (in fm) of the ^{12}C ground state (experimental value from Ref. [52]) and the B(E2: $2_1^+ \rightarrow 0_1^+$) strengths (in e^{2}fm^4) (experimental value from [51]) as a function of the fraction of the terms kept in the interaction. SA-NCSM calculations use various selections for the JISP16 interaction for $\hbar\Omega = 15$ MeV and different $N_{\max}$ model spaces. Figure adapted from Sargsyan *et al.* [43]

when about 20% of the SU(3) components are used is likely due to the small model space. This issue disappears in higher $N_{\max}$ values, and even $N_{\max}$= 6 results for the 2^+ state compare remarkably well to the initial interaction for all selections.

The selected interactions yield very close results to the initial one for other observables as well. For example, the ^{12}C rms radius of the ground state and the B(E2: $2^+ \rightarrow 0^+$) have very low dependence on the selection (Fig. 2.5), with variations nearly inconsequential compared to the deviations from the experiment (the underprediction of these observables for the JISP16 interaction has been addressed, e.g., in Ref. [53]). Specifically, the values are essentially the same when half of the interaction components are used. With less than 30% of interaction components, the difference from the initial interaction results is less than 2% for rms radius and less than 7% for B(E2). Thus, small deviations start to appear only at significantly trimmed interactions, indicating that the long-range physics is mostly preserved when only the dominant interaction terms are used.

In addition, vital information about the nuclear structure can be found through analysis of the $(\lambda\mu)S$ configurations that comprise the SA-NCSM wavefunction. This uncovers the physically relevant features that arise from the complex nuclear dynamics as shown in Ref. [1].

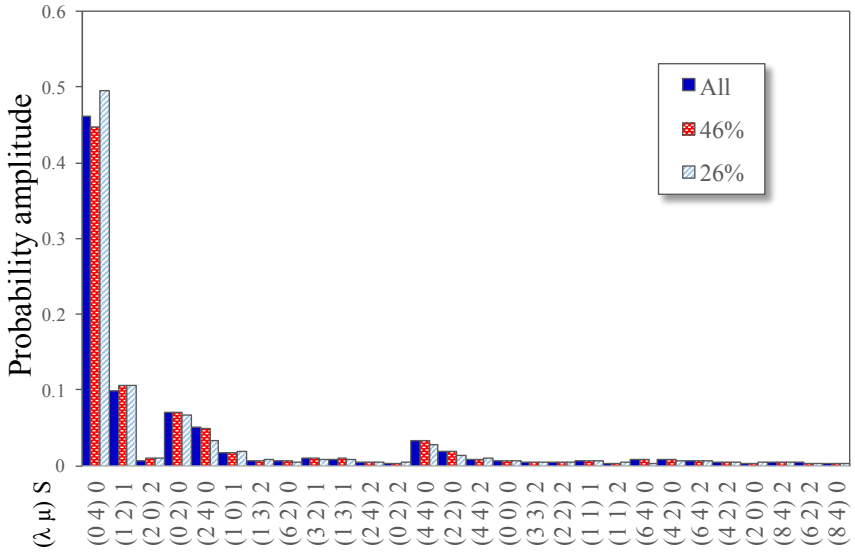

Figure 2.6. Probability amplitudes for the $(\lambda\,\mu)S$ configurations that make up the ^{12}C ground state (0^+_1), calculated in $N_{\max}$= 12 model space using JISP16 interaction for $\hbar\Omega$ = 15 MeV (labeled by "All") and two selected interactions (labeled by the fraction of the interaction components kept, 46% and 26%). Only states with probability amplitudes > 0.003 are shown. Figure adapted from Sargsyan *et al.* [43]

In other words, the wavefunctions contain a manageable number of major SU(3) components that account for most of the underlying physics. Indeed, we find that calculations with various selected interactions largely preserve the major components of the wavefunction (Fig. 2.6). For the ground state of ^{12}C calculated in the $N_{\max}$= 12 model space the probability amplitude for each set of the quantum numbers $(\lambda\mu)S$ almost does not change when a little less then half (46%) of the JISP16 interaction tensors are used for the calculations. Even with about quarter (26%) of the tensors, the SU(3) structure remains the same with only a slight difference in the amplitudes. It should be noted that, the $(\lambda\mu)S$ here are not to be confused with the ones in Fig. 2.3, as they correspond to the many-body states of ^{12}C. In particular, $(0\,4)0$ is the lowest particle configuration in the HO basis, that is, 4 particles in $(\eta_z, \eta_x, \eta_y) = (1, 0, 0)$ and 4 particles in $(0, 1, 0)$. As shown in Fig. 2.6, this accounts for almost half of the probability amplitude of the ground state wavefunction. The first three $(\lambda\mu)S$ in the figure correspond to the 0p-0h configurations, among which the $(0\,4)0$ is

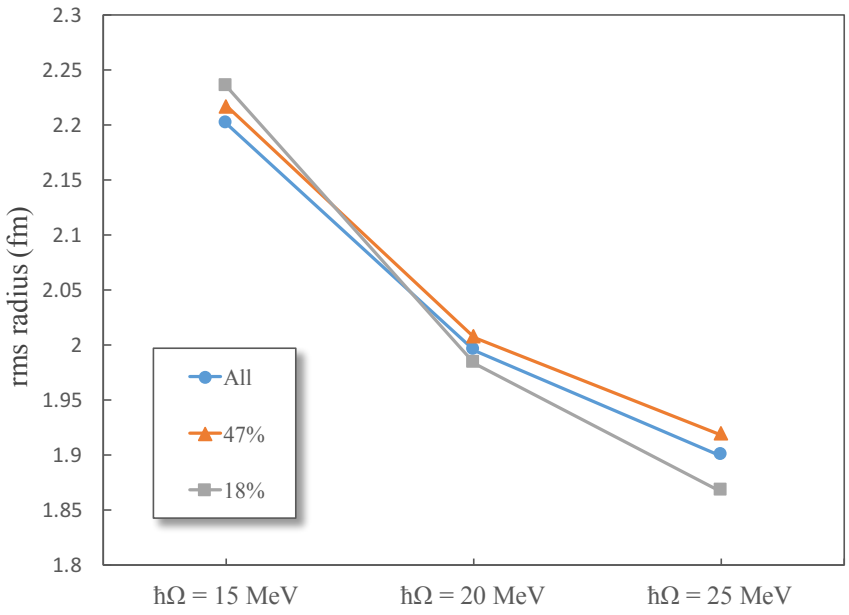

Figure 2.7. ^{12}C ground state rms radius from SA-NCSM calculations with $N_{\max}$= 6 model space vs. $\hbar\Omega$, using the full ("All") and selected (labeled by the percentage of the tensors kept) JISP16 interaction. Figure adapted from Sargsyan *et al.* [43].

the most deformed and has the lowest spin. The dominance of configurations with largest deformation and lowest spin has been shown in Ref. [1].

As mentioned above, the dependence on the HO parameter $\hbar\Omega$ disappears at the $N_{\max}\to\infty$ limit, however, even for comparatively small $N_{\max}$ model spaces, there is often a range of $\hbar\Omega$ values, which achieves convergence for selected observables, while typically larger $N_{\max}$ model spaces are required outside this range. For long-range observables, such a range often falls closely to an empirical estimate given by $\hbar\Omega = 41/A^{1/3}$ [54], which is 18 MeV for ^{12}C. We investigate the dependence of the ground state rms radius of ^{12}C on $\hbar\Omega$ using different selections (Fig. 2.7). We examine small model spaces, where the $\hbar\Omega$ dependence is large and its effect on the interaction selections is expected to be enhanced; yet, we ensure that these model spaces provide results close to the $N_{\max}$=12 outcomes (see $N_{\max}$=6 and 8 results in Figs. 2.4 and 2.5). Comparing to the full interaction, the results indicate that, indeed, small deviations are observed for values around $\hbar\Omega$ = 18 MeV, and the deviations

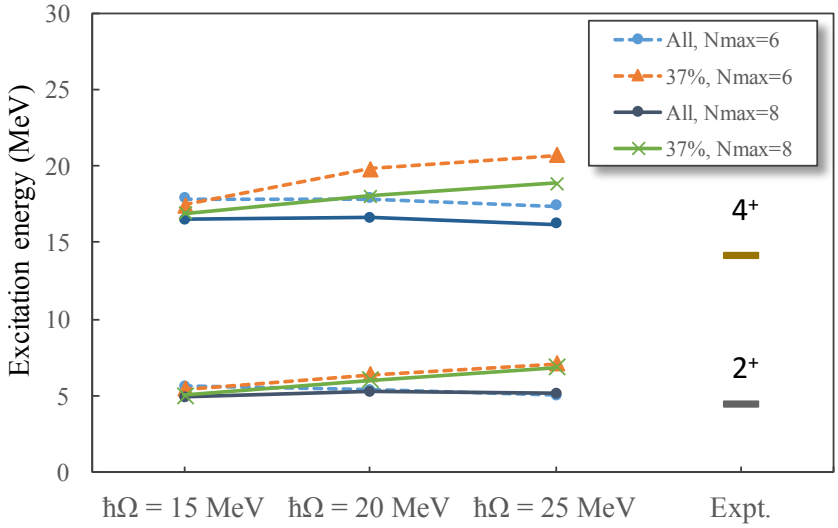

Figure 2.8. Excitation energies of the first 2^+ and 4^+ states for ^{12}C from SA-NCSM calculations with $N_{\max}$= 6 and $N_{\max}$= 8 model spaces using full JISP16 interaction ("All") and its selected counterpart (with 37% of the tensors kept), with $\hbar\Omega = 15, 20$ and 25 MeV, and compared to experiment. Figure adapted from Sargsyan *et al.* [43].

become larger at higher (less optimal) $\hbar\Omega$ values (Fig. 2.7). Similarly, the excitation energies for $\hbar\Omega = 15$ MeV calculations are much less sensitive to the interaction selection (Fig. 2.8), whereas the deviation in the results between the initial and selected interactions increases for higher $\hbar\Omega$. However, this difference gets smaller with increasing model space. To summarize, the selection of the interactions affects the calculations with optimal $\hbar\Omega$ values the least.

It is interesting to examine how the selection of NN interactions affects the nucleon-nucleon physics. As a simple illustration, we study the Hamiltonian for the proton-neutron system and its corresponding eigenvalues. (We note that states beyond the lowest 1^+ state are scattering states, but they appear in a shell model energy spectra as distinct states; however, the idea here is to examine if there is any loss of information in the selected NN interaction, which in turn guides *ab initio* calculations.) In addition to $T = 0$ states, we consider $T = 1$ states, which can also inform the proton-proton and neutron-neutron systems. To do this, we look for deviations in the corresponding eigenvalues as compared to those computed with the full interaction.

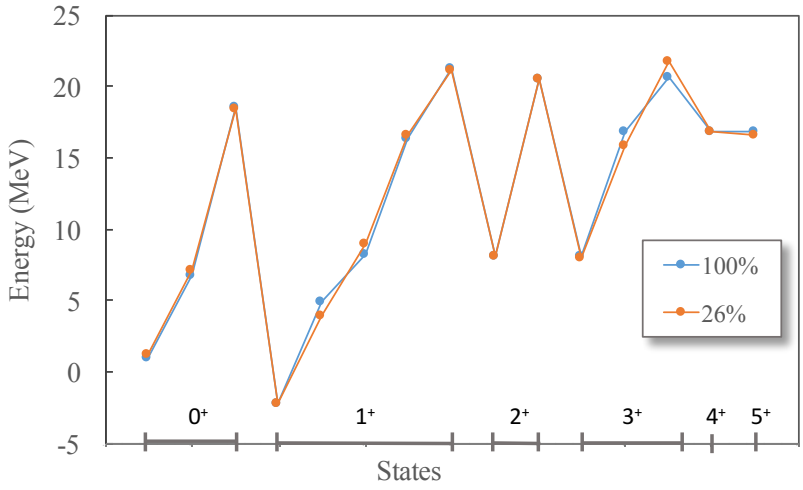

Figure 2.9. Energies of the proton-neutron system for the positive-parity lowest-lying states (< 30 MeV), calculated in the SA-NCSM in $N_{\max}$=12 model space using the JISP16 interaction, with all terms kept (100%) as compared to a selection that keeps only 26% of the terms, for $\hbar\Omega$=15 MeV. Figure adapted from Sargsyan *et al.* [43].

In particular, we observe that only about quarter of the SU(3)-symmetric interaction components (the most dominant ones) can reproduce, with high accuracy, the $N_{\max}$=12 calculated energies that use the full interaction for most of the low-lying states of the proton-neutron system (Fig. 2.9). To estimate the difference in energies, we calculate the root mean square error (RMSE), RMSE $= \sqrt{\frac{1}{N_d}\sum_i^{N_d}\left(E^i_{\rm all} - E^i_{\rm sel}\right)^2}$ where $E_{\rm all}$ and $E_{\rm sel}$ are the eigenenergies calculated with the initial and selected interactions, respectively, the summation is over all positive- or negative-parity states and N_d is the total number of states. For negative-parity $0 \leq J \leq 5$ states up through energy with 30 MeV, we find RMSE to be about 0.9 - 1.2 MeV depending on $\hbar\Omega$, whereas for positive-parity states, it is between 0.5 and 0.9 MeV. Similar RMSE values are seen even for the higher lying spectrum up to 50 MeV. As it can be seen from Fig. 2.9, the main deviations come from the second and third 1^+ and 3^+ states indicating that certain states are more sensitive to the selection than others.

Comparing the SU(3) decompositions of initial interactions to their renormalized (effective) counterparts shows that the same major SU(3) tensors remain dominant after renormalization (Fig. 2.3). In the case of JISP16 the tensors with the largest relative strengths

practically do not change. The renormalization has a larger impact on the N3LO interaction where the spread over various tensors is larger. Here, only a few SU(3)-symmetric components change significantly while the others change slightly. It should be noted that the two effective counterparts of the interactions resemble each other (Fig. 2.3). A similar behavior is observed for, e.g., the AV18 [55] and CD-Bonn interactions [1].

Examining the largest contributing tensors of realistic interactions we can link them to the monopole operator (the HO potential), $Q \cdot Q$, spin-orbit, pairing and tensor forces. The key idea is that the position and momentum operators, $\vec{r}$ and $\vec{p}$ respectively, have an SU(3) rank $(1\,0)$, and conjugate $(0\,1)$ (to preserve hermiticity), with $\mathrm{SU}(2)_S$ rank zero ($S_0 = 0$, that is, the operator does not change spin). The HO potential operator ($\sim r^2 = \vec{r} \cdot \vec{r}$) has orbital momentum $L_0 = 0$ and spin $S_0 = 0$, and its SU(3) rank is obtained by coupling $(1\,0) \times (1\,0)$, $(1\,0) \times (0\,1)$ and conjugates. For $L_0 = 0$, the SU(3) Clebsch-Gordan coefficients for these couplings are non-zero only for total $(\lambda_0\,\mu_0) = (0\,0)$, $(2\,0)$ and $(0\,2)$ that, in turn, define the SU(3) ranks of the HO potential.

The quadrupole operator Q, given by the tensor product of $\vec{r}$, has $L_0 = 2$ and $S_0 = 0$. Here, the SU(3) Clebsch-Gordan coefficients restrict the total $(\lambda_0\,\mu_0)$ to $(2\,0)$ and $(1\,1)$ (and conjugates), which define the SU(3) rank of Q [56]. Consequently, the $Q \cdot Q$ operator, which describes the interaction of each nucleon with the quadrupole moment of the nucleus, will have $L_0 = 0$ and spin $S_0 = 0$, along with SU(3) rank of $(4\,0)$, $(2\,0)$, $(2\,2)$ and $(0\,0)$ (and conjugates). Similarly, the spin-orbit operator has $(\lambda_0\,\mu_0) = (1\,1)$, $L_0 = 1$ from the orbital momentum operator and $S_0 = 1$ from the spin operator.

The idea of the pairing interaction in nuclei is that the configurations with paired nucleons are energetically favored. The SU(3) ranks of the pairing interaction are derived in Ref. [57], which shows that a large number of pairing interaction tensors have $\lambda_0 = \mu_0$ SU(3) rank. Lastly, the nuclear tensor force originates mainly from the one-pion exchange and it depends on the orientation of the spins with regard to the relative coordinate vector joining the two nucleons (see, *e.g.*, Ref. [58]). Similarly to the quadrupole operator, the tensor force has

$L_0 = 2$ and SU(3) rank of $(2\,0)$ and $(1\,1)$ (and conjugates), but with $S_0 = 2$, coming from the tensor coupling of the spin operators.

Indeed, the scalar $(0\ 0)$ S_0=0 dominates for a variety of realistic interactions, and especially in their effective counterparts (see Fig. 2.3). As mentioned above, this suggests a dominant Elliott SU(3) symmetry. This may have important implications for various models that employ the SU(3) symmetry, such as the ones in Refs. [59–65]. The next important components are typically $(2\,0)$, $(4\,0)$ and $(2\,2)S_0$=0 and their conjugates. These SU(3) modes are the ones that appear in the $Q \cdot Q$ interaction, while $(\lambda_0\,\lambda_0)$ configurations dominate the pairing interactions within a shell [57]. The dominant $(2\,0)$ and $(1\,1)S_0 = 2$ modes, and conjugates, can be linked to the tensor force. Finally, the $(1\,1)S_0$=1 can be linked to the spin-orbit force. These features, we find, repeat for various realistic interactions and, more notably, the similarity is found to be further enhanced for their renormalized counterparts. Given the link between the phenomenon-tailored interactions and major terms in realistic interactions, it is then not surprising that both *ab initio* approaches and earlier schematic models can successfully describe dominant features in nuclei.

3 Collectivity and Spin Structure: Intermediate-mass Nuclei with the SA-NCSM

Electromagnetic transitions in nuclei are treated as interactions of the nucleus with an external electromagnetic field. They are often used to probe the collectivity and spin structure in nuclei. In this chapter we discuss the calculations of electromagnetic transitions in the HO basis and present applications to various intermediate mass nuclei.

3.1 Electromagnetic transitions, multipole moments, and selection rules

Electromagnetic processes in atomic nuclei are considered as perturbations that change the state of the nucleus. The transition probability per unit time or *transition rate* W_{fi} of a gamma decay from an initial state i to a final state f is inversely proportional to the half life of the decay

$$t_{1/2} = \frac{\ln 2}{W_{fi}}. \tag{3.1}$$

Electromagnetic transitions occur by multipole components L_0 and M_0 of the radiation field. The transition rate for given L_0M_0 is calculated by the Fermi golden rule of time-dependent perturbation theory [66, 67]. It has the following form in CGS units:

$$W_{fi}^{L_0M_0} = \frac{8\pi(L_0+1)}{\hbar L_0[(2L_0+1)!!]^2}\left(\frac{E_\gamma}{\hbar c}\right)^{2L_0+1} |\langle \xi_f J_f m_f | O_{L_0M_0} | \xi_i J_i m_i \rangle|^2, \tag{3.2}$$

where E_γ is the γ-ray energy from the decay, $O_{L_0M_0}$ is the transition operator, J_i (J_f) is the total angular momentum of the initial (final) state, m_i (m_f) is the projection of J_i (J_f) on the quantization axis, and ξ_i (ξ_f) accounts for additional quantum numbers.

Since the substates m_i and m_f are usually not detected separately, the transition rates are summed over the final substates and averaged over the initial substates

$$W_{fi}^{L_0} = \frac{1}{2J_i+1}\sum_{m_i,m_f,M_0} W_{fi}^{L_0M_0} = \frac{8\pi(L_0+1)}{\hbar L_0[(2L_0+1)!!]^2}\left(\frac{E_\gamma}{\hbar c}\right)^{2L_0+1} \frac{|\langle \xi_f J_f \| O_{L_0} \| \xi_i J_i \rangle|^2}{2J_i+1}, \tag{3.3}$$

where $(2J_i+1)$ is the number or initial substates and we used Wigner-Eckart theorem and

orthonormality of Clebsch-Gordan coefficients to obtain the reduced form of the matrix elelment in Eq. 3.3:

$$\begin{aligned}\sum_{m_i,m_f,M_0} |\langle \xi_f J_f m_f | O_{L_0 M_0} | \xi_i J_i m_i \rangle|^2 &= \frac{1}{2J_f+1} \sum_{m_i,m_f,M_0} |C^{J_f m_f}_{J_i m_i L_0 M_0} \langle \xi_f J_f \| O_{L_0} \| \xi_i J_i \rangle|^2 \\ &= |\langle \xi_f J_f \| O_{L_0} \| \xi_i J_i \rangle|^2. \end{aligned} \tag{3.4}$$

In Eq. 3.3 the quantity

$$B(L_0, \xi_i J_i \to \xi_f J_f) \equiv \frac{|\langle \xi_f J_f \| O_{L_0} \| \xi_i J_i \rangle|^2}{2J_i+1} \tag{3.5}$$

is called reduced transition probability or *transition strength*. The operator $O_{L_0 M_0}$ can represent either electric or magnetic transitions, which are given as

$$Q_{L_0 M_0} = \sum_{j=1}^{A} e_j r_j^{L_0} Y_{L_0 M_0}(\theta_j, \phi_j), \tag{3.6}$$

$$M_{L_0 M_0} = \sum_{j=1}^{A} \Big[\frac{2}{L_0+1} g_j^l \vec{l_j} + g_j^s \vec{s_j} \Big] \cdot \vec{\nabla}_j [r_j^{L_0} Y_{L_0 M_0}(\theta_j, \phi_j)], \tag{3.7}$$

where e_j is the electric charge, and l_j and s_j are the angular momentum and spin of the nucleon j. The g^l and g^s are gyromagnetic ratios which for protons have the values $g^s_\pi = 5.586\mu_N$ and $g^l_\pi = 1\mu_N$, and for neutrons $g^s_\nu = -3.826\mu_N$ and g^l_ν=0, with μ_N being the nuclear magneton. From Eqs. (3.6) and (3.7) we can see that the units of the electric moments are in $[e\,\mathrm{fm}^{L_0}]$ and for magnetic moments $[\mu_N\,\mathrm{fm}^{L_0-1}]$. For transition strengths these units are squared. Often the experimental values of the transition strengths are given in Weisskopf units [W.u.], which show roughly how many nucleons contribute to the radiation. The conversion between the units for electric and magnetic transition strengths are as follows:

$$B(EL_0)[\text{W.u.}] = \frac{(1.2)^{2L_0}}{4\pi} \Big(\frac{3}{L_0+3} \Big)^2 A^{2L_0/3} B(EL_0)[e^2\,\mathrm{fm}^{2L_0}] \tag{3.8}$$

$$B(ML_0)[\text{W.u.}] = \frac{10}{\pi} (1.2)^{2L_0-2} \Big(\frac{3}{L_0+3} \Big)^2 A^{(2L_0-2)/3} B(ML_0)[\mu_N^2 \mathrm{fm}^{2L_0-2}] \tag{3.9}$$

For the low-lying states in nuclei the energy of the gamma transition is of order of 10^0 to 10^1 MeV, so the ratio $E_\gamma/(\hbar c)$ is around 10^{-2} to 10^{-1}. Due to the exponential decrease of the transition rate with the increase of the multipolarity order L_0 in Eq. (3.3), the transition between initial $J_i^{\pi_i}$ and final $J_f^{\pi_f}$ states is mainly dominated by the small values of L_0. Here π is the parity of the state. Thus, we will be interested in electric dipole ($E1$) and quadrupole ($E2$) as well as magnetic dipole ($M1$) transitions. The operator forms for these transitions are

$$Q_{1M_0} = \sum_{j=1}^{A} e_j r_j Y_{1M_0}(\theta_j, \phi_j) = \sqrt{\frac{3}{4\pi}} \sum_{j=1}^{A} e_j r_{1M_0}^{(j)}, \tag{3.10}$$

$$Q_{2M_0} = \sum_{j=1}^{A} e_j r_j^2 Y_{2M_0}(\theta_j, \phi_j) = \sqrt{\frac{15}{8\pi}} \sum_{j=1}^{A} e_j [r_1^{(j)} \times r_1^{(j)}]_{2M_0}, \tag{3.11}$$

$$M_{1M_0} = \sqrt{\frac{3}{4\pi}} \sum_{j=1}^{A} (g_j^s s_{1M_0}^{(j)} + g_j^l l_{1M_0}^{(j)}), \tag{3.12}$$

where $\vec{r}$ is expressed as a spherical tensor and for the magnetic dipole operator we use the fact that $\vec{\nabla}_j [r_j Y_{1M_0}(\theta_j, \phi_j)] \sim \hat{e}_{M_0}$, with $\hat{e}_{M_0}$ being a unit spherical tensor of rank 1. We note that there are no $E0$ gamma transitions since a γ-ray cannot carry spin 0. Such monopole transitions are possible through internal electron conversion and are described by the r^2 operator. The absence of $M0$ transitions comes from the fact that there are no magnetic charges in nature.

The selection rule for a multipole transition with L_0 connecting an initial state with total angular momentum J_i to a final state J_f is given by

$$|J_f - J_i| \leq L_0 \leq J_f + J_i. \tag{3.13}$$

To obtain a selection rule for the parities we examine the expressions in Eqs. (3.6) and (3.7). The spherical harmonics $Y_{L_0 M_0}$ has parity of $(-1)^{L_0}$, while the scalar r^{L_0} is $+1$. Therefore, for electric transitions with odd L_0, such as $E1$, the parity flips while for even L_0 transitions,

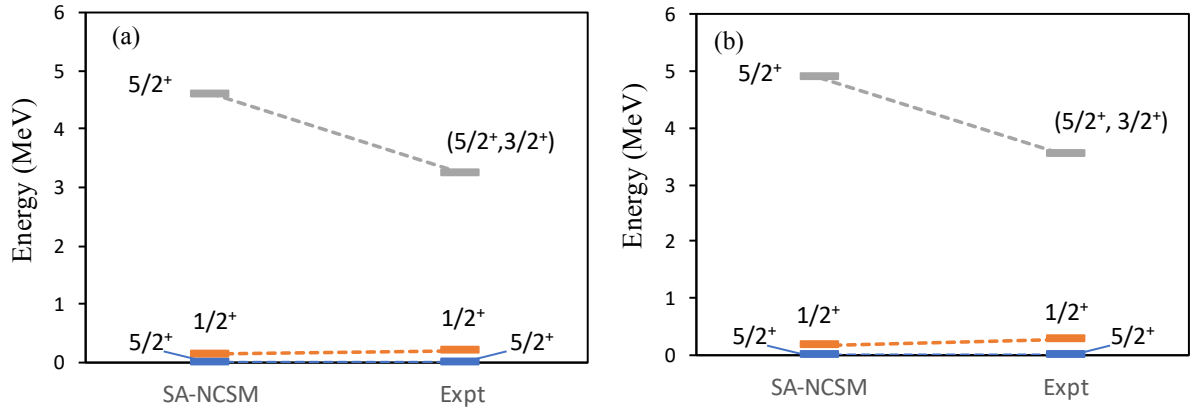

Figure 3.1. SA-NCSM calculations for (a) ^{21}Mg and (b) ^{21}F excitation energies using NNLO$_{\rm opt}$ interaction in $N_{\rm max}$=8 with HO parameter $\hbar\Omega$=15 MeV and compared to experiment (Expt). Experimental results are from Ref. [68].

such as $E2$, the parity is preserved. In the operator of magnetic transitions the $\vec{l}$ and $\vec{s}$ are axial vectors with parity $+1$. The vector operator $\vec{\nabla}$ has parity of -1, so there is one more -1 compared to the electric transitions. Hence, for magnetic transitions with odd L_0, such as $M1$, the parity of the initial state does not change, while it changes for even L_0.

Another electromagnetic observable that is measured in experiments is the charge quadrupole moment. The expression for this quantity is given by the electric quadrupole operator sandwiched between the same initial and final states with $M = J$.

$$Q(J) = \sqrt{\frac{16\pi}{5}} C^{JJ}_{JJ20} \frac{\langle \xi J \| Q_2 \| \xi J \rangle}{\sqrt{2J+1}}. \tag{3.14}$$

The charge quadrupole moment describes the effective shape of the nuclear charge distribution. The value of Q is negative if the shape is prolate and positive if it is oblate. The necessary angular momentum condition for a non-vanishing quadrupole moment is $J \geq 1$. This condition can be seen from the Clebsh-Gordan coefficient in Eq. (3.14).

3.2 SA-NCSM results for B(E2) strengths, quadrupole moments, and energy spectra

The electric and magnetic transitions along with multipole moments are essential observables in the study of nuclear structure. In theoretical calculations they are sensitive to

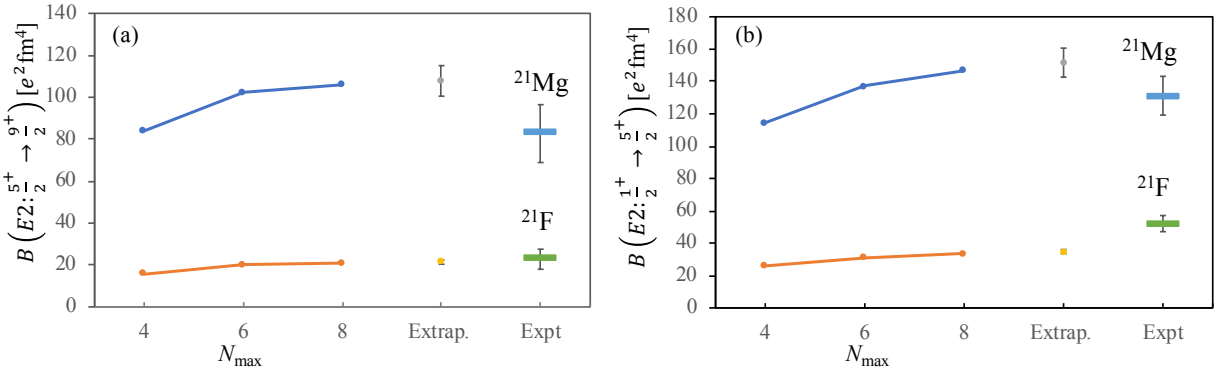

Figure 3.2. SA-NCSM calculations for (a) $B(E2{:}5/2^+ \rightarrow 9/2^+)$ and (b) $B(E2{:}1/2^+ \rightarrow 5/2^+)$ strengths for ^{21}Mg and ^{21}F using NNLO$_{\mathrm{opt}}$ interactions in $N_{\max}$=4 to 8 and $\hbar\Omega$=15 MeV alongside with extrapolated values ("Extrap."), and compared to experiment ("Expt"). Experimental results are from Ref. [68]. Extrapolations are performed using Shanks transformation [69], with uncertainties from $\hbar\Omega$ variance by 1 MeV.

details of the wavefunctions, hence providing a good test of a nuclear model. In addition, as mentioned above, the electric quadrupole moment provides an important information about the effective shape of the nuclear charge distribution. Thus, the electric quadrupole moments and transitions [$B(E2)$ strengths] provide an invaluable tool for studying collective features of nuclei.

In a recent experimental study in Ref. [68], $B(E2)$ strengths have been measured to investigate the isospin symmetry in odd-A ^{21}Mg and ^{21}F mirror nuclei. This work provided the first electric quadrupole transition measurements for the neutron deficient ^{21}Mg nucleus. We contributed to this study by calculating the $B(E2)$ strengths using the SA-NCSM, and without knowing the experimental results beforehand. In addition, the total angular momentum and parity assignment of the energy levels in ^{21}Mg and ^{21}F experimental spectra is challenging and only a few states with certain J and π are currently available in these nuclei. The calculated energies from SA-NCSM in $N_{\max}$=8 with NNLO$_{\mathrm{opt}}$ interaction compare well to the low-lying states from the experiment (Fig. 3.1). In particular, the calculations indicate a ground state of $J^\pi = 5/2^+$, and a first excited state of $J^\pi = 1/2^+$ slightly above the ground state similar to the experiment.

The $B(E2)$ calculations have been performed using NNLO$_{\mathrm{opt}}$ chiral interaction without

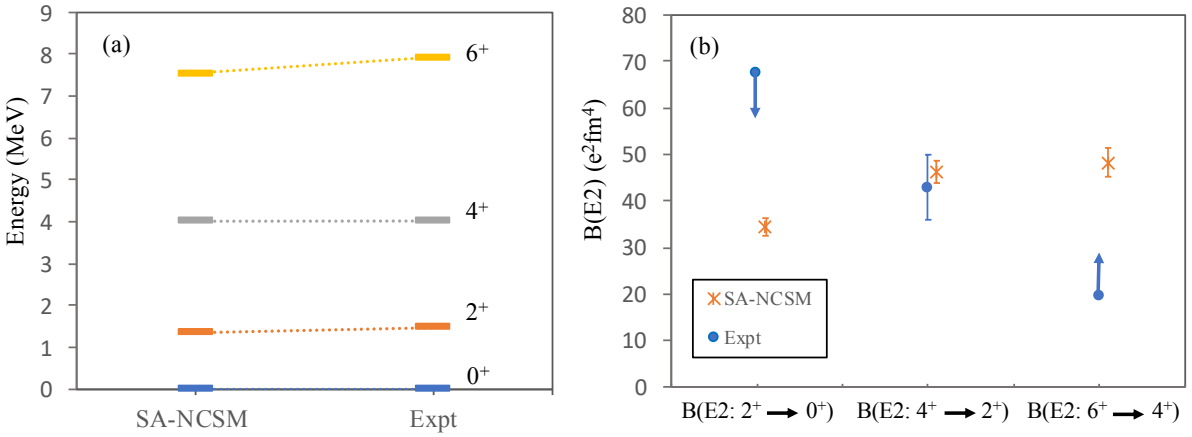

Figure 3.3. SA-NCSM calculations with NNLO_{opt} interaction for ^{28}Mg (a) excitation energies in $N_{\max}$=6 with HO parameter $\hbar\Omega$=15MeV and (b) B(E2) transition strengths between states of the lowest rotational band compared to the experiment (Expt). The up and down arrows on experimental values indicate that only upper or lower limit have been measured. Experimental results are from Ref. [70].

J^π	(6 6) S=0	(8 2) S=0	(7 4) S=1
0_1^+	40%	24%	15%
2_1^+	40%	23%	16%
4_1^+	42%	21%	18%
6_1^+	42%	19%	21%

Table 3.1. Contributions of dominant deformations for the ^{28}Mg yrast states from calculations in $N_{\max}$=6 with NNLO_{opt} interactions and HO parameter $\hbar\Omega$=15 MeV.

employing effective charges. To ensure convergence of results, the calculations have been carried out in several large model spaces, and extrapolated values obtained (Fig. 3.2). The uncertainties on extrapolations come from variation of $B(E2)$ with increasing $N_{\max}$ and the HO parameter $\hbar\Omega$. Given the uncertainties, the calculations are in a good agreement with the values measured in Ref. [68]. For ^{21}Mg, the SA-NCSM calculation yields larger collectivity than observed in the experiment, which practically arises from a slightly enhanced charge deformation.

In another recent study, the electric quadrupole transitions have been measured between the ^{28}Mg low-lying states [70]. One of the focuses of this study have been to investigate the neutron number $N = 20$ island of inversion, which is one of many regions of neutron shell breaking. We provided SA-NCSM calculations results for the energy spectrum and $B(E2)$

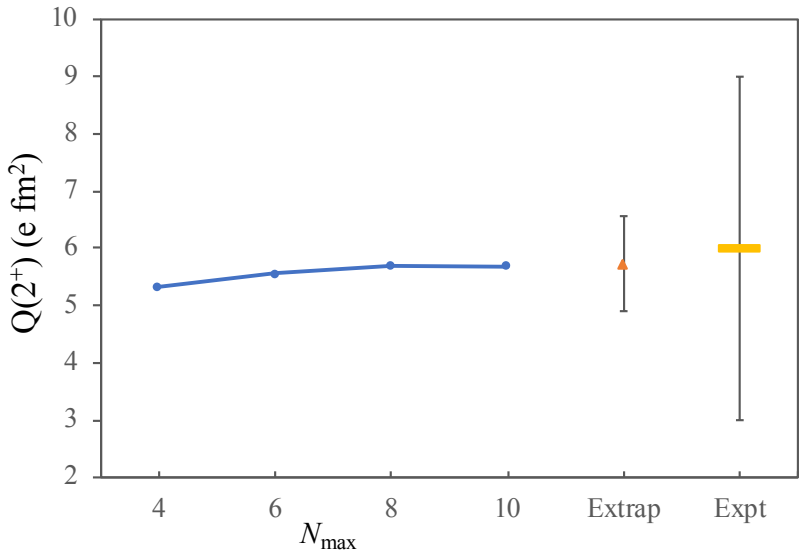

Figure 3.4. SA-NCSM calculations for the ^{12}C quadrupole moment for the lowest 2^+ state $[Q(2^+)]$ using NNLO$_{\rm opt}$ interaction with HO parameter $\hbar\Omega$=15 MeV. The uncertainty on the extrapolated value ("Extrap") is from $\hbar\Omega$ variance by 5 MeV. The experimental value ("Expt") is from Ref. [71].

strengths using NNLO$_{\rm opt}$ interaction up to $N_{\rm max}$=6 (*i.e.* 9 HO major shells) model space (Fig. 3.3).

The energy spectrum of the yrast band up to $J^\pi = 6^+$ is well reproduced by the SA-NCSM (Fig. 3.3a). Moreover, the calculations are consistent with the newly measured $B(E2{:}4_1^+ \rightarrow 2_1^+)$ of 42(7) e^2fm^4 (Fig. 3.3b), which indicates reduced collectivity in the yrast band at high intrinsic spin. The calculated wavefunctions demonstrate a shape coexistance of triaxial $(6\,6)S = 0$, and prolate $(8\,2)S = 0$ and $(7\,4)S = 1$ configurations (Table 3.1). The increased mixing between two major prolate configurations with intrinsic spin $S = 0$ and $S = 1$ for the 4_1^+ and 6_1^+ states compared to the 0_1^+ and 2_1^+ states may be responsible for the lowered transition strengths from the higher lying levels. The contribution of the $(7\,4)S = 1$ prolate shape might be slightly enhanced by the specific interaction used in the calculations, which can explain the low $B(E2 : 2^+ \rightarrow 0^+)$ transition strength.

Studying the deformation of the ^{12}C nucleus can provide insight into the structure of light nuclei. As mentioned in the previous chapter, the ground state of the ^{12}C in SA-NCSM is dominated by the oblate $(\lambda\,\mu) = (0\,4)$ configuration, consistent with the predictions from

earlier mean field models [72]. The corresponding 2^+ state of the yrast band has the same dominant deformation. The SA-NCSM calculations of the $Q(2^+)$ are in an good agreement with the experimental value (Fig. 3.4), which also indicates an oblate deformation for the lowest 2^+ [71]. With the increasing model space the fastest convergence is achieved for $\hbar\Omega$=15 MeV. The extrapolated results are obtained through fitting to a three parameter exponential function from Ref. [73] described in Chapter 6 [Eq. (6.11)], with the quoted uncertainties arising from $\hbar\Omega$ variance by 5 MeV.

The SA-NCSM calculations for a deformed ^{22}Ne nucleus are able to successfully capture collective features. Cluster structures (such as α+^{16}O+2n) in this kind of systems are of great interest to nuclear astrophysics. Again, to study the shape of the lowest lying states, we examine the 2^+ state in the yrast band (Fig. 3.5). The calculated excitation energy for this state practically does not differ from the experimental value (Fig. 3.5a). Contrary to the ^{12}C, the quadrupole moment of ^{22}Ne 2^+ is negative and calculations suggest a highly deformed prolate shape in agreement with the experimental observations [74]. The extrapolations are done using the three parameter exponential formula for $\hbar\Omega$=15 MeV calculations only [Eq. (6.11)]. Uncertainties due to $\hbar\Omega$ varience are not included. The extrapolated value agrees with the experimental one given the uncertainties (Fig. 3.5b).

3.3 SA-NCSM results for electromagnetic dipole transitions for ^{12}C and ^{20}Ne

Magnetic dipole transitions of ^{12}C and ^{20}Ne are of interest to neutrino physics since these nuclei are used in some of the detectors of accelerator-based neutrino experiments. Their excitation via $M1$ transitions has a close relation to the inelastic neutral-current neutrino-nucleus scattering. This scattering process is employed for the detection of supernova neutrinos and presents a significant source of background in modern high-energy neutrino detection experiments [75]. The energy spectrum of the supernova neutrinos is centered at approximately 10 MeV [76] resulting in excitation of target nuclei up to energies in this region. Thus, we will be interested in dipole transitions connecting the ground state to a few of the lowest excited states allowed by the selection rules.

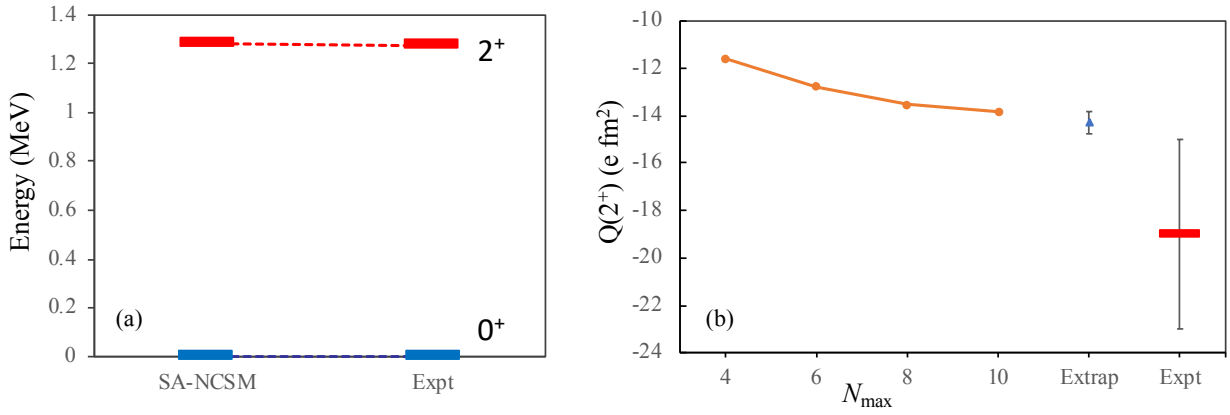

Figure 3.5. SA-NCSM calculations for ^{22}Ne (a) lowest 2^+ excitation energy in $N_{\max}$=10 and (b) quadrupole moment calculations up to $N_{\max}$=10, and compared to the experiment (Expt). All calculations are with HO parameter $\hbar\Omega$=15 MeV and NNLO$_{\rm opt}$ interaction. The uncertainty on the extrapolated value (Extrap) arises from the least squares fitting to the Eq. (6.11). Experimental results are from Ref. [74].

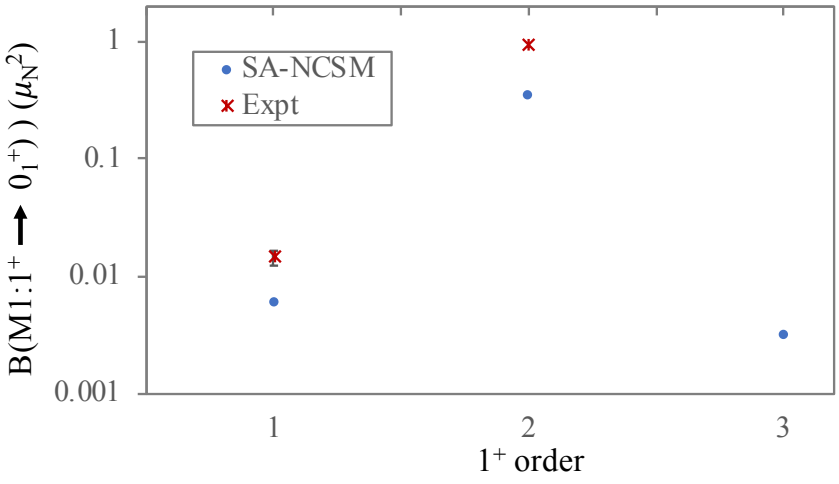

Figure 3.6. SA-NCSM calculations with NNLO$_{\rm opt}$ interaction for ^{12}C $B(M1:1^+\rightarrow 0^+_1)$ in $N_{\max}$=10. The abscissa shows the order of the states in the energy spectrum. All calculations are with HO parameter $\hbar\Omega$=15MeV. Experimental results (Expt) are from Ref. [77].

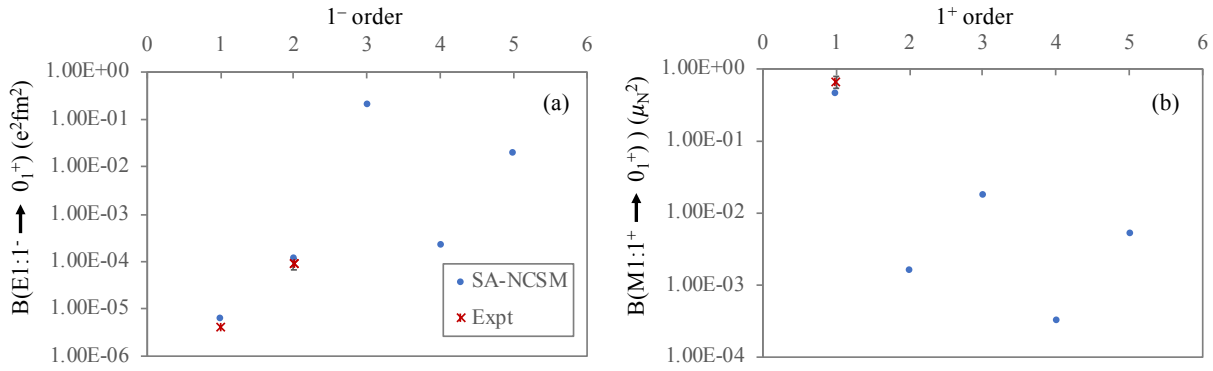

Figure 3.7. SA-NCSM calculations for ^{20}Ne (a) $B(E1 : 1^- \rightarrow 0^+_1)$ in $N_{\max}$=7, and (b) $B(M1 : 1^+ \rightarrow 0^+_1)$ in $N_{\max}$=6 using NNLO$_{\text{opt}}$ interaction. The abscissa shows the order of the states in the energy spectrum. All calculations are with HO parameter $\hbar\Omega$=15MeV. Experimental results (Expt) are from Ref. [78].

The ground state of ^{12}C is 0^+, which means that an $M1$ transition can occur only to or from a 1^+ state. Given that the 1^+ states are above 10 MeV in the ^{12}C energy spectrum, we limit our calculations to only the first three such states. The SA-NCSM calculations with NNLO$_{\text{opt}}$ interaction underpredict the $B(M1)$ strengths from the first two 1^+ states compared to experiment, however they do capture the correct orders of magnitude and show a clear dominance of the transition from the second 1^+ state in agreement with the experiment (Fig. 3.6). Since in neutrino scattering experiments often the total transition rate to an energy range is of interest, *ab initio* calculations can provide $B(M1)$ estimates that are not available from the experimental data.

Similar to ^{12}C the $M1$ transitions to the ground state of ^{20}Ne can occur only from 1^+ states. In this case the density of states is higher, hence we perform calculations for transitions from the first five 1^+ states. In addition, we provide calculations of the $B(E1)$ strengths to the ground state due to their dominant transition rates and comparatively large number of 1^- states in the low-lying spectrum of ^{20}Ne. Neglecting the higher multipole transitions, the $B(E1)$ and $B(M1)$ strengths can be used to calculate the average transition width from the ground state to excited states [75]. For the transitions from the lowest lying states, the SA-NCSM calculations agree with the experimental values (Fig. 3.7). The

calculations predict a large $E1$ transition strength from the third 1^- state, which will be dominant in the total gamma transition (Fig. 3.7a). In the 1^+ states, the lowest energy $M1$ transition prevails, with its strength being almost two orders of magnitude larger than the second largest $B(M1)$ (Fig. 3.7b).

4 Physics Beyond the Standard Model: Neutrinoless Double-beta Decay

4.1 Beta decay theory

Nuclear beta decay (β-decay) is the process in which a nucleus emits an electron or a positron and the lightest neutral lepton, neutrino. In the meantime the mass of the nucleus A remains unchanged, while the atomic number Z changes by ± 1. A β^--decay,

$$ {}^{A}_{Z}X \longrightarrow {}^{A}_{Z+1}X + e^- + \tilde{\nu}_e $$

may be considered as a transformation of one of the neutrons in the nucleus to a proton, and a β^+-decay,

$$ {}^{A}_{Z}X \longrightarrow {}^{A}_{Z-1}X + e^+ + \nu_e $$

as a transformations of one of the bound protons to a neutron. An important aspect of β-decays is that they occur purely due to the weak interaction. The general interaction Hamiltonian is given by

$$ H' = \sum_{i=1}^{5} (C_i H'_i + C'_i H''_i), \tag{4.1} $$

where $i = \{S, V, T, A, P\}$ each of which corresponds to scalar, vector, tensor, axial vector and pseudo-scalar interactions, respectively. The $C_i H'_i$ terms do not change their sign under coordinate inversion, while $C'_i H''_i$ change it to the opposite one. The necessity to have two such parts in the Hamiltonian arises because of the violation of parity in weak interactions [79].

For our discussion, we need to introduce the quantity called *helicity* of elementary particles. The helicity of a particle is defined as the projection of the intrinsic spin unit vector onto the direction of its momentum,

$$ h = \frac{\boldsymbol{\sigma} \cdot \mathbf{p}}{|\mathbf{p}|}, $$

where $\boldsymbol{\sigma} = \{\sigma_x, \sigma_y, \sigma_z\}$ is the spin unit operator, with σ_x, σ_y and σ_z being the Pauli matrices. Particles with positive helicity are referred to as "right handed" particles and negative-helicity particles are called "left handed" particles.

Experimental observations show that all the leptons emitted in β-decays are left-handed ($h < 0$), while all the antileptons right-handed ($h > 0$). It appears that the interaction terms that are scalars, pseudoscalars and tensors produce leptons and antileptons of both helicities under a parity transformation, thus leaving only vector operators V and axial vector operators A to be able to account for the observed result [67].

Since β-decay contains both a vector part and an axial part, there should be two separate operators corresponding to each of them. As we mentioned above, in its simplest form, β-decay may be regarded as transformation of a nucleon in the nucleus to another type, hence the nuclear operator must be one-body in nature (*i.e.* only one nucleon is involved at a time). This change can be expressed by the single-particle isospin raising or lowering operator $\tau^{\pm}$, which must be present in both V and A parts. The vector part is represented by

$$F = \sum_{j=1}^{A} \tau_j^{\pm}, \tag{4.2}$$

which is known as Fermi operator, and the axial part is

$$GT = \sum_{j=1}^{A} \boldsymbol{\sigma}_j \tau_j^{\pm}, \tag{4.3}$$

which is known as Gamow-Teller operator, where the summations span over the number of nucleons in the system.

The forms of Fermi and Gamow-Teller operators result in specific selection rules for the angular momentum and isospin of initial and final nuclear states. The Fermi term involves only the isospin raising or lowering operator, therefore the summation over the nucleons can

be performed explicitly,

$$\sum_{j=1}^{A} \tau_j^{\pm} = T^{\pm},$$

where $T^{\pm}$ raises or lowers the isospin projection, T_z, of the whole nucleus. Hence, the Fermi type β-decays do not change the total angular momentum J and the total isospin T, while the projection of the total isospin changes by exactly 1, $T_{z,f} = T_{z,i} \pm 1$, and the parity also remains unchanged. Note that a transition between $T_i = 0$ and $T_f = 0$ states is impossible, since the isospin projection cannot be anything but 0.

For the Gamow-Teller operator explicit summation over nucleons is impossible, yet the angular momentum and isospin selection rules can be derived from the form of the operator. Since $\tau_{\pm}$ and $\boldsymbol{\sigma}$ are spherical tensors of rank one (with respect to $\mathrm{SU}(2)_T$ and $\mathrm{SU}(2)_S$, respectively), then the total angular momentum and isospin can change by 0 or 1, but $J_i = 0 \to J_f = 0$ or $T_i = 0 \to T_f = 0$ transitions are forbidden. Again the parity remains unchanged and the isospin projection changes by 1.

Using the forms in (4.2) and (4.3) and multiplying them by appropriate coupling constants, the allowed β-decay transition rate will be given by the following equation (see Appendix B.1 for the derivation and definition of notations),

$$\begin{aligned} W &= \frac{m_e^5 c^4}{2\pi^3 \hbar^7} f(Z, E_0) \Big| \sum_{M_f} \Big[C_V \langle \zeta_f, J_f M_f; T_f T_{z,f} | \sum_{j=1}^{A} \tau_j^{\pm} | \zeta_i, J_i M_i; T_i T_{z,i} \rangle \\ &\quad + \; C_A \sum_{\mu} \langle \zeta_f, J_f M_f; T_f T_{z,f} | \sum_{j=1}^{A} \sigma_{\mu,j} \tau_j^{\pm} | \zeta_i, J_i M_i; T_i T_{z,i} \rangle \Big] \Big|^2 \\ &= \frac{m_e^5 c^4}{2\pi^3 \hbar^7} f(Z, E_0) C_V^2 \left[\langle F \rangle^2 + g_A^2 \langle GT \rangle^2 \right], \qquad (4.4) \\ \left[T_{1/2}^{\beta} \right]^{-1} &= \frac{f(Z, E_0)}{K} \frac{\langle f \| F \| i \rangle^2 + g_A^2 \langle f \| F \| i \rangle^2}{2J_i + 1} \qquad (4.5) \end{aligned}$$

where $g_A = C_A/C_V$, and $\langle F \rangle$ and $\langle GT \rangle$ are the reduced transition matrix elements of Fermi and Gamow-Teller operators for the wavefunctions of the parent and daughter nuclei. The $f(Z, E_0)$ is the Fermi integral (tables of calculated values of $f(Z, E_0)$ are available in Ref.

[80]), and $K = 6141.2 \pm 3.2$ [81] is a constant. The decay rate is related to the decay half-life by $T_{1/2} = \ln 2/W$. In literature, the decay rate is sometimes given as $[T_{1/2}]^{-1}$.

In certain cases, other faster reactions and ordinary β-decay in nuclei are forbidden, hence there is a possibility of double-beta decay. Double-beta decay is the process in which two electrons or two positrons are emitted from a nucleus. Such processes occur when the energy of a nucleus with odd protons and odd neutrons is higher than the energies of both of its neighboring even-even nuclei (*e.g.*, see red arrow in Fig. 4.1). Since proton-neutron pairing correlations can explain this even-odd energy difference it has been suggested that proton-neutron pairs play important role in calculating the double-beta decay rate. Double-beta decays are products of second-order perturbation induced by weak interaction and, therefore, have much smaller rates of occurrence or much longer half-lives ($T_{1/2} > 10^{20}$ years) than single β decays.

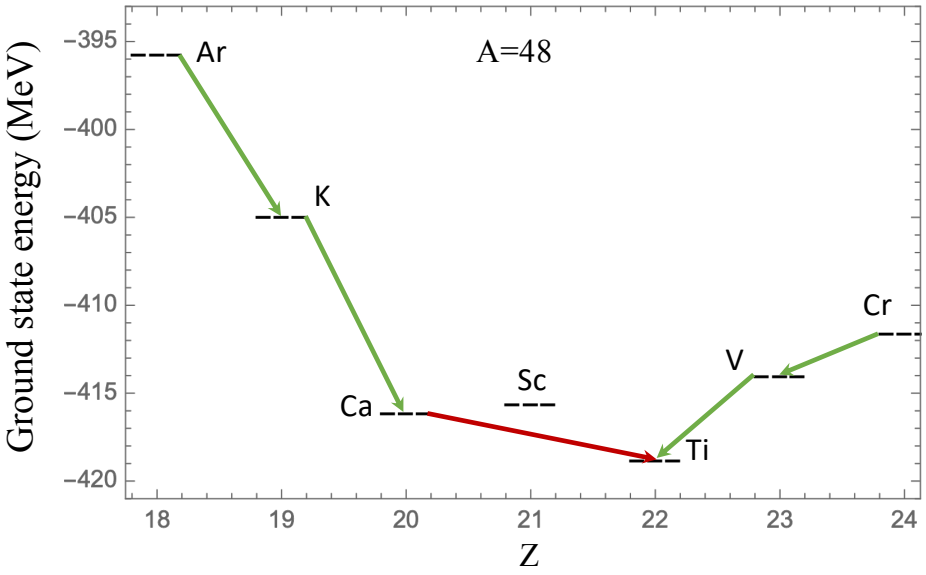

Figure 4.1. The experimental ground state energies of $A = 48$ nuclei (isobaric chain). The green arrows represent single β decay, and the red arrow displays the double-beta decay.

Double-beta decays with emission of two neutrinos (antineutrinos) have been detected for a number of nuclei. Nevertheless, one of the profound questions in modern physics is whether the double-beta decay can take place without emitting neutrinos. If neutrinos are

Majorana particles (meaning there is no distinction between neutrino and antineutrino) and have a non-zero mass, then the neutrinoless double-beta decay can be imagined as absorption of the neutrino from the first β-decay in the intermediate state which induces the ejection of the second charged lepton. The Feynman diagram of $0\nu\beta\beta$ from nuclear physics prospective (without the intermediate interaction bosons) is given in Fig. 4.2.

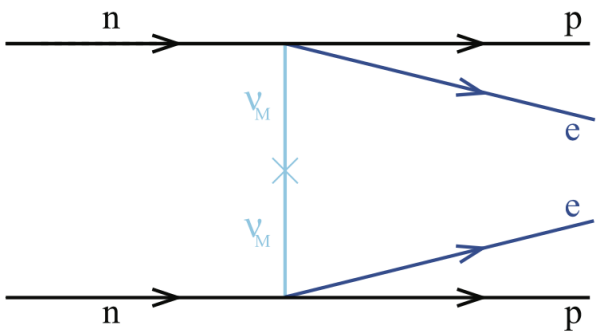

Figure 4.2. Schematic illustration of the Feynman diagram for $0\nu\beta\beta$. Two neutrons (n) decay into two protons (p), emitting two electrons (e). No neutrinos are emitted, implying that they are Majorana particles (ν_M). Figure adapted from [17].

As mentioned above, the process of neutrinoless double-beta decay is of great importance in the searches of physics beyond the Standard Model (BSM). Various collaborations around the world are performing experiments towards measuring the rate of this process in a number of nuclei. In order to provide guidance for the state-of-the-art experiments, theoretical calculations prove to be crucial.

In the present theory, the $0\nu\beta\beta$ decay rate is given by the following expression [17]

$$[T^{0\nu}_{1/2}]^{-1} = G_{0\nu}(Q,Z)|M_{0\nu}|^2 m^2_{\beta\beta}, \tag{4.6}$$

$$M_{0\nu} = \langle f|\,\hat{O}_{0\nu}\,|i\rangle \tag{4.7}$$

where $Q = E_f - E_i$ is the difference between the initial and final kinetic energies, Z is the number of protons in the mother nucleus, $G_{0\nu}(Q,Z)$ is a phase-space factor evaluated with high precision [82]. The nuclear matrix element, $M_{0\nu}$, contains Fermi (F), Gamow-Teller (GT) and Tensor (T) terms for $0\nu\beta\beta$ decay mediated by light Majorana-neutrino exchange

(derived by only including the long-distance neutrino-exchange contribution),

$$M_{0\nu} = M_{0\nu}^{GT} - \frac{g_V^2}{g_A^2} M_{0\nu}^{F} + M_{0\nu}^{T}. \tag{4.8}$$

The forms of each of these terms are given in Appendix A.2. The mass $m_{\beta\beta}$ is the effective Majorana mass of the electron neutrino given by

$$m_{\beta\beta} = \sum_{i=1}^{3} m_i U_{ei}^2,$$

with m_i being the neutrino masses (of the i^{th} mass eigenstate) and U_{ei} the elements of neutrino mixing matrix (also called Pontecorvo–Maki–Nakagawa–Sakata or PMNS matrix), the e subscript implies that only electron terms of the matrix are used. We note that there have been recently discovered corrections to the decay operator from the chiral effective field theory [83, 84]. These corrections have not yet been incorporated in any of the currently available theoretical calculations of $M_{0\nu}$. However, a newly published work in Ref. [85] provides a procedure on how to account for them in *ab initio* calculations.

Evaluation of $0\nu\beta\beta$ matrix elements, $M_{0\nu}$, is critical for several reasons. First, the amount of material necessary to achieve the sensitivity of a certain neutrino mass $m_{\beta\beta}$ is proportional to the decay half-life. The half-life depends on the square of the nuclear matrix element (4.7), hence an uncertainty of a factor of three in $M_{0\nu}$ will result in an uncertainty of almost an order of magnitude in the required amount of material. Second, having a more accurate matrix element would make it easier to choose an optimal isotope which has the lowest $0\nu\beta\beta$ half-life. Finally, the matrix element is vital for obtaining the absolute Majorana neutrino mass once the half-life is measured [17].

To calculate the $0\nu\beta\beta$ matrix elements in the SA-NCSM, we need to compute the wave-functions of the initial and final nuclei. Current computational resources allow the SA-NCSM to carry out reasonable calculations for only the lightest of the $0\nu\beta\beta$ candidates, ^{48}Ca, which after the decay transforms to ^{48}Ti. However, before performing calculations for the challeng-

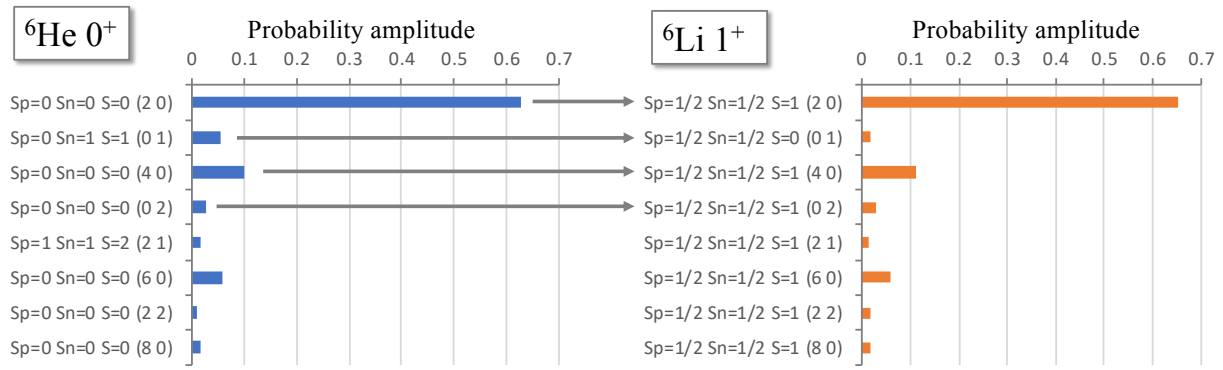

Figure 4.3. Calculated wavefunctions of ^{6}He and ^{6}Li ground states in $N_{\max}$=8 and $\hbar\Omega$=20 MeV, using NNLO$_{\text{opt}}$ interaction. Only configurations with probability amplitude $> 1\%$ are shown. The arrows show GT transitions connecting only the basis states with the same $(\lambda\,\mu)$.

ing $A = 48$ systems, it is necessary to verify the applicability of the model on the calculations of single and double-β decay of light nuclei.

4.2 GT results for light nuclei

Calculations of GT matrix elements with various models have shown systematic underprediction of the β decay half-lives for most of the nuclei. This problem has been commonly overcome by replacing the axial coupling constant ($g_A \approx 1.27$) that is involved in the expression for the half-life, with an effective smaller value [17, 86, 87]. However, the origin of this "quenching" of the g_A has not been understood until recent years. The recent *ab initio* studies have suggested this quenching to arise mainly from the missing correlations (complexity) in the wavefunctions of the earlier models and from the two-body currents in the weak interaction [88, 89]. In this section we present *ab initio* SA-NCSM calculations of GT transitions with non-renormalized NN interactions and unquenched g_A. The results help us validate the model for β decays and pave the path toward describing of other β decay quantities such as $0\nu\beta\beta$ matrix elements and recoil-order corrections.

The allowed β decay operators (F and GT) act only on the spin and isospin parts of wavefunctions and do not affect the spatial component of the basis states (see Eqs. 4.2 and 4.3), thus they cannot change the SU(3) quantum numbers of the initial basis state. In

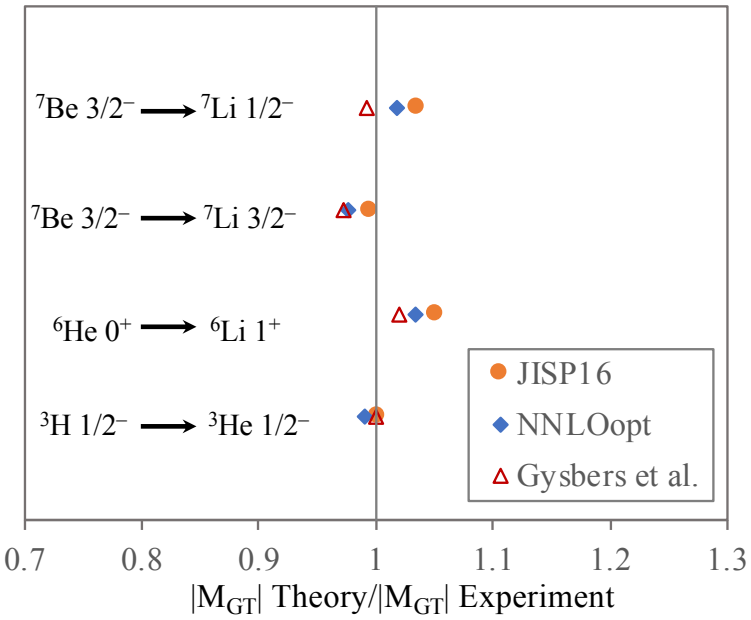

Figure 4.4. Theory-to-experiment ratio for the GT matrix elements of four strong transitions in light nuclei for the NNLO$_{opt}$ and JISP16 interactions compared to the Ref. [89] results with 2-body currents. All initial states are ground states.

other words, a basis state in the initial nucleus with a certain $(\lambda\,\mu)$ can only transition to a basis state with the same $(\lambda\,\mu)$ in the final nucleus (Fig. 4.3). Due to these selection rules, configurations of interest to allowed β decay are already within the model spaces used in the SA-NCSM in both initial and final nuclei. Along with the spin and isospin selection rules, this allows the SA-NCSM to significantly reduce the size of the allowed β-decay calculations. Moreover, before performing calculations, one can assess the size of the transition matrix elements by examining the major configurations in the initial and final wavefunctions.

Here, we perform calculations of GT matrix elements of ^{3}H and ^{6}He ground state β decays as well as ^{7}Be electron captures (Fig. 4.4). The typical quenching factor for $A < 16$ nuclei is 0.82 [86], which means that the earlier models have over-predicted the GT matrix elements in this region by about 15-20% compared to the experiment. Our calculations with non-renormalized NNLO$_{opt}$ and JISP16 interactions are in a close agreement with the experimental results, the largest deviation being about 5%. In addition, we compare our results with the calculations from Ref. [89] that include three-nucleon forces and the corresponding

two-body currents in the β decay. We agree with these results, even with only the (one-body) GT operator, showing the important role of correlations.

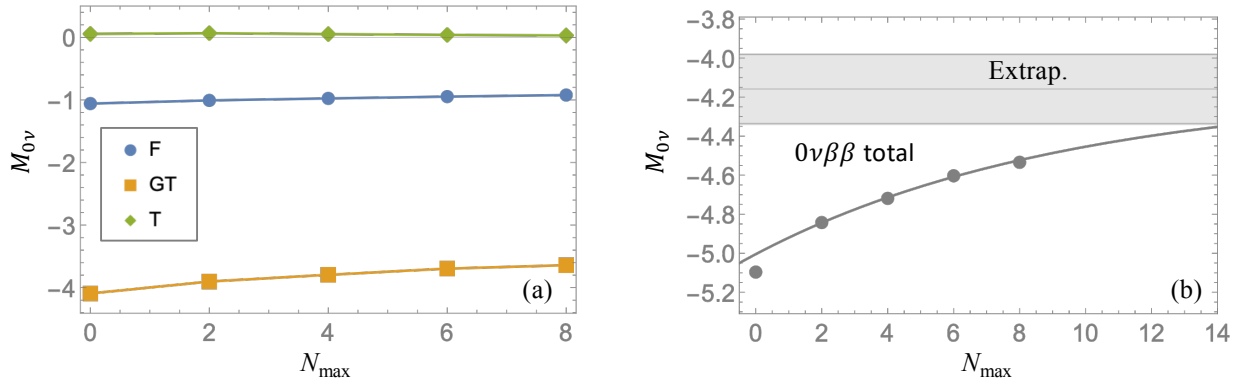

Figure 4.5. (a) Fermi (F), Gamow-Teller (GT) and Tensor (T) components and (b) total neutrinoless double-beta decay nuclear matrix element for the ^{6}He $\rightarrow^6$Be decay. The discrete points represent results of many-body calculations while lines represent fits. The gray band indicates the extrapolation uncertainty. Calculations are done using NNLO$_{\rm opt}$ interaction with $\hbar\Omega$=20 MeV HO parameter.

4.3 Double-beta decay for light nuclei

The calculations of $0\nu\beta\beta$ nuclear matrix element, $M_{0\nu}$, are extremely challenging since there is no experimental data that can be used to validate the results from various models. To compare different *ab initio* methods, benchmark calculations of $0\nu\beta\beta$ for decays that are energetically forbidden or happen in competition with single β decay have been performed for a number of light nuclei. In Refs. [90, 91], the nuclear matrix elements for ^{6,8,10}He and ^{10,12}Be were calculated with a quantum Monte Carlo (QMC) approach based on the AV18 interaction. Later, the same calculations were carried out with the local Norfolk chiral interaction for ^{6}He and ^{12}Be [92]. In Ref. [93] the NCSM calculations of ^{6}He $M_{0\nu}$ were benchmarked against the results from the multireference in-medium similarity renormalization group (MR-IMSRG) with a softened chiral interaction. Moreover, the $M_{0\nu}$ of ^{6,8,10}He, ^{14}C and ^{22}O were calculated with the NCSM and coupled-cluster theory in Ref. [15]. For most of these nuclei along with ^{10}Be, Ref. [94] calculated nuclear matrix elements with the importance-truncated (IT) NCSM [95] and two variants of IMSRG – the valence-shell (VS) IMSRG [96] and the in-medium generator coordinate method (IM-GCM) [14].

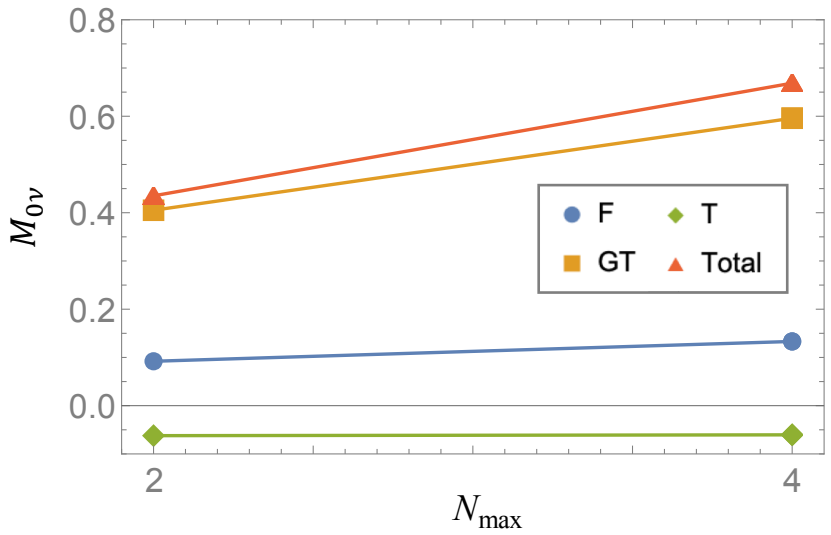

Figure 4.6. Fermi (F), Gamow-Teller (GT) and Tensor (T) components and the total neutrinoless double-beta decay nuclear matrix element for the ^{22}O $\rightarrow^{22}$Ne decay between the ground states. Calculations are done using NNLO$_{\rm opt}$ interaction with $\hbar\Omega$=15 MeV HO parameter.

To benchmark the SA-NCSM results of $0\nu\beta\beta$ against other methods, we perform calculations of $M_{0\nu}$ for the light ^{6}He $\rightarrow^{6}$Be and intermediate-mass ^{22}O $\rightarrow^{22}$Ne ground-state-to-ground-state decays. For both of these systems we use the NNLO$_{\rm opt}$ interaction. In the case of the $A = 6$ system, the calculations are done up to $N_{\max}$=8 model space with $\hbar\Omega$=20 MeV. For convenience, the $-g_V^2/g_A^2$ factor in Eq. (4.8) is absorbed into the Fermi contribution $M^F_{0,\nu}$. The results show that the GT matrix element is about four times larger than the Fermi contribution, whereas the tensor contribution is approximately two orders of magnitude smaller and of opposite sign (Fig. 4.5). Moreover, it is important to note that these matrix elements show a fast convergence as the model space increases. We use the three-parameter exponential formula in Eq. (6.11) to extrapolate the total $M_{0\nu}$, which yields $M_{0\nu} = -4.16 \pm 0.18$. The results are in agreement with the ones from Refs. [15, 93, 94].

Both of the nuclei invlolved in the ^{22}O$\rightarrow^{22}$Ne decay have enhanced collectivities as indicated by their large $B(E2)$ values [97], which has been a challenge to reproduce for *ab initio* models. As shown in the previous chapter, the SA-NCSM provides an accurate description of collective correlations in this mass region. Our calculations for the ^{22}O$\rightarrow^{22}$Ne decay per-

formed with $\hbar\Omega$=15 MeV show an increase of the nuclear matrix element with $N_{\max}$ (Fig. 4.6). We note that in the IT-NCSM results from Ref. [94] all components of the nuclear matrix element stay practically the same as the model space increases.

4.4 Neutrinoless double-beta decay for $A = 48$

After testing the SA-NCSM for computations of $0\nu\beta\beta$ in light nuclei, we calculate $M_{0\nu}$ for the ^{48}Ca decay to ^{48}Ti. An experimental program already exists that aims to measure the $0\nu\beta\beta$ half-life from the ^{48}Ca decay [98]. In addition, for this decay some calculations are available from *ab initio* models. In Ref. [14] $M_{0\nu}$ has been calculated using IM-GCM with a predicted value of $0.61^{+0.04}_{-0.05}$ for the total matrix element, while Ref. [15] has predicted the range of values $0.25 \leq M_{0\nu} \leq 0.75$ using the coupled cluster method.

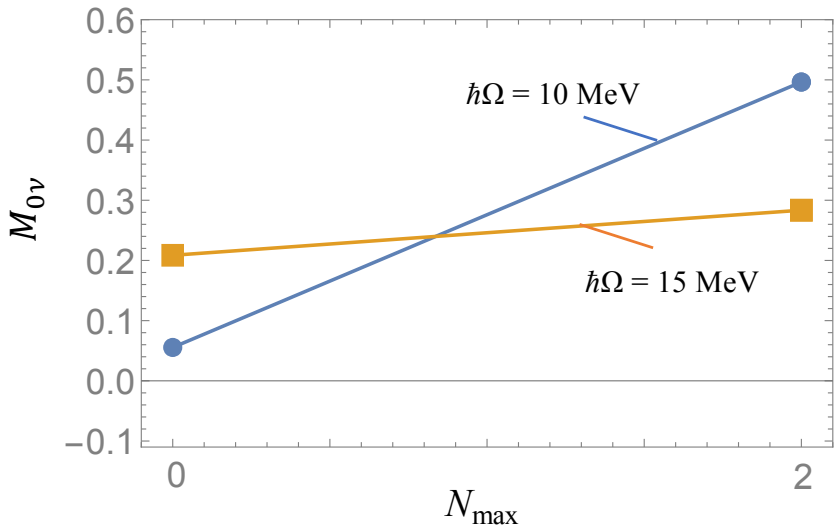

Figure 4.7. Neutrinoless double-beta decay nuclear matrix element for the ^{48}Ca $\rightarrow^{48}$Ti decay between the ground states. Calculations are done using NNLO$_{\text{opt}}$ interaction with $\hbar\Omega$=10 and 15 MeV HO parameter.

We use NNLO$_{\text{opt}}$ interactions with $\hbar\Omega$=10 and 15 MeV to calculate the ground states of ^{48}Ca decay to ^{48}Ti. The calculations indicate that the ^{48}Ti is dominated by a prolate deformation with a large quadrupole moment in a good agreement with the experimental value as shown in Ref. [99]. The ground state wavefunctions are then used to calculate $M_{0\nu}$ for $N_{\max}$=0 and 2 model spaces (Fig.4.7). The calculations are limited due to the

huge number of the configurations in the model space of the $A = 48$ systems. However, calculations in larger model spaces are currently underway. Based on these results we can put a lower limit of 0.50 on the nuclear matrix element for the ^{48}Ca $0\nu\beta\beta$ decay. This value agrees with the results from other *ab initio* models mentioned above. Additional calculations in larger model spaces will help provide a more robust prediction.

In short, we applied the SA-NCSM to calculate $0\nu\beta\beta$ matrix elements for the ^{6}He $\rightarrow^{6}$Be, ^{22}O $\rightarrow^{22}$Ne and ^{48}Ca $\rightarrow^{48}$Ti decays. Even though the first two transitions are energetically forbidden, they provide a testbed for implementing the newly developed method. Our current result for the ^{48}Ca nuclear matrix element is in agreement with other *ab initio* models and it is below the phenomenological predictions shown in Fig. 1.1.

5 Physics Beyond the Standard Model: ^{8}Li Beta Decay and Recoil-order Corrections

This chapter presents *ab initio* SA-NCSM calculations that place unprecedented constraints on recoil corrections in the β decay of ^{8}Li, by identifying a strong correlation between them and the ^{8}Li ground state quadrupole moment in large-scale *ab initio* calculations. The results are essential for improving the sensitivity of high-precision experiments that probe the weak interaction theory and test physics beyond the Standard Model. In addition, our calculations predict a 2^+ state of the $\alpha+\alpha$ system that is energetically accessible to β decay but has not been observed in the experimental ^{8}Be energy spectrum, and has an important effect on the recoil corrections and β decay for the $A = 8$ systems. This state and an associated 0^+ state are notoriously difficult to model due to their cluster structure and collective correlations, but become feasible for calculations in the *ab initio* symmetry-adapted no-core shell-model framework.

5.1 ^{8}Li β decay and theory

The left-handed vector minus axial-vector (V−A) structure of the weak interaction was theoretically established in late 1950's and early 1960's [100, 101] guided in large part by a series of β-decay experiments [102–104] and later was incorporated in the Standard Model of particle physics. However, in its most general form, the weak interaction can also have scalar, tensor, and pseudoscalar terms as well as right-handed currents. Beta-decay experiments continue to pursue increasingly sensitive searches for these additional contributions. Various experiments [23, 104–106] have constrained the tensor part of the interaction where the limits are the least stringent compared to the other non-standard-model terms [107, 108]. These experiments have achieved remarkable precision, but further improvements require confronting the systematic uncertainties that stem from higher-order corrections (referred to as recoil-order terms) in nuclear β decay. These terms are inherently small compared to the allowed β decay terms; however, current experiments have reached a precision where even subtle distortions matter.

Measurements of recoil-order terms have provided important information about nuclear structure [109], the existence of second-class currents [110–112] and the accuracy of the conserved vector current (CVC) hypothesis [24, 25, 111, 113]. For CVC tests in particular, a number of experiments have been performed to study the β decay of ^{8}Li (Fig. 5.1). The recoil-order terms have been extracted from the β-α angular correlations [113, 114] or β-spin alignment correlations [25] of the β decay to ^{8}Be, which subsequently breaks up into two α particles. In addition, they have been deduced from γ decays of the doublet 2^+ states near 17 MeV in the ^{8}Be spectrum, which contain the isobaric analogue of the ^{8}Li ground state [111]. Due to their small size, most of the experimentally extracted recoil-order terms have large uncertainties. The β decay of ^{8}Li has also been studied to search for weak tensor currents through the measurements of β-$\bar{\nu}$-α correlations with trapped ions [23, 106, 115], including the most stringent limit on a tensor contribution to date [116]. One of the largest uncertainties in these experiments comes from the recoil-order corrections.

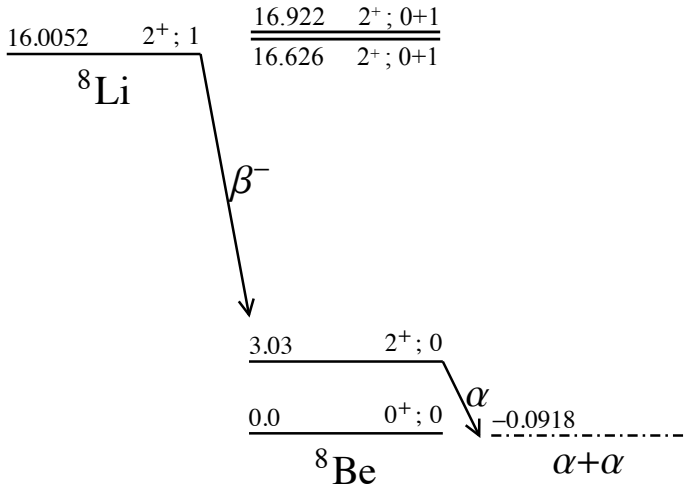

Figure 5.1. Decay scheme for β decay of ^{8}Li ground state (denoted as g.s.) to experimentally known levels in ^{8}Be. Energies are in MeV.

In this chapter, we report the first *ab initio* calculations of recoil-order terms in the β decay of ^{8}Li . These calculations achieve highly reduced uncertainties compared to the experimentally extracted values of Ref. [25]. They help decrease the systematic uncertainties

on the tensor-current estimates in the weak interaction reported in Ref. [116], and are of interest to experimental tests of the CVC hypothesis [111]. We also provide evidence that the β transition strength of the ^{8}Li decay is largely affected by a disputed low-lying 2^+ state (sometimes referred to as an "intruder" state) below 16 MeV in the ^{8}Be spectrum. Our calculations in unprecedentedly large model spaces support the existence of low-lying states with a large overlap with the $\alpha + \alpha$ s- and d-waves. Indeed, a very broad 2^+ state along with a lower 0^+ were initially proposed by Barker from the R-matrix analysis of $\alpha + \alpha$ scattering and the β decays of ^{8}Li and ^{8}B [117–119]. Even though such states have not been directly observed experimentally, some earlier theoretical studies have predicted them in the low-lying spectrum of ^{8}Be [120–122]. Furthermore, there has been a recent experimental indication in favor of intruder states below 16 MeV [123].

The use of chiral effective field theory interactions [124–127] in the SA-NCSM enables nuclear calculations informed by elementary particle physics, while the symmetry-adapted basis allows us to achieve ultra-large model spaces imperative for the description of challenging features in the ^{8}Be states, such as clustering and collectivity. It uses a harmonic oscillator (HO) basis with frequency $\hbar\Omega$ and a model space with an $N_{\max}$ cutoff, which is the maximum total HO excitation quanta above the lowest HO configuration for a given nucleus. These parameters are related to infrared and ultraviolet cutoffs [128], which can be understood as the effective size of the model space in which the nucleus resides, and its grid resolution, respectively. The calculations become independent of $\hbar\Omega$ at $N_{\max} \to \infty$, providing a parameter-free *ab initio* prediction. The SA-NCSM results exactly reproduce those of the NCSM [129, 130] for the same nuclear interaction. However, by utilizing the emergent symplectic $\mathrm{Sp}(3, \mathbb{R})$-symmetry in nuclei [2], the SA-NCSM can expand the model space by a physically relevant subspace, which is only a fraction of the complete NCSM space, thereby including localized-α degrees of freedom within the interaction effective range [131].

In this chapter we adopt various chiral nucleon-nucleon (NN) potentials without renormalization in nuclear medium: Entem-Machleidt (EM) N^{3}LO [126], NNLO$_{\mathrm{opt}}$ [32], as well as

NNLO_{sat} [132] with the three-nucleon (3N) forces, hierarchically smaller than NN, added as averages [99]. For comparison, we present results with the soft JISP16 phase-equivalent NN interaction [30] discussed in Chapter 2. We use $\hbar\Omega$=15-25 MeV for $\text{N}^3\text{LO-EM}$, NNLO_{opt}, and JISP16, and $\hbar\Omega$=16 MeV for NNLO_{sat}, unless otherwise stated. The NNLO_{opt} is used without 3N forces that have been shown to contribute only minimally to the 3- and 4-nucleon binding energy. Furthermore, the NNLO_{opt} NN potential has been found to reproduce various observables, including the ^{4}He electric dipole polarizability [133], the challenging analyzing power for elastic proton scattering on ^{4}He, ^{12}C, and ^{16}O [134], along with the B(E2) transition strengths for ^{21}Mg and ^{21}F shown in Chapter 3 that are extremely difficult to be reproduced within an *ab initio* framework.

For the purposes of this study, the quadrupole moment of the ^{8}Li ground state, $Q(2^+_{\text{g.s.}})$, for which SA-NCSM calculations with the NNLO_{opt} NN are extrapolated to the infinite model-space size, is shown to reproduce the experimental value within the many-body model uncertainties (Fig. 5.2), in close agreement with the extrapolated value of Ref. [135] that uses renormalized NN+3N chiral potentials. The model uncertainties are based on variations in the model-space size and resolution, and extrapolations use the Shanks method of Ref. [2].

The recoil-order terms are generally neglected in β-decay theory since they are of the order of q/m_N or higher, where q is the momentum transfer (typically several MeV) and m_N is the nucleon mass. Thus, for most β decays, the recoil effect is typically less than a percent of the dominant Fermi and Gamow-Teller (GT) contributions. However, for measurements of sufficiently high precision, these terms must be included in the analysis especially when the leading contributions are suppressed and the recoil-order terms are unusually large, as in the case of the decay to ^{8}Be.

The recoil-order terms in nuclear β decay have been derived using the impulse approximation in Ref. [24]. Here, we consider the the second forbidden axial vector (j_2 and j_3), induced tensor (d) and weak magnetism (b) terms, along with the GT matrix element (c_0), since they account for the recoil-order corrections and their comparatively large uncertainties

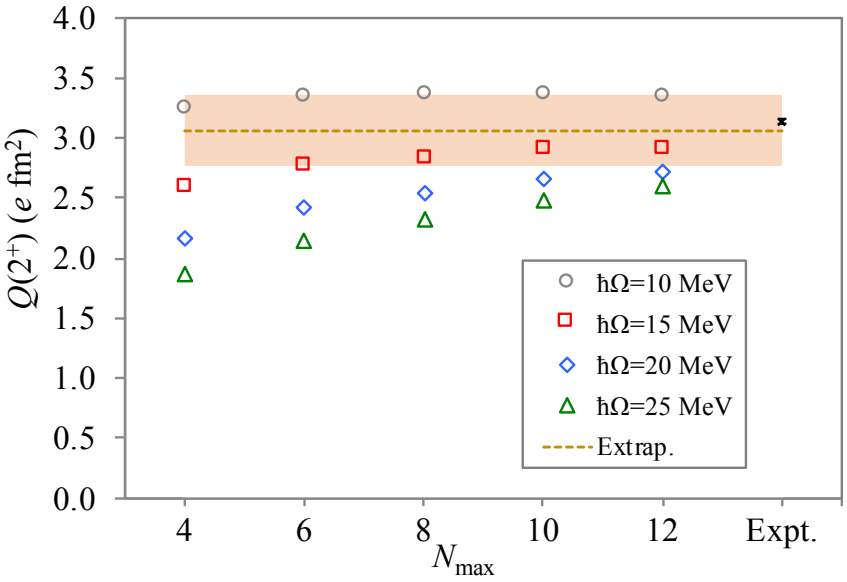

Figure 5.2. Calculated ^{8}Li ground state quadrupole moment $Q(2^+)$ [e fm^2] using the NNLO$_{\rm opt}$ NN for different model space sizes and resolutions (open symbols), along with the infinite-size extrapolated value (dashed line) and the corresponding many-body uncertainty (shaded area). The experimental value ("Expt.") is from Ref. [136]. Figure adapted from Sargsyan *et al.* [137]

in the measurements of weak interaction tensor currents due to the relatively large error bars on them measured by Ref. [25]. The c_0, $j_{2,3}$, d and b terms are given by the expressions

$$
\begin{aligned}
c_0(q^2) &= (-)^{(J'-J)}\frac{g_A(q^2)}{\sqrt{2J+1}}\langle J'||\sum_i^A \tau_i^{\pm}\sigma_i||J\rangle = (-)^{(J'-J)}\frac{g_A(q^2)}{\sqrt{2J+1}}M_{GT},\\
j_K(q^2) &= -(-)^{(J'-J)}\frac{2}{3}\frac{g_A(q^2)}{\sqrt{2J+1}}\frac{(Am_Nc^2)^2}{(\hbar c)^2}\langle J'||\sum_i^A \tau_i^{\pm}[Q_i\times\sigma_i]^K||J\rangle\,, \text{with } K=2,3,\\
d(q^2) &= (-)^{(J'-J)}A\frac{g_A(q^2)}{\sqrt{2J+1}}\langle J'||\sum_i^A \tau_i^{\pm}\sqrt{2}[L_i\times\sigma_i]^1||J\rangle\\
b(q^2) &= A\frac{(-)^{(J'-J)}}{\sqrt{2J+1}}\Big[g_M(q^2)\langle J'||\sum_i^A \tau_i^{\pm}\sigma_i||J\rangle + g_V(q^2)\langle J'||\sum_i^A \tau_i^{\pm}L_i||J\rangle\Big],
\end{aligned}
\tag{5.1}
$$

where $g_V(0)=1$ and $g_A(0)\approx 1.27$ are the vector and axial coupling constants (unitless), A is the mass number, $J(J')$ is the total angular momentum of the initial (final) nucleus. The $\tau_i/2$,

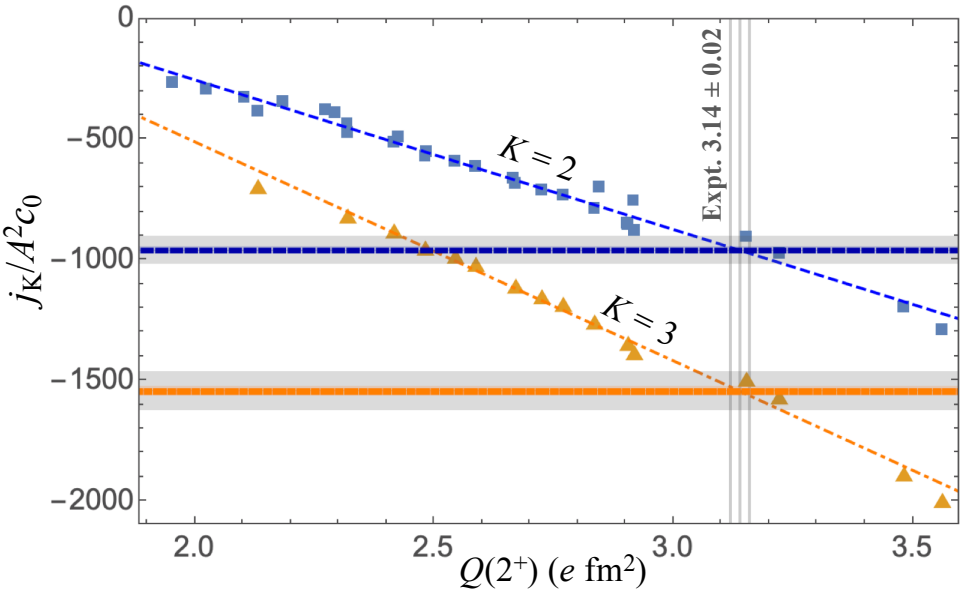

Figure 5.3. Calculated j_2/A^2c_0 and j_3/A^2c_0 (squares and triangles, respectively) for the ^{8}Li β decay to the lowest 2^+ state in ^{8}Be vs. calculated ^{8}Li ground state quadrupole moment Q(2^+) [e fm^2]. Calculations use the NNLO$_{\rm opt}$, NNLO$_{\rm sat}$ and N3LO chiral potentials, as well as the JISP16 NN, in model spaces $N_{\rm max}$=6 to 12. The upper and lower horizontal lines correspond to the j_2/A^2c_0 and j_3/A^2c_0 values, respectively, predicted from the linear regression using the experimental ^{8}Li quadrupole moment [136]. The corresponding uncertainties are shown by the line thickness. The total uncertainties, which also include the linear regression slope uncertainty, are shown by the gray bands. Figure adapted from Sargsyan *et al.* [137]

$\sigma_i/2$, $Q_i = \sqrt{16\pi/5}r_i^2 Y_{2\mu}(\theta_i,\phi_i)$, and L_i are the isospin, intrinsic spin, quadrupole moment and angular momentum operators, respectively, of the $i^{\rm th}$ particle. All of the reduced matrix elements are with respect to the total angular momentum (not isospin). The additional factor, $(-)^{(J'-J)}\sqrt{2J+1}$, compared to Ref. [24] arises from the difference in the convention of Wigner-Eckart theorem. The convention we use can be found in, e.g., Ref. [66]. M_{GT} is the conventional GT matrix element. These recoil-order terms, usually reported as decay-agnostic ratios j_2/A^2c_0, j_3/A^2c_0, d/Ac_0 and b/Ac_0, enter into the expression of the β decay rate for nuclei undergoing delayed α-particle emission [23, 24, 116, 138].

5.2 Recoil corrections from the SA-NCSM

Remarkably, we identify a strong correlation between $j_{2,3}/A^2c_0$ and the ^{8}Li ground state quadrupole moment based on calculations across several interactions, $N_{\rm max}$ and $\hbar\Omega$ parame-

ters (Fig. 5.3, using $N_{\max}$= 6 to 12 for NNLO$_{\rm opt}$, and to 8 for the other interactions). A linear regression along with the combination of the correlation to $Q(2^+_{\rm g.s.})$ and its experimental value of 3.14(2) $e\,\mathrm{fm}^2$ [136] lead to reduced uncertainties on our predictions:

$$\frac{j_2}{A^2 c_0} = -962 \pm 12 \pm 55, \quad \frac{j_3}{A^2 c_0} = -1547 \pm 18 \pm 78. \tag{5.2}$$

Here, the first set of uncertainties uses the quadrupole moment experimental uncertainties given the linear regression slope, and the second set arises from the slope uncertainty multiplied by the $Q(2^+_{\rm g.s.})$ experimental value. This correlation is important, as we can reduce the problem of calculating a matrix element that depends on cluster physics in ^{8}Be to a bound state observable in ^{8}Li.

Table 5.1. β recoil-order matrix elements from SA-NCSM. Results for the 2^+_1 j_2/A^2c_0 and j_3/A^2c_0 are from Eq. (5.2); all other calculations use NNLO$_{\rm opt}$ and have error bars from variations in $\hbar\Omega$ by 5 MeV and in model space sizes up to $N_{\max}$=16 (12) for j_K/A^2c_0 (d/Ac_0 and b/Ac_0).

	j_2/A^2c_0	j_3/A^2c_0	d/Ac_0	b/Ac_0
2^+_1	-962 ± 56	-1547 ± 80	10.0 ± 1.0	6.0 ± 0.4
2^+_2	-10 ± 10	-80 ± 30	-0.5 ± 0.5	3.7 ± 0.4
Doublet 1 2^+_3	12 ± 5	-60 ± 15	0.3 ± 0.2	3.8 ± 0.2
Doublet 2 2^+_4	11 ± 3	-65 ± 11	0.2 ± 0.2	3.8 ± 0.2

Most significantly, with the new predictions (5.2), the uncertainty from the recoil-order corrections on the tensor current contribution to the weak interaction presented in Ref. [138] is reduced by over 50% [116]. The β recoil-order terms, including the b and d terms, for the lowest four SA-NCSM 2^+ states, are summarized in Table 5.1. The d/Ac_0 prediction for 2^+_1 is based on a correlation similar to the one for $j_{2,3}/A^2c_0$ (Fig. 5.4). Besides tensor-current probes, these b weak magnetism predictions are of interest to experiments that test the CVC hypothesis, while d is of importance to determining the existence of second-class currents [111].

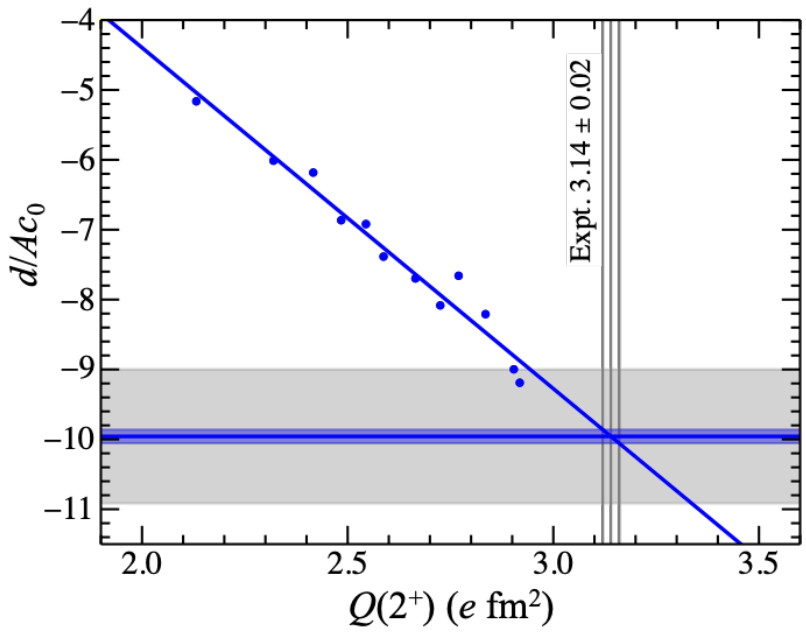

Figure 5.4. Calculated d/Ac_0 for the ^{8}Li β decay to the lowest 2^+ state in ^{8}Be vs. calculated ^{8}Li ground state quadrupole moment Q(2^+) [e fm^2]. Calculations use the NNLO$_{\rm opt}$ chiral potential in model spaces $N_{\rm max}$=6 to 12. The horizontal line corresponds to the d/Ac_0 value predicted from the linear regression using the experimental ^{8}Li quadrupole moment [136]. The blue band indicates the uncertainty from experiment. The total uncertainty, which also includes the linear regression slope uncertainty, is shown by the gray band. Figure adapted from Sargsyan *et al.* [137].

5.3 Untangling the physics of ^{8}Be

The experimentally deduced values for the j_K/A^2c_0, d/Ac_0 and b/Ac_0 presented in Ref. [25] ($j_2/A^2c_0 = -490 \pm 70$, $j_3/A^2c_0 = -980 \pm 280$, $d/Ac_0 = 5.5 \pm 1.7$ and $b/Ac_0 = 7.5 \pm 0.2$) are comparable but different from our predicted values. These experimental results were obtained through a global fit to β-spin alignment and β-α angular correlation data [114] from ^{8}Li and ^{8}B β decays. Due to the small size of higher-order effects and relatively large statistical uncertainties, the $j_{2,3}/A^2c_0$ and d/Ac_0 were assumed in Ref. [25] to be independent of the ^{8}Be excitation energy. Thus, the results were averaged over the entire β decay spectrum. In contrast, the SA-NCSM wavefunctions are for individual states, hence, the predictions in Eq. (5.2) are for the lowest 2^+ state only, which is the dominant transition for the ^{8}Li β decay. A small branching fraction is observed to the doublet 2^+ states near 17

MeV due to their resonant nature (Fig. 5.1).

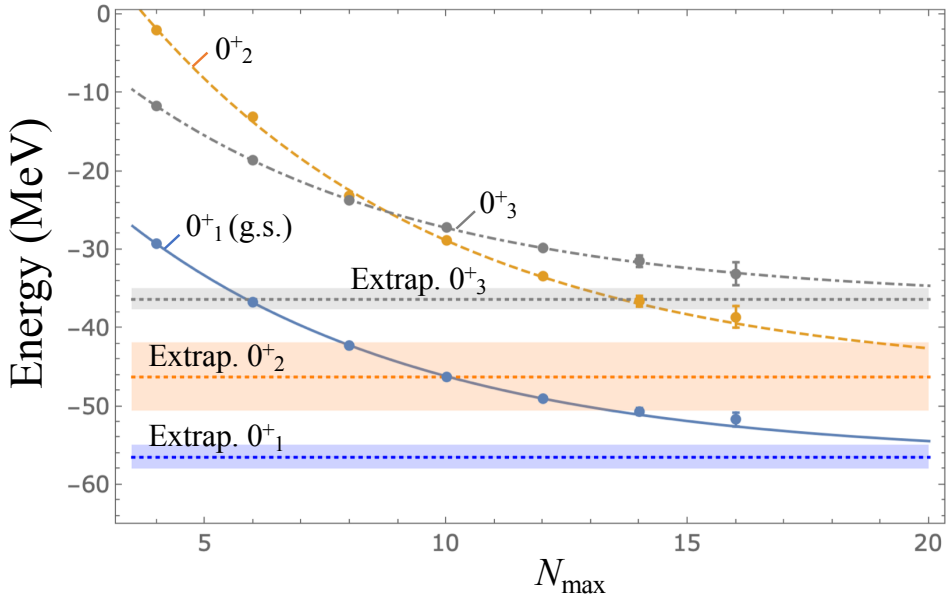

Figure 5.5. Calculated ^{8}Be low-lying 0^+ state energies illustrated for the NNLO$_{\text{opt}}$ chiral potential ($\hbar\Omega$=15 MeV) vs. the model space size, together with the extrapolated values (dotted lines) and their extrapolation uncertainties (bands). Extrapolations use complete model spaces up to N_{max}=12 and do not include the N_{max}=14 and 16 SA selected model spaces shown with uncertainties determined by the selection. The measured 0^+_1 energy is −56.5 MeV [139]. Figure adapted from Sargsyan *et al.* [137].

However, the SA-NCSM calculations indicate the existence of another 2^+ state below 16 MeV and a corresponding 0^+ state that largely overlap with the α+α system (Fig. 5.5, see also Fig. 5.8). This state would be accessible to the ^{8}Li or ^{8}B β decays through allowed transitions. In the SA-NCSM calculations, a 2^+ state and an associated lower 0^+ state quickly decrease in energy as the model space size increases, similarly to the Hoyle-state rotational band in ^{12}C [140]. These states are observed in calculations with all the realistic interactions under consideration, and extrapolations to the infinite model space determine their energies between 5 and 15 MeV above the ground state (Fig. 5.6), corroborating earlier estimates [117,118,120]. The extrapolations are performed using the three-parameter exponential formula of Ref. [73]. For example, for the NNLO$_{\text{opt}}$ NN, we observe the fastest convergence of the energy of these states for $\hbar\Omega$=15 MeV, and in this case, this 0^+ state

becomes the lowest excited 0^+ in the spectrum after $N_{\max}$=10 (Fig. 5.5). It should be noted that the third 0^+ converges to 20.1 ± 1.5 MeV and has a structure similar to the doublet 2^+ states, and an isospin $T = 1$. This state is not seen in the currently available experimental spectrum and it is likely to be the isobaric analogue of the low-lying 0^+ in ^{8}Li predicted by recent *ab initio* calculations [135, 141].

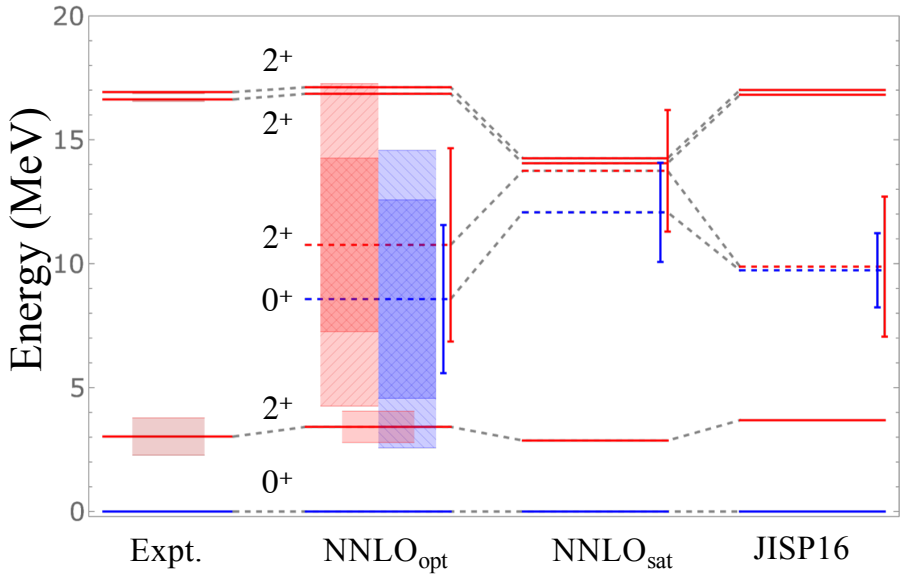

Figure 5.6. Low-lying states in ^{8}Be from extrapolations with NNLO$_{\rm opt}$, JISP16 and NNLO$_{\rm sat}$ calculations, compared to experiment (Expt.). The extrapolation uncertainties for the new states (dashed levels) shown as error bars are based on variations in the model space size and selection. For the lowest two 0^+ and 2^+ states, we show the α width estimates (shaded areas) and their uncertainties (lighter shades) across threshold energy variations for NNLO$_{\rm opt}$ and $\hbar\Omega$=15 MeV, compared to experimentally deduced values; the small width for the lowest 0^+ resonance (not shown) is 5.7 eV compared to 5.57 eV [142]. Figure adapted from Sargsyan *et al.* [137].

The calculated low-lying states in ^{8}Be are in good agreement with experiment across various interactions (Fig. 5.6). Specifically, we show infinite-size results for NNLO$_{\rm opt}$ and JISP16 NN across several $\hbar\Omega$ values. The $\hbar\Omega$=16-MeV NNLO$_{\rm sat}$ results include the average 3N contribution determined for a given isospin (for ^{8}Be, the contribution to the binding energy in $N_{\max}$=12 is 1.51 MeV, resulting in a total extrapolated binding energy of 56.8 MeV). For NNLO$_{\rm opt}$ NN and the case of the fastest energy convergence of the 0^+_2 and 2^+_2 states,

($\hbar\Omega$=15 MeV), we estimate the α widths by projecting the $N_{\max}$=16 SA-NCSM wavefunctions onto $\alpha + \alpha$ cluster states following the procedure of Ref. [131]. For this the ^{8}Be and ^{4}He wavefunctions are expressed in terms of Sp$(3,\mathbb{R})$ basis states each associated with a certain intrinsic shape. In SA-NCSM the many-body wavefunctions can be decomposed in terms of collective Sp$(3,\mathbb{R})$ basis states. As shown in Ref. [2], each irreducible representation (irrep) of the symplectic Sp$(3,\mathbb{R})$ group describes an equilibrium shape within a nucleus that vibrates and rotates. These irreps are labeled by the SU(3) quantum numbers $(\lambda\,\mu)$ of the equilibrium shape with an average deformation given by the familiar shape parameters, the deformation β and triaxiality γ [143, 144]. Typically, the nuclei are comprised of only a few shapes, often a single shape (a single symplectic irrep) as for the ^{8}Be ground state and the corresponding lowest 2^+ state (Fig. 5.7). However, for the 0^+_2 and 2^+_2 states, the wavefunction consists of a mixture of three dominant prolate shapes (Fig. 5.8). Thus, one needs calculations in ultra-large model spaces and consideration of all the major shapes to obtain an accurate description of these sates. For ^{8}Be, we need to consider three dominant prolate shapes with contributions of 75%, 4% and 3% (totaling 82%) to the ground-state 0^+ resonance, and 46%, 15%, and 11% (totaling 72%) to the second 0^+ state (similarly for the 2^+ states). These shapes extend to 18 HO shells and start at the most deformed configurations among those in the valence shell, $2\hbar\Omega$ and $4\hbar\Omega$ excitations.

The SA-NCSM with NNLO$_{\rm opt}$ estimates the α+α threshold at -104 keV relative to ^{8}Be, based on extrapolations of the ^{4}He and ^{8}Be binding energies. To reduce uncertainties in the width of the ground state, we use the experimental threshold of -92 keV. For all other states we use the extrapolated threshold, with the width uncertainties arising from the upper and lower limits on the state energies above the threshold (Fig. 5.6). These widths are in good agreement with experimentally deduced values [142] and earlier theoretical studies [145–147].

Intruder 0^+ and 2^+ states in the low-lying spectrum of ^{8}Be were proposed in the late 1960's by Barker from concurrent R-matrix fits to scattering, reaction, and decay data associated with the ^{8}Be nucleus [117, 118]. The inclusion of an intruder 2^+ state below 16 MeV in the

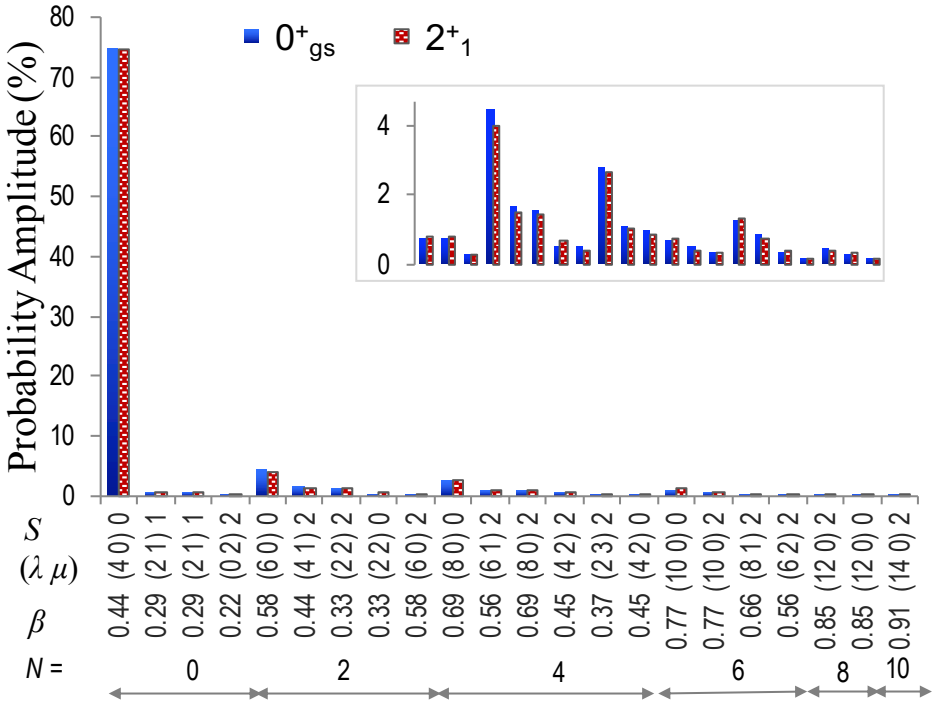

Figure 5.7. Symplectic $\mathrm{Sp}(3,\mathbb{R})$ irreps that compose the lowest $0^+_{\text{g.s.}}$ and 2^+_1 states of ^{8}Be; each irrep is specified by its equilibrium shape, labeled by β and the corresponding SU(3) labels $(\lambda\,\mu)$ together with total intrinsic spin S. N denotes the total HO excitations. Insets: the same irreps but without the terms larger than 5%. Figure adapted from Sargsyan *et al.* [137].

R-matrix fits of β decays significantly changes the GT value for the first 2^+ state. Indeed, the analysis in Ref. [148] shows that the extracted GT value for a decay to the lowest 2^+ state decreases by almost 1.5 times when a low-lying 2^+ intruder is present. The energies from the R-matrix fits for the intruder 0^+ and 2^+ states proposed by Barker were around 6 MeV and 9 MeV, respectively, with α widths of > 7 MeV. These excitation energies agree with the SA-NCSM extrapolated results given the error bars (Fig. 5.5), as well as with the predicted widths.

The SA-NCSM reveals large differences between the β recoil-order terms to the lowest two 2^+ states, the most notable being for the j_K/A^2c_0 terms where the values differ by almost two orders of magnitude (see Table 5.1). The large difference is mainly due to the small M_{GT} for 2^+_1 as compared to the other states. Notably, the strong excitation energy dependence of the recoil-order terms due to the presence of 2^+_2 significantly affects the constraints on

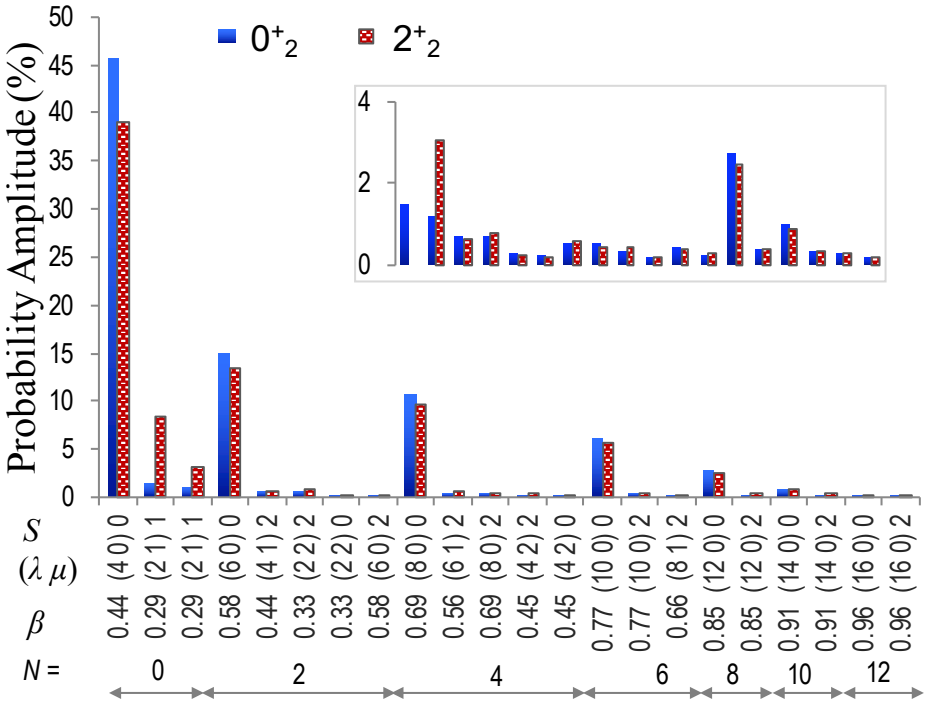

Figure 5.8. Symplectic $\mathrm{Sp}(3,\mathbb{R})$ irreps that compose the second 0_2^+ and 2_2^+ states of ^{8}Be; each irrep is specified by its equilibrium shape, labeled by β and the corresponding SU(3) labels $(\lambda\,\mu)$ together with total intrinsic spin S. N denotes the total HO excitations. Insets: the same irreps but without the terms larger than 5%. Figure adapted from Sargsyan *et al.* [137].

the weak tensor currents [116]. However, angular-correlation experiments can minimize this issue by restricting their analysis to decays centered on the broad 2_1^+ state.

In summary, the *ab initio* SA-NCSM calculated the size of the recoil-order terms in the β decay of ^{8}Li. It showed that states of ^{8}Be not observed in the experimental energy spectrum have important effect on $j_{2,3}/A^2c_0$, b/Ac_0 and d/Ac_0 form factors and can explain the M_{GT} discrepancy in the $A = 8$ systems. The results significantly reduce the uncertainty on these recoil-order corrections and help improve the sensitivity of high-precision β-decay experiments that probe the V−A structure of the weak interaction [116].

Table 5.2. *Ab initio* M_{GT}, c_0 and $\log(ft)$, compared to the experimentally deduced values. Ref. [148] includes both evaluations with an intruder 2^+ state (denoted by *) around 8 MeV similar to Ref. [119], and without it.

		2_1^+		2_2^+
	$\lvert M_{\mathrm{GT}}\rvert$	$\lvert c_0\rvert$	$\log(ft)$	$\log(ft)$
$\mathrm{NNLO_{opt}}$	0.16(1)	0.09(1)	5.90	> 5.06
$\mathrm{NNLO_{sat}}$	0.21(3)	0.12(2)	5.64	> 5.05
JISP16	0.23(4)	0.13(2)	5.54	> 4.28
Expt., Ref. [119]	0.190	0.108	5.72	5.27
Expt., Ref. [148]*	0.204	0.116	5.66	5.2
Expt., Ref. [148]	0.284	0.163	5.37	–

6 Clustering in Nuclei: A Bridge to Reaction Observables

6.1 Spectroscopic overlaps: application to ^{8}Be

Studying nuclei in terms of cluster substructures has played a major role in the description of nuclear structure and reaction observables. Representations of nuclei as α conjugates (that is, with multiple of two protons and two neutrons) and as single-nucleon plus $A-1$ systems have been of particular interest due to their importance for modeling reactions that take place in stellar environments. Such reactions include the prominent triple-α process and single-nucleon capture reactions [140, 149]. In particular, all the low-lying states in ^{8}Be discussed in the previous chapter decay almost exclusively into two α particles within immensely short timescales ($T_{1/2} < 10^{-16}$s). Hence, the the description of ^{8}Be as a two-α cluster system has been a common practice for many decades [150, 151]. Moreover, the $\alpha + \alpha$ reaction is the main production mode of ^{8}Be in stars necessary for the synthesis of carbon through the triple-α process [149].

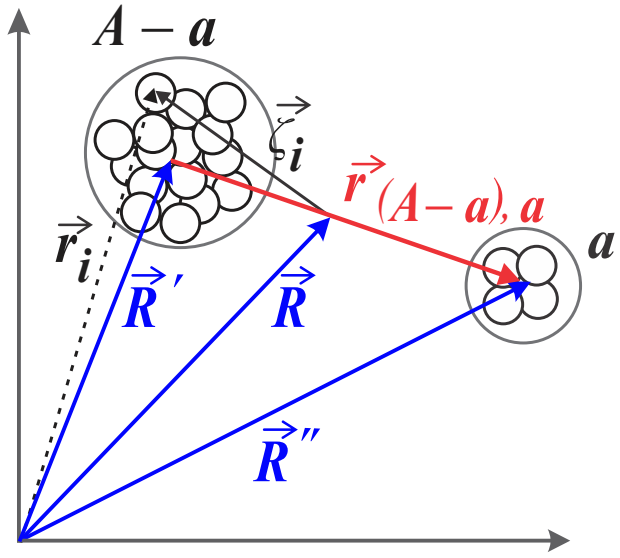

Figure 6.1. Representation of an A-nucleon system in terms of two clusters with $A-a$ and a nucleons. $\vec{r}$ are the particle coordinates in the laboratory frame; $\vec{R}'$ and $\vec{R}''$ are the center-of-mass coordinates of the individual clusters, $\vec{R}$ is the center-of-mass coordinate of the A-nucleon system; ζ_i are the relative coordinates with respect to $\vec{R}$. The relative separation of the clusters is $\vec{r}_{(A-a),a}$. Figure adapted from [131].

Various many-body methods built upon realistic internucleon interactions have been employed for describing clustering in nuclei. Such models include the generator coordinate method (GCM) [152], the Green's function Monte-Carlo (GFMC) [153], nuclear lattice EFT [147], the no-core shell model with resonating-group method (NCSM/RGM) [154,155], the no-core shell model with continuum (NCSMC) [156], and SA-NCSM [131]. In this chapter we present the first single-nucleon cluster wavefunction calculations from the SA-NCSM for ^{8}Be and a series of Li isotopes as well as the application of a previously established technique (see Ref. [131]) that uses symmetry-adapted wavefunctions to calculate α clustering in ^{8}Be. The *ab initio* single-nucleon cluster wavefunctions (also called spectroscopic overlaps) are a first step to description of low-energy nuclear reactions and can be used to construct *ab initio* nucleon optical potentials.

For a nucleus of A particles, the set of laboratory coordinates are given by $\vec{r}_1, ..., \vec{r}_A$. In the case of two clusters one with a particles and the other with $A-a$ separated from each other by $\vec{r}_{A-a,a}$, the coordinates can be divided into two distinct sets of laboratory coordinates, $\vec{r}_1, ..., \vec{r}_a$ and $\vec{r}_{a+1}, ..., \vec{r}_A$ (see Fig. 6.1). The centers of mass of the nucleus ($\vec{R}$) and the two clusters ($\vec{R}'$ and $\vec{R}''$), along with the distance between the clusters ($\vec{r}_{A-a,a}$) are given as

$$\vec{R} = \frac{1}{A}\sum_{i=1}^{A}\vec{r}_i = \frac{(A-a)\vec{R}' + a\vec{R}''}{A}, \tag{6.1}$$

$$\vec{R}' = \frac{1}{A-a}\sum_{i=a+1}^{A}\vec{r}_i, \quad \vec{R}'' = \frac{1}{a}\sum_{i=1}^{a}\vec{r}_i, \tag{6.2}$$

$$\vec{r}_{A-a,a} = \vec{R}'' - \vec{R}'. \tag{6.3}$$

To describe the two-cluster system in terms of translationally invariant quantities we use relative coordinates with respect to the center-of-mass (c.m.) of the A-particle system given

as

$$\vec{\zeta}_i = \vec{r}_i - \vec{R}. \tag{6.4}$$

Note that there are only $A-1$ independent relative coordinates since $\sum_{i=1}^{A} \vec{\zeta}_i = 0$. The two-cluster system is then fully described by

$$\vec{\zeta} = \{\vec{\zeta}_1, ..., \vec{\zeta}_a, \vec{\zeta}_{a+1}, ..., \vec{\zeta}_{A-1}\}. \tag{6.5}$$

The cluster wavefunction is considered in two regions, the internal range, where the wavefunction is driven by the internucleon interactions, and the external range where the only interaction between the clusters is assumed to be due to the Coulomb force. The internal wavefunction can be calculated using many-body methods such as the SA-NCSM. For bound states the exterior wavefunction for clusters with relative angular momentum l is given by an asymptotically decaying Whittaker function [131, 149, 157]:

$$W_{-\eta,l+\frac{1}{2}}(2kr) \xrightarrow[r\to\infty]{} (2kr)^{-\eta} e^{-kr}, \tag{6.6}$$

with $k = \sqrt{2\mu B}/\hbar$, where B is the cluster separation energy and μ is the reduced mass of the two clusters, and $\eta = Z_a Z_{A-a} \mu e^2/\hbar^2 k$ is the Sommerfeld parameter. The amplitude of the exterior wavefunction at large distances r is called asymptotic normalization coefficient (ANC), hence the exterior bound state wavefunction is given as

$$\phi^{J,\,\mathrm{ext}}_{\nu lj}(r) \approx C^J_{\nu lj} \frac{W_{-\eta,l+\frac{1}{2}}(2kr)}{r}. \tag{6.7}$$

Here, $C^J_{\nu lj}$ corresponds to the ANC, where ν represents all quantum numbers needed to fully characterize the respective states of the two clusters, and contains their parities and total angular momenta. The relative orbital momentum l (the partial wave) is coupled with the total angular momentum of the a cluster to j. Subsequently, j is coupled with the total angular momentum of the $A-a$ cluster to a good total angular momentum J of the system.

Asymtotically, for large r the interior cluster wavefunction (or the spectroscopic overlap) $u^J_{\nu lj}(r)$ approaches the exterior wavefunction in Eq. (6.7). To extract the ANCs, we use direct matching of the interior wavefunction to the exterior one similar to Ref. [153]. The radius where the two wavefunctions are matched is called channel radius, r_c. Other matching methods are described in Refs. [131, 158].

In terms of Slater determinants the spectroscopic overlap for a single-nucleon projectile ($a = 1$) has the form [159]:

$$\begin{aligned} u^{A\alpha JT}_{A-1\alpha_1 I_1 T_1;(1/2)(1/2)l,j}(r) &= \sum_n R_{nl}(r) \frac{1}{\langle nl00l|00nll\rangle_{1/A-1}} \frac{1}{\Pi_J \Pi_T} \\ &\quad \times {}_{\rm L}\langle A\alpha JT \| |a^\dagger_{nlj}| \| A-1\alpha_1 I_1 T_1\rangle_{\rm L}, \end{aligned} \tag{6.8}$$

with A being the mass of the composite nucleus, $I_1(T_1)$ and J (T) are the total angular momenta (total isospins) of the target and composite nuclei, respectively. The coupling of the orbital momentum l of the nucleon with its spin (1/2) yields j, while the coupling of isospin T_1 to the nucleon isospin (1/2) gives T. The $R_{nl}(r)$ is the radial wavefunction, with HO principal quantum number n, and $\Pi_s = \sqrt{2s+1}$. The labels α_1 and α stand for the additional quantum numbers needed to characterize the eigenstates. The matrix element is reduced with respect to the angular momentum and isospin. The bra and ket eigenstates correspond to the lab-frame wavefunctions of the composite and target nuclei, respectively, calculated from the many-body theory. In the SA-NCSM the reduced matrix element is calculated using the eigenvectors of the initial and final many-body states in the SU(3)-coupled basis. The creation operator is expressed as an SU(3) tensor $a^\dagger_{(\eta\,0)lj}$, where $\eta = 2n + l$ (see Chapter 2). The HO bracket that is used to remove the spurious center of mass motion of the A system is given by

$$\langle nl00l|00nll\rangle_{a/A-a} = (-1)^l \Big(\frac{A-a}{A}\Big)^{(2n+l)/2}. \tag{6.9}$$

The norm of the spectroscopic overlap,

$$S^{A\alpha JT}_{A-1\alpha_1 I_1 T_1;(1/2)(1/2)l,j} = \int |r u^{A\alpha JT}_{A-1\alpha_1 I_1 T_1;(1/2)(1/2)l,j}(r)|^2 dr \tag{6.10}$$

is called the spectroscopic factor (SF).

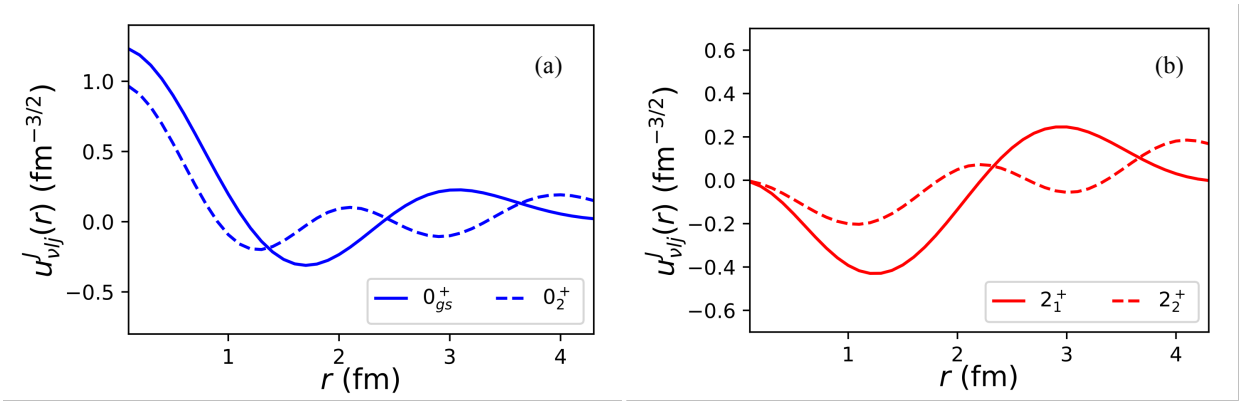

Figure 6.2. Interior cluster wavefunctions $\langle {}^8\mathrm{Be}|\alpha+\alpha\rangle$ for the lowest two (a) 0^+ states with $l=0$, $j=0$, and (b) 2^+ states with $l=2$, $j=2$ in ^{8}Be. The wavefunctions were calculated with NNLO$_{\mathrm{opt}}$interaction in $N_{\max}$=16 model space and $\hbar\Omega$=15 MeV.

To study the cluster structure of the lowest two 0^+ and 2^+ states of ^{8}Be, we calculate the overlaps of the many-body wavefunctions with the $\alpha+\alpha$ and $^7\mathrm{Li}+p$ systems, and present the interior $\alpha+\alpha$ cluster wave function (Fig. 6.2). The experimental threshold of these systems with respect to the ^{8}Be ground state are -0.092 MeV for $\alpha+\alpha$ and 17.255 MeV for $^7\mathrm{Li}+p$, thus the lowest two 2^+ states are below the proton separation energy. For the calculations of $\alpha+\alpha$ cluster wavefunctions (Fig. 6.2), we follow the procedure in Ref. [131] using the ^{8}Be 0^+ and 2^+ states and ^{4}He ground state calculated in Sp$(3,\mathbb{R})$ basis. To compose a $J=2$ cluster state with two α's in their ground state (0^+), we consider the relative orbital momentum $l=2$. Both 2^+ states have distinct peaks at longer distances suggesting alpha clustering, whereas the 2^+_2 state is more spatially expanded.

Calculations of the single-nucleon overlaps $\langle {}^8\mathrm{Be}|{}^7\mathrm{Li}+p\rangle$ follow the formalism outlined above (Fig. 6.3). In this case the states in ^{8}Be below 17.255 MeV excitation energy are bound with respect to the $^7\mathrm{Li}+p$ threshold. Here, the p-wave is described by the ^{7}Li ground

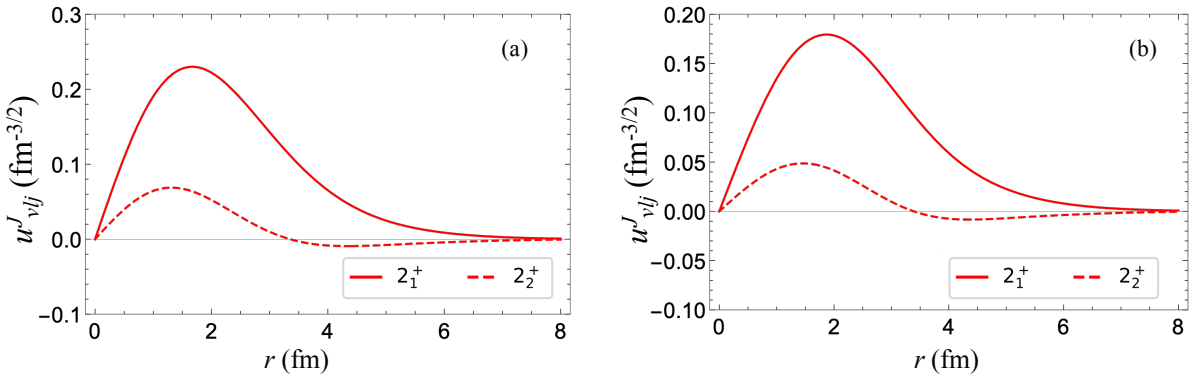

Figure 6.3. Interior cluster wavefunctions $\langle {}^8\mathrm{Be}|{}^7\mathrm{Li}+p\rangle$ for the lowest two 2^+ states in ^{8}Be for (a) $p_{3/2}$ and (b) $p_{1/2}$ partial waves. The wavefunctions were calculated with $\mathrm{NNLO_{opt}}$ interaction in $N_{\max}$=10 model space and $\hbar\Omega$=15 MeV.

state, which couples with the proton orbital momentum and spin to a final $J = 2$ in ^{8}Be. We find a large overlap between the $^7\mathrm{Li} + p$ and the lowest 2^+ state, and a comparatively small but non-negligible overlap with the second 2^+ state.

6.2 Single-nucleon overlaps for Li isotopes

To further investigate the formalism for calculations of single-nucleon overlaps we study a series of Li+n systems that are important for astrophysical processes. In particular, the calculated abundances for ^{6}Li and ^{7}Li from the standard big bang nucleosynthesis deviate from the observations in metal-poor halo stars [160]. This deviation has motivated several experimental studies of $^6\mathrm{Li}(n,\gamma)^7\mathrm{Li}$ reaction [161, 162]. In addition, the inhomogeneous big bang models [163] predict relatively higher abundances of $A > 8$ nuclides than the standard big bang nucleosynthesis. In inhomogeneous models the reaction chains $^7\mathrm{Li}(n,\gamma)^8\mathrm{Li}(\alpha,n)^{11}\mathrm{B}$ are typically thought to be critical for producing heavier nuclei. However, it has been determined that $^7\mathrm{Li}(n,\gamma)^8\mathrm{Li}(n,\gamma)^9\mathrm{Li}(\alpha,n)^{12}\mathrm{B}$ may be even more vital [164] since the $^8\mathrm{Li}(n,\gamma)^9\mathrm{Li}$ process affects not only the reaction path to $A > 8$ nuclei but also the abundances of Li, Be, B, and C.

Here, we present calculations of single-nucleon overlaps $\langle {}^7\mathrm{Li}|{}^6\mathrm{Li}+n\rangle$, $\langle {}^8\mathrm{Li}|{}^7\mathrm{Li}+n\rangle$ and $\langle {}^9\mathrm{Li}|{}^8\mathrm{Li}+n\rangle$ between the ground states. We match the obtained overlaps to the exterior Whittaker function to calculate the ANCs and compare them to the experimentally deduced

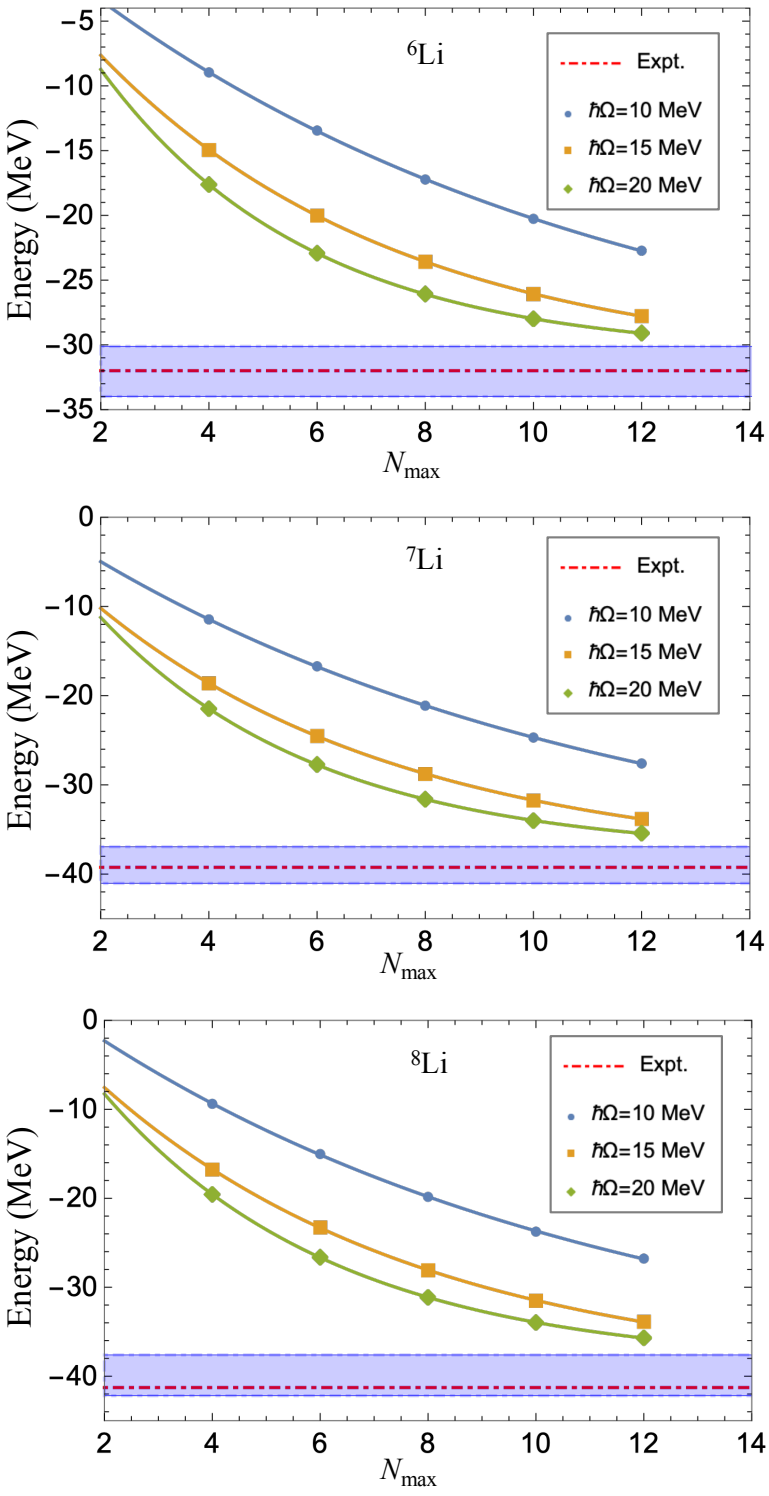

Figure 6.4. Calculations of ^{6,7,8}Li ground state energies vs. $N_{\max}$ using NNLO$_{\text{opt}}$ interaction with $\hbar\Omega$=10, 15 and 20 MeV, and compared to experiment (Expt.). The blue band indicates the range of energies from extrapolations.

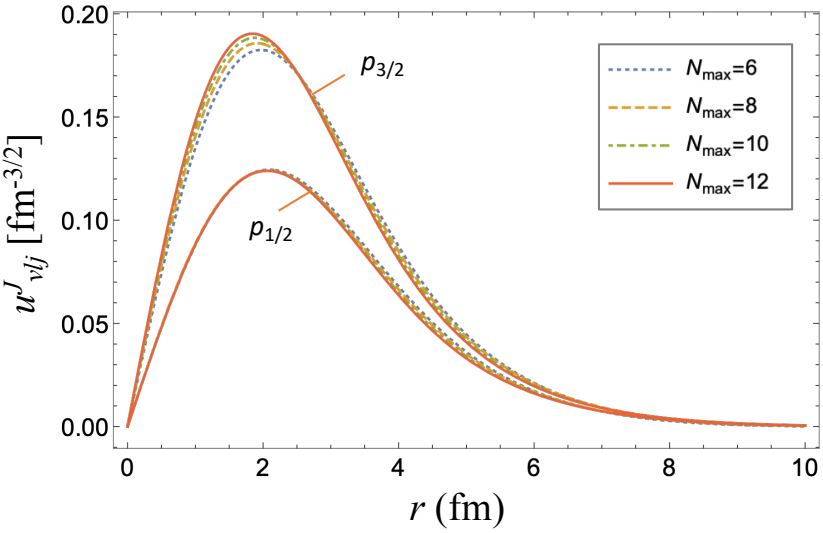

Figure 6.5. Single-nucleon overlaps $\langle {}^7\mathrm{Li}|{}^6\mathrm{Li}+n\rangle$ in $N_{\max}$=6 to 12 with $\hbar\Omega$=10 MeV for partial waves $p_{1/2}$ and $p_{3/2}$ vs. the separation between ^{8}Li and the neutron.

values. All of the calculations in this section are done using the NNLO$_{\mathrm{opt}}$ chiral potential [32].

To obtain the eigenvectors of the Li ground states needed for calculations of spectroscopic overlaps, we solve the Schrödinger equation with realistic interactions. The eigenvalues from the solutions correspond to the ground state energies of the Li isotopes (Fig. 6.4). Since the calculations are done in a finite model space, the eigenvalues converge to the infinite-space result from above. We perform calculations using HO parameter values $\hbar\Omega$=10, 15 and 20 MeV and for each of the $\hbar\Omega$ extrapolate to the infinite-space using a three-parameter exponential formula similar to Ref. [73]:

$$E(N_{\max}) = E(\infty) + a\exp(-cN_{\max}), \tag{6.11}$$

where $E(\infty)$ is the energy at infinite model space. The error bars indicate uncertainty due to $\hbar\Omega$ variance and the nonlinear fitting. The extrapolated values are in a good agreement with the experiment.

The ground states of Li isotopes that differ in mass by one nucleon have opposite parities. Since the parity of the nucleon is given by $(-1)^l$, l must be odd to preserve the parity. In

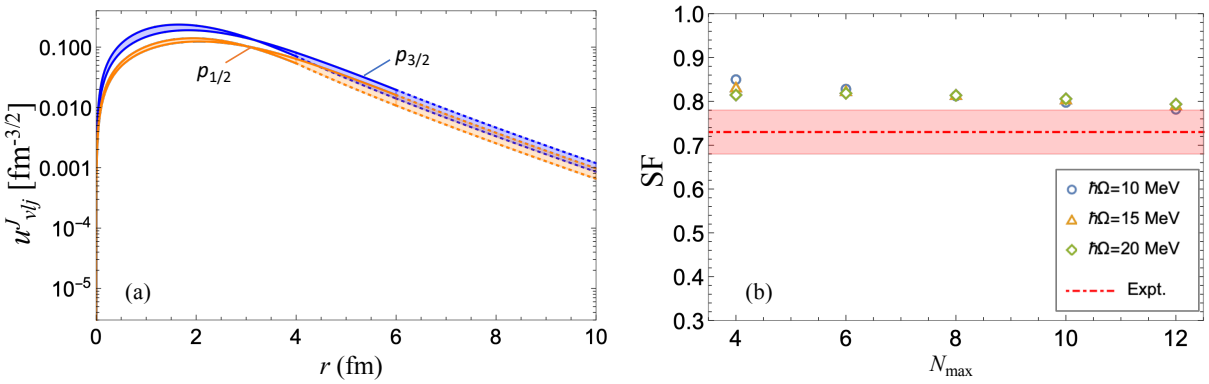

Figure 6.6. (a) Single-nucleon overlaps of the ^{7}Li ground state with the ^{6}Li+n in $N_{\max}$=12 for partial waves $p_{1/2}$ and $p_{3/2}$ vs. the separation between ^{8}Li and the neutron. The dotted lines correspond to the exterior Whittaker function. The shaded bands indicate the uncertainty due to the $\hbar\Omega$ variance from 10 to 20 MeV. (b) Calculated SFs with the increasing model space $N_{\max}$ and compared to the experimentally deduced value (denoted as "Expt.") from Ref. [162]. The red band indicates the experimental uncertainty.

addition, as it was shown in Ref. [158] and observed in our calculations, the $l = 3$ overlaps are about two orders of magnitude smaller than the $l = 1$ overlaps. Hence, we limit our analysis to only $l = 1$, $p_{1/2}$ ($j = 1 - 1/2$) and $p_{3/2}$ ($j = 1 + 1/2$) partial waves. For these two values of l we explore the dependence of the $\langle^7\mathrm{Li}|^6\mathrm{Li} + n\rangle$ overlaps on the model space size for a fixed $\hbar\Omega$ (Fig. 6.5). With increasing $N_{\max}$, the changes between successive curves become smaller indicating convergence of the overlaps. Similar dependence is observed for $\langle^8\mathrm{Li}|^7\mathrm{Li} + n\rangle$ and $\langle^9\mathrm{Li}|^8\mathrm{Li} + n\rangle$.

It should be noted that the short-range part of the overlaps has a weak dependence on the $N_{\max}$, while the long-range part is more sensitive to it. To ensure accurate description of the long range part, we match the tails of the overlaps to the exterior wavefunctions (dotted lines in the figures). Since the overlaps decay quickly at larger radii, it is more informative to present them in a logarithmic scale. Furthermore, the overlaps are represented as bands of values due to the variance of the HO parameter $\hbar\Omega$ from 10 to 20 MeV, typical for nuclei in this mass range (Fig. 6.6a). We integrate the overlaps to obtain the SFs for each of the partial waves, with the total SF given by the sum of all. For $\langle^7\mathrm{Li}|^6\mathrm{Li} + n\rangle$ the calculated SFs converge towards the experimentally deduced value from Ref. [162] as the model space

increases (Fig. 6.6b).

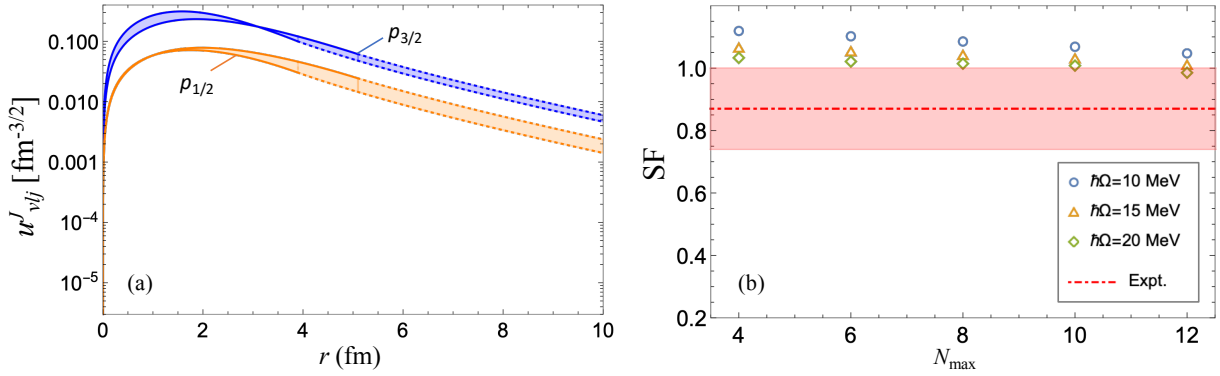

Figure 6.7. Same as Fig. 6.6 but for $^7\mathrm{Li} + n$. The experimentally deduced SF is from Ref. [165].

A similar picture is seen in $\langle {}^8\mathrm{Li}|{}^7\mathrm{Li} + n\rangle$ and $\langle {}^9\mathrm{Li}|{}^8\mathrm{Li} + n\rangle$ overlaps (Figs. 6.7 and 6.8). In $\langle {}^8\mathrm{Li}|{}^7\mathrm{Li} + n\rangle$ the spread of values due to the $\hbar\Omega$ variance is small in the short-range part of the wavefunction but becomes more apparent at larger radii. This shows that the description of the long-range part of the wavefunction is sensitive to the $\hbar\Omega$ values for a given $N_{\max}$. The larger spread in the $p_{1/2}$ overlap of $\langle {}^9\mathrm{Li}|{}^8\mathrm{Li} + n\rangle$ is due to its smaller values (by an order of magnitude) compared to the $p_{3/2}$ (Fig. 6.8a). For both $\langle {}^8\mathrm{Li}|{}^7\mathrm{Li} + n\rangle$ and $\langle {}^9\mathrm{Li}|{}^8\mathrm{Li} + n\rangle$ the calculations of SFs with all HO frequencies are converging to the uncertainty range of the experimentally deduced results (Figs. 6.7b and 6.8b). We should note that the SFs, representing the area under the overlaps curves, depend mainly on the short-range part of overlaps, thus they are mostly unaffected by the matching to the exterior wavefunction.

Obtaining ANCs directly from matching the overlaps to Eq. (6.7) can be challenging for the many-body methods that use HO basis, since the asymptotics at large radii is affected by the model space cutoff. Ideally, the ANC should become independent of the matching radius after a certain point. However, this does not happen as the tails of the overlaps drop quickly beyond the HO cutoff. In addition, the extractions of ANCs from Eq. (6.7) requires the separation energy B. To be fully consistent in determining the ANCs from overlaps, one should use theoretically calculated separation energies B_{th}. Nevertheless, in most models

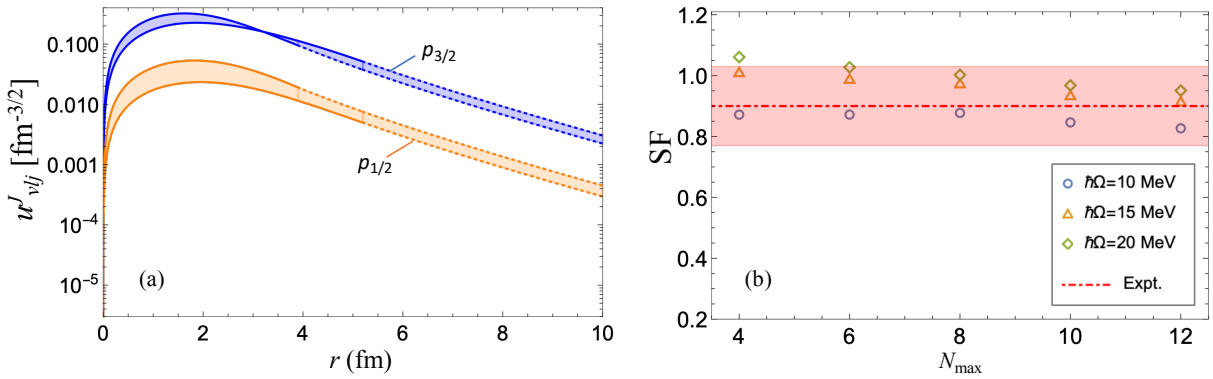

Figure 6.8. Same as Fig. 6.6 but for $^8\mathrm{Li} + n$. The experimentally deduced SF is from Ref. [166].

the experimental value B_{exp} is used to make the ANCs practical for reaction calculations, since even small deviations of B_{th} from B_{exp} can affect the ANCs [158].

As mentioned above, we calculate the ANCs by directly matching the spectroscopic overlap to the exterior Whittaker function and choosing an r_c that maximizes the ANC. We use B_{exp} in our calculations. To report a parameter-free ANCs, we use the Shanks transformation [69, 167] on the $N_{\max}$=8, 10 and 12 calculations for $\hbar\Omega$=15 and 20 MeV that are close to convergence. For the Li isotopes discussed here the fastest convergence is observed for $\hbar\Omega$=15 MeV, which appears to be the optimal $\hbar\Omega$ value, that is, where the convergence of results is achieved at comparatively smaller model spaces, while other $\hbar\Omega$ values demand larger $N_{\max}$ to produce the same estimate. In particular, the ANC for $\langle {}^7\mathrm{Li}|{}^6\mathrm{Li} + n\rangle$ flattens around r_c = 4.6 - 5 fm (Fig. 6.9b), whereas for the $\hbar\Omega$=10 and 20 MeV the results are not yet close to convergence (Fig. 6.9a and c). The total ANC for the $p_{1/2}$ and $p_{3/2}$ partial waves is calculated by $C_1 = \sqrt{C^2_{p1/2} + C^2_{p3/2}}$. Our prediction based on the extrapolated results of $\hbar\Omega$=15 MeV and 20 MeV at channel radii with maximum ANC is 2.4 ± 0.2, which is within the experimentally deduced range of $1.26 - 2.82$ fm$^{-1/2}$ [168].

The experimentally inferred ANCs for the $\langle {}^8\mathrm{Li}|{}^7\mathrm{Li} + n\rangle$ wavefunction are available for $p_{1/2}$ and $p_{3/2}$ partial waves separately. Thus, we compare the extrapolations of the calculated ANCs for each of the partial waves separately. For this system, both $\hbar\Omega$=15 and 20 MeV yield

extrapolated results almost independent of the channel radius (Fig. 6.10). The predictions from calculations are 0.24 ± 0.04 fm$^{-1/2}$ for $p_{1/2}$ and 0.72 ± 0.07 fm$^{-1/2}$ for $p_{3/2}$, which agree with the "measured" values of 0.22 ± 0.03 fm$^{-1/2}$ and 0.62 ± 0.03 fm$^{-1/2}$, respectively [169].

As mentioned above, the $\langle {}^9\mathrm{Li} | {}^8\mathrm{Li} + n \rangle$ overlap is dominated by the $p_{3/2}$ partial wave. This results in total ANC being almost indistinguishable from the $p_{3/2}$ ANC (Fig. 6.11). Again, the extrapolations of ANCs for $\hbar\Omega$=15 and 20 MeV are very close to each other and virtually do not depend on r_c. From these extrapolations, we predict a total ANC of 1.24 ± 0.04 fm$^{-1/2}$ in an excellent agreement with the experimentally extracted value of 1.15 ± 0.14 fm$^{-1/2}$ [170].

6.3 Toward constructing optical potentials from *ab initio* wave functions

Nuclear reactions are indispensable for studying atomic nuclei. Many reactions relevant to astrophysical processes occur at relatively low energies $E < 1$ MeV [149]. Nevertheless, these reactions are generally measured in laboratories indirectly with beams at energies $\geqslant 5$ MeV per nucleon. To extract reaction observables for low energies, the measured data is often used to obtain effective interactions between the nuclear clusters, commonly known as optical potentials [171]. In this case, the many-body description of nuclei is reduced to a few-body one, with only the relevant degrees of freedom maintained. These potentials can then be utilized to calculate reaction cross-sections for a wide range of energies.

The application of optical potentials becomes unreliable in exotic regions of the nuclear chart since the experimental data is scarce. For these regions, it is important to connect the optical potentials to the underlying many-body theory [172]. The cluster wavefunctions calculated from *ab initio* methods can help in this endeavor. The single-particle overlaps are the solutions of the Schrödinger equation with one-nucleon optical potentials. Hence, they can be fitted to obtain parameters of optical potentials. Such fits have been performed for a series of light nuclei through a χ^2 fitting for overlaps calculated from the GFMC [153]. Yet, the work has focused on obtaining the ANCs from the fitted potentials and did not provide uncertainties on the parameters. The accurate quantification of uncertainties is critical in reaction models. In the recent years, the Bayesian methods have become increasingly more

popular for uncertainty quantification in nuclear physics [172–177]. As a further application of the overlaps calculated from the SA-NCSM, they are be parameterized using Bayesian methods to obtain optical potentials based on *ab initio* calculations (work in progress). The first such fits have shown promising results for the $\langle {}^7\mathrm{Li}|{}^6\mathrm{Li} + n\rangle$ overlaps [178] (work in progress) opening new opportunities for the *ab initio* reaction theory.

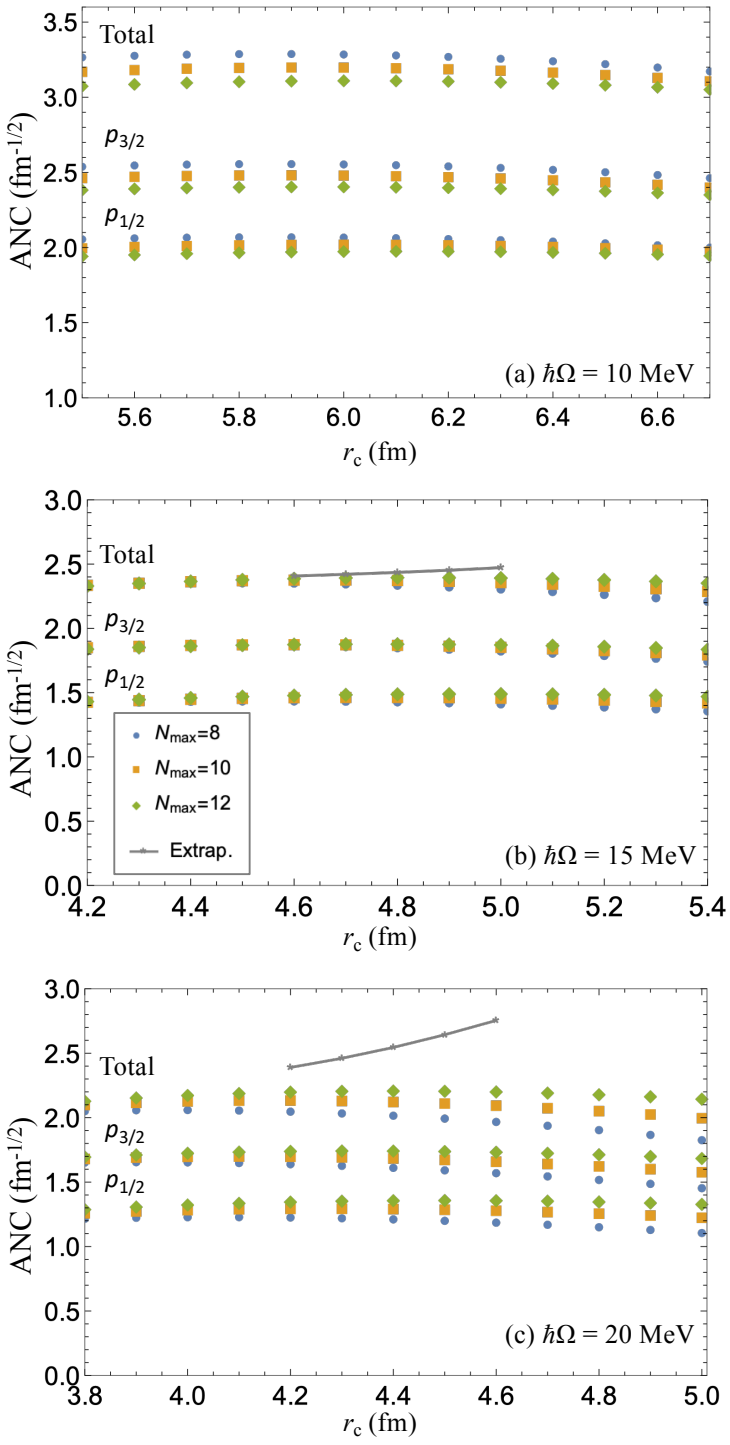

Figure 6.9. ANCs for the $\langle {}^7\mathrm{Li}|{}^6\mathrm{Li}+n\rangle$ as a functions of the channel radius r_c with (a) $\hbar\Omega$=10 MeV, (b) $\hbar\Omega$=15 MeV and (c) $\hbar\Omega$=20 MeV. The label "Total" denotes $\sqrt{\sum C_{lj}^2}$ for the $p_{1/2}$ and $p_{3/2}$ partial waves. The connected gray points show the extrapolated results (denoted as "Extrap."). The experimentally deduced range for the total ANC is 1.26–2.82 fm$^{-1/2}$ [168].

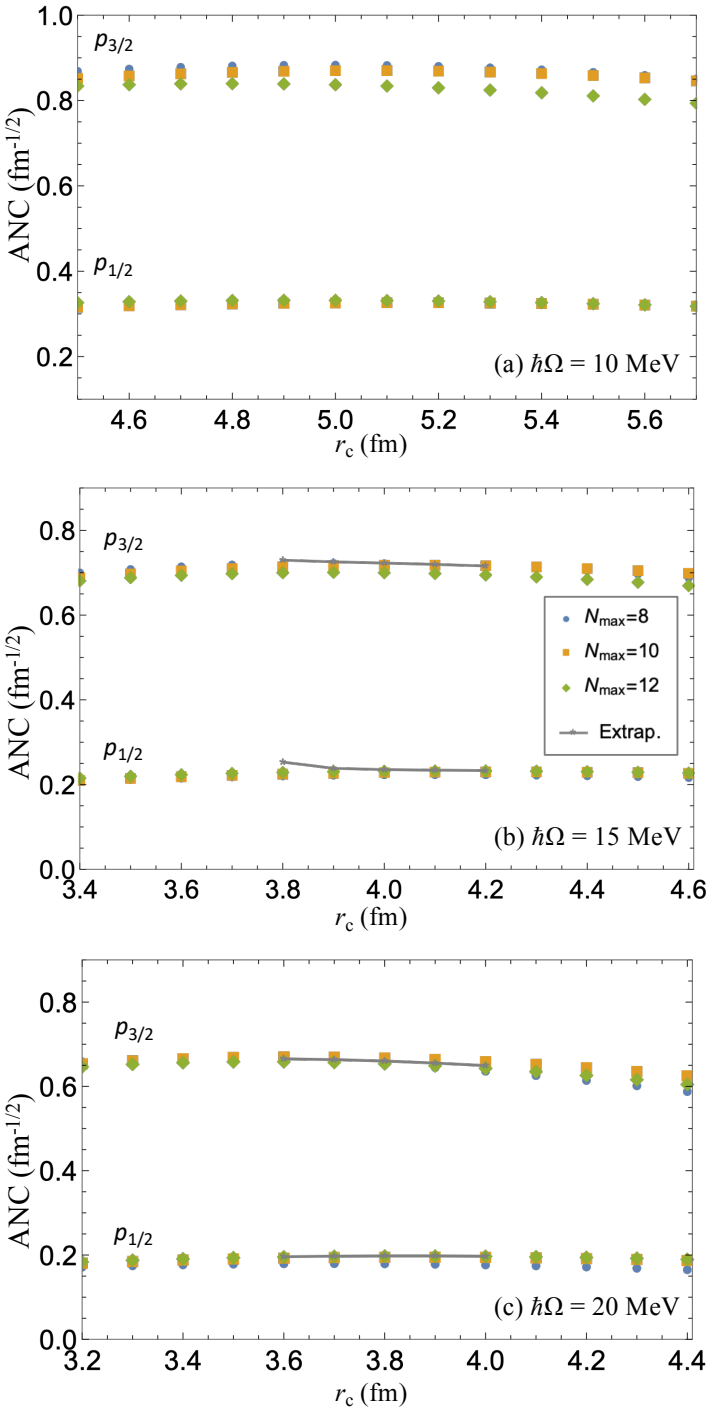

Figure 6.10. ANCs for the $\langle {}^8\mathrm{Li}|{}^7\mathrm{Li}+n\rangle$ as a functions of the channel radius r_c in $N_{\max}$=8 to 12 with (a) $\hbar\Omega$=10 MeV, (b) $\hbar\Omega$=15 MeV and (c) $\hbar\Omega$=20 MeV. The connected gray points show the extrapolated results (denoted as "Extrap."). The experimentally deduced ANC for $p_{1/2}$ is 0.22 ± 0.3 fm$^{-1/2}$ and for $p_{3/2}$ is 0.62 ± 0.3 fm$^{-1/2}$ [169].

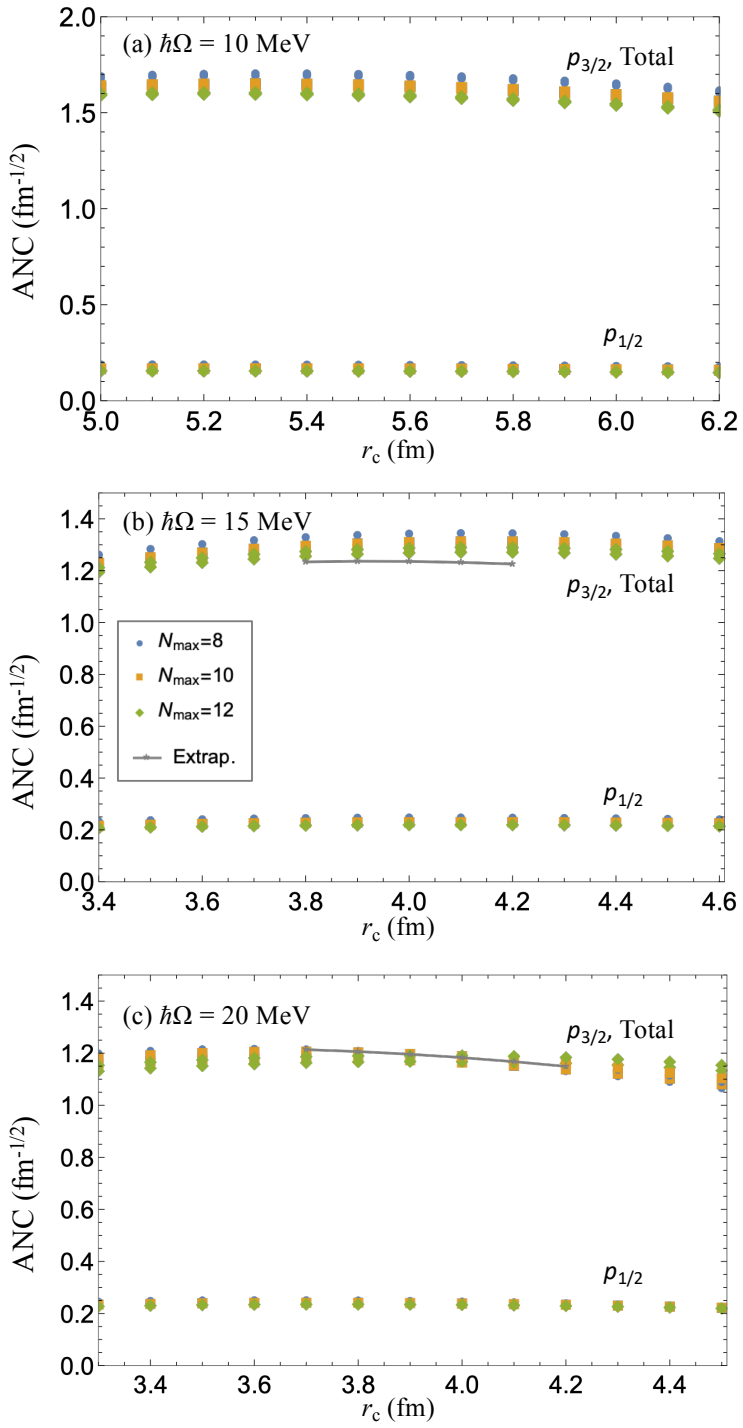

Figure 6.11. ANCs for the $\langle {}^9\mathrm{Li}|{}^8\mathrm{Li}+n\rangle$ as a functions of the channel radius r_c in $N_{\max}$=8 to 12 with (a) $\hbar\Omega$=10 MeV, (b) $\hbar\Omega$=15 MeV and (c) $\hbar\Omega$=20 MeV. The label "Total" denotes $\sqrt{\sum C_{lj}^2}$ for the $p_{1/2}$ and $p_{3/2}$ partial waves. The connected gray points show the extrapolated results (denoted as "Extrap."). The experimentally deduced total ANC is 1.15 ± 0.14 [170].

7 Conclusions

In this work we calculated electromagnetic and weak transitions in nuclei from first principles. The results are valuable for helping probe physics beyond the Standard Model. In addition, we showed the importance of clustering in describing the challenging resonance states in nuclei, and advanced a method to calculate single-nucleon overlaps that can be used to obtain optical potentials for nucleon projectiles.

In particular, to better understand the building blocks of *ab initio* methods, we studied the underlying internucleon interactions from the symmetry-adapted prospective. Realistic NN interactions expressed in an SU(3) basis show a clear dominance of only a small fraction of all terms. We performed *ab initio* calculations of several observables in ^{12}C using interactions that were selected down to the most significant terms and compared them to the calculations with the initial interactions. We found that in sufficiently large model spaces even the interactions with less than half of the terms produce almost the same results as the initial interaction for ^{12}C. By analyzing the most dominant terms of various realistic interactions, we found that they can be linked to well-known nuclear forces. In particular, an inspection of these terms allowed us to link them to the widely used HO potential, $Q \cdot Q$, pairing, spin-orbit and tensor forces. Moreover, we saw that after renormalization the NN interactions, regardless of their type, have mainly the same dominant terms with similar strengths, indicating that the renormalization techniques strengthen the same dominant terms in all the interactions.

We developed a method to calculate neutrinoless double-beta decay matrix elements using *ab initio* many-body wavefunctions. The method was validated on ^{6}He $\rightarrow^{6}$Be and ^{22}O $\rightarrow^{22}$Ne transitions and subsequently applied to the lightest candidate of the neutrinoless double-beta decay ^{48}Ca. To help modern experiments deduce whether neutrino is its own antiparticle, we set a lower limit on the $0\nu\beta\beta$ nuclear matrix element for ^{48}Ca using the chiral NNLO$_{\rm opt}$ potential. The result is below the predictions of most phenomenological approaches and it is in agreement with other recent *ab initio* studies, but utilizes the exact

(non-renormalized) operator.

The *ab initio* SA-NCSM was used to determine the size of the recoil-order form factors in the β decay of ^{8}Li. It showed that states of the $\alpha+\alpha$ system not included in the evaluated ^{8}Be energy spectrum have an important effect on all $j_{2,3}/A^2c_0$, b/Ac_0 and d/Ac_0 terms, and can explain the $M_{\rm GT}$ discrepancy in the $A = 8$ systems. The outcomes reduce – by over 50% – the uncertainty on these recoil-order corrections. These results help improve the sensitivity of high-precision β-decay experiments that probe the V−A structure of the weak interaction [116]. Furthermore, our predicted b/Ac_0 and d/Ac_0 values are important for other investigations of the Standard Model symmetries, such as the CVC hypothesis and the existence of second-class currents.

In addition, we examined the ^{8}Be cluster substructures such as the single-nucleon and alpha cluster wavefunctions to gain a better understanding of the final states of the ^{8}Li beta decay. The method was then applied to a series of Li isotopes to calculate SFs and ANCs that were shown to be in good agreement with the experimentally deduced values. The single-nucleon cluster wavefunctions calculated from first principles were parameterized using Bayesian technique to obtain optical potentials for nucleon projectiles. This, in turn, opens new opportunities for calculating reaction observables from *ab initio* methods.

Appendix A NN Interaction Transformation into SU(3) Basis

In the standard second quantized form, a one- and two-body interaction Hamiltonian is given in terms of fermion creation $a^\dagger_{jm(1/2)\sigma}$ and annihilation $\tilde{a}_{j-m(1/2)-\sigma} = (-1)^{j-m+1/2-\sigma} a_{jm(1/2)\sigma}$ tensors, which create or annihilate a particle of type $\sigma = \pm 1/2$ (proton/neutron) in the HO basis.

In Eq. (A.1), V^Γ_{rstu} is the two-body antisymmetric matrix element in the JT-coupled scheme [$V^\Gamma_{rstu} = -(-)^{r+s-\Gamma} V^\Gamma_{srtu} = -(-)^{t+u-\Gamma} V^\Gamma_{rsut} = (-)^{r+s-t-u} V^\Gamma_{srut} = V^\Gamma_{turs}$]. For an isospin nonconserving two-body interaction of isospin rank $\mathcal{T}$, the coupling of fermion operators is as follows, $\{\{a^\dagger_r \times a^\dagger_s\}^{JT} \times \{a_t \times a_u\}^{JT}\}^{(0\mathcal{T})}$, with $V^{(\mathcal{T})JT}_{rstu}$ matrix elements.

$$
\begin{aligned}
V &= -\frac{1}{4} \sum_{rstu\Gamma} \sqrt{(1+\delta_{rs})(1+\delta_{tu})}\Pi_\Gamma V^\Gamma_{rstu} \{\{a^\dagger_r \times a^\dagger_s\}^\Gamma \times \{\tilde{a}_t \times \tilde{a}_u\}^\Gamma\}^{(\Gamma_0 M_{\Gamma_0})} \\
&= \sum_{\substack{(\chi^* \omega S)_{fi} \\ \rho_0 \omega_0 \kappa_0 S_0}} \frac{(-1)^{\omega_0 - \omega_f + \omega_i}}{\sqrt{(1+\delta_{\eta_r \eta_s})(1+\delta_{\eta_t \eta_u})}} \frac{1}{\Pi_{S_0}} \sqrt{\frac{\dim \omega_f}{\dim \omega_0}} V^{\rho_0 \omega_0 \kappa_0 S_0}_{(\chi \omega S)_{f,i} T} \times \\
&\quad \sum_{\rho'_0} \Phi_{\rho'_0 \rho_0}(\omega_0 \omega_i \omega_f) \{\{a^\dagger_{\eta_r} \times a^\dagger_{\eta_s}\}^{\omega_f S_f T} \times \{\tilde{a}_{\eta_t} \times \tilde{a}_{\eta_u}\}^{\omega_i S_i T}\}^{\rho'_0 \omega_0 \kappa_0 (L_0 = S_0 S_0) \Gamma_0 = 0 M_{\Gamma_0} = 0},
\end{aligned}
\tag{A.1}
$$

where dim ω is defined in Eq. (2.3) and the phase matrix $\Phi_{\rho'_0 \rho_0}(\omega_0 \omega_i \omega_i)$ accommodates the interchange between the coupling of ω_0 and ω_i to ω_f, so for SU(3) Clebsch-Gordan coefficients we have [179]

$$
\langle \omega_0 \kappa_0 L_0 M_0; \omega_i \kappa_i L_i M_i | \, \omega_f \kappa_f L_f M_f \rangle_{\rho_0} = \sum_{\rho'_0} \Phi_{\rho_0 \rho'_0}(\omega_0 \omega_i \omega_f) \langle \omega_i \kappa_i L_i M_i; \omega_0 \kappa_0 L_0 M_0 | \, \omega_f \kappa_f L_f M_f \rangle_{\rho'_0}.
\tag{A.2}
$$

For the special case when $\rho = 1$, that is, where the SU(3) coupling $\{\omega_i \times \omega_0\} \to \omega_f$ is unique, the phase matrix reduces to a simple phase factor $(-1)^{(\lambda_0+\mu_0)+(\lambda_i+\mu_i)-(\lambda_f+\mu_f)}$. Finally, the interaction reduced matrix elements in a $\mathrm{SU(3)} \times \mathrm{SU(2)}_S \times \mathrm{SU(2)}_T$-coupled HO basis are

given as,

$$
\begin{aligned}
V^{\rho_0\omega_0\kappa_0 S_0}_{(\chi\omega S)_{fi};T} &= (-)^{S_f+S_0}\Pi_{TS_0}\frac{\dim\omega_0}{\dim\omega_f}\sum_{J(\kappa L)_{if}}(-)^{L_i+J}\Pi_J^2\Pi_{L_f} \\
&\times \begin{Bmatrix} L_f & S_f & J \\ S_i & L_i & S_0 \end{Bmatrix}\langle\omega_i\kappa_i L_i;\omega_0\kappa_0 L_0\|\omega_f\kappa_f L_f\rangle_{\rho_0}V^{\Gamma}_{(\chi\omega\kappa LS)_{fi}} \\
&= (-)^{S_f+S_0}\Pi_{TS_0}\frac{\dim\omega_0}{\dim\omega_f}\sum_{J(\kappa L)_{if}}(-)^{L_i+J}\Pi_J^2\Pi_{L_f} \\
&\times \begin{Bmatrix} L_f & S_f & J \\ S_i & L_i & S_0 \end{Bmatrix}\langle\omega_i\kappa_i L_i;\omega_0\kappa_0 L_0\|\omega_f\kappa_f L_f\rangle_{\rho_0}\Pi_{L_iL_fS_iS_f} \\
&\times \sum_{\substack{l_rl_sl_tl_u \\ j_rj_sj_tj_u}}\sqrt{\frac{(1+\delta_{rs})(1+\delta_{tu})}{(1+\delta_{\eta_r\eta_s})(1+\delta_{\eta_t\eta_u})}}\Pi_{j_rj_sj_tj_u}\langle(\eta_r\,0)l_r;(\eta_s\,0)l_s\|(\omega\kappa L)_f\rangle \\
&\quad\times\langle(\eta_t\,0)l_t;(\eta_u\,0)l_u\|(\omega\kappa L)_i\rangle\begin{Bmatrix} l_r & \frac{1}{2} & j_r \\ l_s & \frac{1}{2} & j_s \\ L_f & S_f & J \end{Bmatrix}\begin{Bmatrix} l_t & \frac{1}{2} & j_t \\ l_u & \frac{1}{2} & j_u \\ L_i & S_i & J \end{Bmatrix}V^{\Gamma}_{rstu}, \qquad \text{(A.3)}
\end{aligned}
$$

where $V^{\Gamma}_{(\chi\omega\kappa LS)_{fi}}$ is a two-body interaction in a SU(3)-JT-coupled scheme; as mentioned above $\langle;\|\rangle$ are reduced SU(3) Clebsch-Gordan coefficients [41, 42], and we use SU(2) Wigner 6-j and 9-j symbols.

Appendix B Beta Decay Matrix Elements

B.1 β decay Transition Rates

The weaker interaction between nucleons and electron-neutrino field allows to use perturbation theory in the first Born approximation. Hence the transition rate for β-decay can be given with Fermi's golden rule,

$$W = \frac{2\pi}{\hbar} |\langle \phi_f | H' | \phi_i \rangle|^2 \rho(E_f), \tag{B.1}$$

where ϕ_i and ϕ_f are the initial and final states respectively, and ρ is the density of the final states. The initial state simply involves the parent nucleus and can be considered stationary, $|\phi_i\rangle = |J_i M_i; T_i T_{z,i}, \zeta_i\rangle$, where ζ_i accounts for additional quantum numbers.

The final wavefunction contains states of three particles, a charged lepton, a neutral lepton and the daughter nucleus. Since the neutrino does not interact with other particles, its wavefunction can be approximated with plane waves, $\psi_\nu(r) = (1/\sqrt{V}) \exp(i\mathbf{k}_\nu \cdot \mathbf{r})$, where $1/\sqrt{V}$ is the renormalization constant and k_ν is the wavenumber of the neutrino. Moreover, if we neglect for the time being the interaction between the electron (positron) and the Coulomb filed of the nucleus, then the wavefunction of the charged lepton can also be expressed by plane waves $\psi_e(r) = (1/\sqrt{V}) \exp(i\mathbf{k_e} \cdot \mathbf{r})$. Typically, for β-decays the energy of the emitting leptons does not exceed several MeVs, so $|\mathbf{k_e} + \mathbf{k}_\nu| R << 1$, with R being the radius of the nucleus, therefore, the exponents can be expanded,

$$e^{i(\mathbf{k_e}+\mathbf{k}_\nu)\cdot\mathbf{r}} = 1 + i(\mathbf{k_e} + \mathbf{k}_\nu) \cdot \mathbf{r} - \frac{1}{2}[(\mathbf{k_e} + \mathbf{k}_\nu) \cdot \mathbf{r}]^2 + ...$$

In the first approximation we only need to retain the first term of the expansion. The probability of a β-decay in this approximation corresponds to the so called *allowed* β-decay. Inclusion of higher order terms when the first term alone gives zero, corresponds to *forbidden*

decays. The wavefunction of the final state for allowed decays will be

$$|\phi_f\rangle = \frac{1}{V} |J_f M_f; T_f T_{z,f}, \zeta_f\rangle \,.$$

Using the forms of Fermi and Gamow-Teller operators, the transition matrix element in Eq. (B.1) becomes

$$\begin{aligned} \langle \phi_f | \, H' \, | \phi_i \rangle \approx \frac{1}{V} \sum_{M_f} \big[C_V \, \langle J_f M_f; T_f T_{z,f}, \zeta_f | \sum_{j=1}^{A} \tau_j^{\pm} \, | J_i M_i; T_i T_{z,i}, \zeta_i \rangle \\ + C_A \sum_{\mu} \langle J_f M_f; T_f T_{z,f}, \zeta_f | \sum_{j=1}^{A} \sigma_{\mu,j} \tau_j^{\pm} \, | J_i M_i; T_i T_{z,i}, \zeta_i \rangle \, \big], \end{aligned} \tag{B.2}$$

here the summation over M_f takes care of the requirement to include all the possible nuclear final states.

To find the transition rate given in Eq. (B.1) we also need to determine the density of final states, $\rho(E_f) = dn/dE_f$. Since the mass of the daughter nucleus is much larger than the masses of emitted leptons, the recoil energy will be negligibly small compared to the kinetic energies of other two particles. As we mentioned, the neutrino does not interact with the other members, so it can be regarded as a free particle. Hence, the number of states of a neutrino with momentum p_ν is given by

$$dn_\nu = \frac{V}{2\pi^2 \hbar^3} p_\nu^2 dp_\nu,$$

where V is the same volume as in the three-dimensional plane wave renormalization. The relation between the momentum of the neutrino and its energy is found from $E_\nu^2 = m_\nu^2 c^4 + p_\nu^2 c^2$, where m_ν is the rest mass of the neutrino.

The density of the charged lepton states may be written as

$$dn_e = \frac{V}{2\pi^2 \hbar^3} F(Z, E_e) p_e^2 dp_e,$$

where $F(Z, E_e)$, known as Fermi function, accounts for the interaction between the charged lepton and the Coulomb field of the daughter nucleus.

It is convenient to express the final energies of the neutrino in terms of the so called end-point energy E_0, that is the maximum kinetic energy of the charged lepton,

$$E_\nu = E_0 - E_e.$$

Substituting all E_ν energies with the last expression and integrating over the momenta of the charged lepton gives the final form of the transition rates (for more detailed derivation, see for example [67]),

$$\begin{aligned} W = \frac{m_e^5 c^4}{2\pi^3 \hbar^7} f(Z, E_0) \Big| \sum_{M_f} \Big[C_V \left\langle J_f M_f; T_f T_{z,f}, \zeta_f \right| \sum_{j=1}^{A} \tau_j^{\pm} \left| J_i M_i; T_i T_{z,i}, \zeta_i \right\rangle \\ + \quad C_A \sum_{\mu} \left\langle J_f M_f; T_f T_{z,f}, \zeta_f \right| \sum_{j=1}^{A} \sigma_{\mu,j} \tau_j^{\pm} \left| J_i M_i; T_i T_{z,i}, \zeta_i \right\rangle \Big] \Big|^2 \end{aligned}$$

where $f(Z, E_0)$ is known as Fermi integral (tables of calculated values of $f(Z, E_0)$ are available in Ref. [80]).

B.2 Neutrinoless Double-Beta Decay Matrix Elements

The Gamow-Teller (GT), Fermi (F), and tensor (T) matrix elements are calculated using the associated transition operators [17]

$$\begin{aligned} M_{0\nu}^{GT} &= \frac{2R}{\pi g_A^2} \int_0^\infty q dq \left\langle f \right| \sum_{a,b} \frac{j_0(q r_{ab}) h_{GT}(q) \sigma_a \cdot \sigma_b}{q + \bar{E} - (E_i + E_f)/2} \tau_a^+ \tau_b^+ \left| i \right\rangle, \\ M_{0\nu}^{F} &= \frac{2R}{\pi g_A^2} \int_0^\infty q dq \left\langle f \right| \sum_{a,b} \frac{j_0(q r_{ab}) h_{F}(q)}{q + \bar{E} - (E_i + E_f)/2} \tau_a^+ \tau_b^+ \left| i \right\rangle, \\ M_{0\nu}^{T} &= \frac{2R}{\pi g_A^2} \int_0^\infty q dq \left\langle f \right| \sum_{a,b} \frac{j_2(q r_{ab}) h_{T}(q) [3\sigma_j \cdot \hat{\mathbf{r}}_{ab} \sigma_k \cdot \hat{\mathbf{r}}_{ab} - \sigma_a \cdot \sigma_b]}{q + \bar{E} - (E_i + E_f)/2} \tau_a^+ \tau_b^+ \left| i \right\rangle, \end{aligned}$$

where R is the nuclear radius, q is the momentum transfer, $r_{ab} = |\mathbf{r_a} - \mathbf{r_b}|$ is the magnitude of the inter-nucleon position vector, and $\hat{\mathbf{r}}_{ab} = (\mathbf{r_a} - \mathbf{r_b})/r_{ab}$ is the corresponding unit vector.

The many-particle states $|i\rangle$ and $|f\rangle$ denote the initial and final states of the nucleus and will be calculated as part of this project using SA-NCSM. The functions j_0 and j_2 are spherical Bessel functions, and h_{GT}, h_F and h_T are so called neutrino potentials, defined as

$$\begin{aligned} h_{GT}(q) &\equiv g_A^2(\mathbf{q}^2) - \frac{g_A(\mathbf{q}^2)g_P(\mathbf{q}^2)\mathbf{q}^2}{3m_N} + \frac{g_P^2(\mathbf{q}^2)\mathbf{q}^4}{12m_N^2} + \frac{g_M^2(\mathbf{q}^2)\mathbf{q}^2}{6m_N^2}, \\ h_F(q) &\equiv \frac{g_V^2(\mathbf{q}^2)}{g_A^2}, \\ h_T(q) &\equiv \frac{g_A(\mathbf{q}^2)g_P(\mathbf{q}^2)\mathbf{q}^2}{3m_N} - \frac{g_P^2(\mathbf{q}^2)\mathbf{q}^4}{12m_N^2} + \frac{g_M^2(\mathbf{q}^2)\mathbf{q}^2}{12m_N^2}. \end{aligned}$$

Appendix C Derivation of the $j_{2,3}$ Recoil-order Terms from Impulse Approximation

The derivation of expressions for j_2 and j_3 in Ref. [24] starts from writing down the axial weak current for allowed beta decay and keeping up to next-to-leading order terms (Eq. 7b in the Ref. [24]):

$$\begin{aligned} l^\mu \langle \beta, J'M' | A_\mu | \alpha, JM \rangle &= C^{JM}_{J'M'1k}\epsilon_{ijk}\epsilon_{ij\lambda\eta}\frac{1}{4M}\big[c(q^2)l^\lambda P^\eta - d(q^2)l^\lambda q^\eta \\ &+ \frac{1}{(2M)^2}h(q^2)q^\lambda P^\eta \mathbf{q}\cdot\mathbf{l}\big] \\ &+ C^{JM}_{J'M'2k}C^{2k}_{1n2n'}l_n(4\pi/5)^{1/2}Y_{2n'}(\hat{q})\frac{q^2}{(2M)^2}j_2(q^2) \\ &+ C^{JM}_{J'M'3k}C^{3k}_{1n2n'}l_n(4\pi/5)^{1/2}Y_{2n'}(\hat{q})\frac{q^2}{(2M)^2}j_3(q^2), \end{aligned} \tag{C.1}$$

where l^μ and A^μ are the lepton current and the axial weak current four-vectors (sum over all repeating indices is assumed). Since we are interested in only j_2 and j_3 expressions, we consider only the last two terms of the equation. The angular momenta J with projection M and J' with projection M' correspond to respectively parent and daughter nuclei. The first Clebsch-Gordan coefficients arise from reducing the matrix elements through Wigner-Eckart theorem while the second ones come from coupling of spherical tensors inside j_2 and j_3. Both of these will be discussed below. The M in denominator is the average mass of the parent and daughter nuclei and q is the momentum transfer. Throughout this section following the paper's convention we use $\hbar = 1 = c$.

After introducing the impulse approximation the vector part of the axial current has the following form (Eq. 66 in Ref. [24]):

$$\begin{aligned} \mathbf{A}^\pm(\mathbf{r}_i) &= -\tau_i^\pm\sigma_i \exp(-i\mathbf{q}\cdot\mathbf{r}_i)[g_A(q^2) \mp (q_0/2m)g_{II}(q^2)] \\ &- \tau_i^\pm\sigma_i\cdot\mathbf{q}\exp(i\mathbf{q}\cdot\mathbf{r}_i)[q/(2m)^2]g_p(q^2). \end{aligned} \tag{C.2}$$

The subscript i corresponds to one nucleon in the nucleus (no sum over i is assumed here).

The expressions for j_2 and j_3 depend only on the axial coupling g_A, thus only the first term in Eq. (C.2) is of interest. As the paper suggests we need to expand the exponent and compare to the Eq. (C.1) in this document:

$$\begin{aligned} & -\tau_i^{\pm}\sigma_i \exp(-i\mathbf{q}\cdot\mathbf{r}_i) g_A(q^2) \\ = \; & -g_A(q^2)\tau_i^{\pm}\sigma_i 4\pi \sum_{l,m} (-i)^l j_l(qr_i)(-)^m Y_{lm}(\hat{q}) Y_{l-m}(\hat{r}) \\ \approx \; & -4\pi g_A(q^2)\tau_i^{\pm}\sigma_i \sum_{l,m} (-i)^l \frac{2^l l!(qr)^l}{(2l+1)!}(-)^m Y_{lm}(\hat{q}) Y_{l-m}(\hat{r}), \end{aligned} \tag{C.3}$$

where we used the plane wave expansion from Ref. [180] cited by Ref. [24] and the asymptotic form for the spherical Bessel function (valid in case of the impulse approximation):

$$\lim_{x\to 0} j_l(x) = \frac{2^l l!}{(2l+1)!} x^l.$$

The last two terms in Eq. (C.1) contain only q^2, meaning that j_2 and j_3 correspond to $l = 2$ terms of the expansion in (C.3) (note, $l = 0$ corresponds to the Gamow-Teller matrix element)

$$\frac{4\pi}{15} g_A(q^2)\tau_i^{\pm}\sigma_i \sum_m (-)^m Y_{2m}(\hat{q}) Y_{2-m}(\hat{r}) q^2 r_i^2. \tag{C.4}$$

Next, we note that

$$l^\mu \langle \beta, J'M' | A_\mu | \alpha, JM \rangle = l^0 \langle \beta, J'M' | A_0 | \alpha, JM \rangle - \mathbf{l} \cdot \langle \beta, J'M' | \mathbf{A} | \alpha, JM \rangle . \tag{C.5}$$

The expression (C.4) is one of the terms of $\mathbf{A}$, so in order to compare it to Eq. (C.1) we

substitute it in the second term of Eq. (C.5):

$$-\sum_i \sum_{m'} (-)^{m'} l_{m'} \langle \beta, J'M' | \frac{4\pi}{15} g_A(q^2) \tau_i^{\pm} \sigma_{-m',i} \sum_m (-)^m Y_{2m}(\hat{q}) Y_{2-m}(\hat{r}) q^2 r_i^2 | \alpha, JM \rangle$$
$$= -\frac{4\pi}{15} g_A(q^2) \sum_i \sum_{m,m'} (-)^{m+m'} l_{m'} Y_{2m}(\hat{q}) q^2$$
$$\times \langle \beta, J'M' | \tau_i^{\pm} r_i^2 \sum_{K,k} C^{K-k}_{1-m'2-m} \left[\sigma_i \times Y_2(\hat{r})\right]_{K-k} | \alpha, JM \rangle . \quad \text{(C.6)}$$

Here, we expressed the $\mathbf{l}$ and σ_i vector operators in spherical basis and used the scalar product relation

$$\mathbf{a} \cdot \mathbf{b} = \sum_{m'} (-)^{m'} a_{m'} b_{-m'}.$$

We choose to couple to $-k$ for convenience ($m + m' = k$).

To obtain the expressions for j_2 and j_3 we need to reduce the matrix element in eq. (C.6) and compare to the last two terms in eq. (C.1). We use the commonly used Wigner-Eckart convention given on Ref. [181] page 475. It is important to note that Ref. [24] did not use this convention, apparently the reduction in his paper was done by coupling the final state and the spherical tensor to give the initial state. In addition we use the symmetry property of Clebsch-Gordan coefficients (see, e.g., page 245 of Ref. [181]):

$$C^{jm}_{j_1 m_1 j_2 m_2} = (-)^{j_1+j_2-j} C^{j-m}_{j_1 -m_1 j_2 -m_2}.$$

After the reduction Eq. (C.6) becomes

$$-\frac{4\pi}{15} g_A(q^2) \sum_i \sum_{m,m'} \sum_{K,k} (-)^k (-)^{1+2-K} l_{m'} Y_{2m}(\hat{q}) q^2 C^{Kk}_{1m'2m} \frac{C^{J'M'}_{JMK-k}}{\sqrt{2J'+1}}$$
$$\times \langle \beta, J' \| \tau_i^{\pm} r_i^2 \left[\sigma_i \times Y_2(\hat{r})\right]_K \| \alpha, J \rangle. \quad \text{(C.7)}$$

Considering that the Clebsch-Gordan coefficients should match with the ones in Eq. (C.1)

we use the relations on page 245 in Ref. [181] to exchange JM and $J'M'$:

$$C^{J'M'}_{JMK-k} = (-)^{K-k}\sqrt{\frac{2J'+1}{2J+1}}C^{JM}_{KkJ'M'} = (-)^{K-k}(-)^{J'+K-J}\sqrt{\frac{2J'+1}{2J+1}}C^{JM}_{J'M'Kk}.$$

Taking this relation into account, dropping the sums over repeating indices (except i) and adding some constant factors the Eq. (C.7) becomes

$$\begin{aligned} &-\sqrt{\frac{4\pi}{5}}(-)^{J'-J}(-)^{1+2-K}l_{m'}Y_{2m}(\hat{q})\frac{q^2}{(2M)^2}C^{Kk}_{1m'2m}\frac{C^{JM}_{J'M'Kk}}{\sqrt{2J+1}} \\ &\times(2M^2/3)(16\pi/5)^{1/2}g_A(q^2)\langle\beta,J'\|\sum_i\tau_i^{\pm}r_i^2\left[\sigma_i\times Y_2(\hat{r})\right]_K\|\alpha,J\rangle. \end{aligned} \tag{C.8}$$

The $K=2$ and $K=3$ terms of this expression correspond to the last two terms in eq. (C.1). Thus the expression for j_2 and j_3 will be

$$j_K = -(-)^{J'-J}\frac{2M^2}{3}\frac{g_A(q^2)}{\sqrt{2J+1}}\langle\beta,J'\|\sqrt{\frac{16\pi}{5}}\sum_i\tau_i^{\pm}r_i^2\left[Y_2(\hat{r})\times\sigma_i\right]_K\|\alpha,J\rangle. \tag{C.9}$$

The original expression in Ref. [24] is the following (Eqs. 67 and 68):

$$j_K = -\frac{2M^2}{3}g_A(q^2)\langle\beta,J'\|\sqrt{\frac{16\pi}{5}}\sum_i\tau_i^{\pm}r_i^2\left[\sigma_i\times Y_2(\hat{r})\right]_K\|\alpha,J\rangle_H. \tag{C.10}$$

The difference between these relations comes from the convention difference between the reduced matrix elements. The Wigner-Eckart theorem used in Ref. [24] reads

$$\langle J'M'|\,\hat{O}^{K-k}\,|JM\rangle = C^{JM}_{J'M'Kk}\langle J'\|\hat{O}^K\|J\rangle_H, \tag{C.11}$$

while in our convention it looks like

$$\langle J'M'|\,\hat{O}^{K-k}\,|JM\rangle = \frac{(-)^{J'-J+k}}{\sqrt{2J+1}}C^{JM}_{J'M'Kk}\langle J'\|\hat{O}^K\|J\rangle. \tag{C.12}$$

Recovering the values of $\hbar$ and c, the form of j_K used in SA-NCSM calculations will look like:

$$\begin{aligned} j_K(q^2) &= -(-)^{J'-J}\frac{2}{3}\frac{g_A(q^2)}{\sqrt{2J+1}}\frac{M^2c^4}{(\hbar c)^2}\left\langle J'\right|\left|\sqrt{\frac{16\pi}{5}}\sum_i^A \tau_i^{\pm} r_i^2[Y_2(\hat{r}_i)]^K \times \sigma_i\right|\left|J\right\rangle \\ &= -(-)^{J'-J}\frac{2}{3}\frac{g_A(q^2)}{\sqrt{2J+1}}\frac{(Am_N)^2c^4}{(\hbar c)^2}b^2\left\langle J'\right|\left|\sum_i^A \tau_i^{\pm}[\hat{Q}_2(\hat{r}_i)\times\sigma_i]^K\right|\left|J\right\rangle \\ &= -(-)^{J'-J}\frac{2}{3}\frac{g_A(q^2)}{\sqrt{2J+1}}\frac{A^2m_Nc^2}{\hbar\Omega}\left\langle J'\right|\left|\sum_i^A \tau_i^{\pm}[\hat{Q}_2(\hat{r}_i)\times\sigma_i]^K\right|\left|J\right\rangle, \end{aligned} \tag{C.13}$$

where all of the reduced matrix elements are with respect to the spatial-spin (not isospin). Alternatively,

$$\frac{j_K(q^2)}{A^2c_0} = -\frac{2}{3}\frac{m_Nc^2}{\hbar\Omega}\frac{\left\langle J'\right|\left|\sum_i^A \tau_i^{\pm}[\hat{Q}_2(\hat{r}_i)\times\sigma_i]^K\right|\left|J\right\rangle}{\left\langle J'\right|\left|\sum_i^A \tau_i^{\pm}\sigma_i\right|\left|J\right\rangle}, \tag{C.14}$$

$$\text{with } c_0 = (-)^{J'-J}\frac{g_A(q^2)}{\sqrt{2J+1}}\left\langle J'\right|\left|\sum_i^A \tau_i^{\pm}\sigma_i\right|\left|J\right\rangle, \tag{C.15}$$

where m_N is the nucleon mass ($m_Nc^2 = 938.92$ MeV), $Mc^2 = (M_1 + M_2)c^2/2$ is the arithmetic average of the parent and daughter masses in MeV, g_A is the axial coupling constant (unitless), A is the mass number ($A = 8$), $\hbar\Omega$ is a basis parameter in the SA-NCSM (final results are independent of $\hbar\Omega$), and

$$b^2 = \frac{\hbar}{m_N\Omega} = \frac{(\hbar c)^2}{mc_N^2\hbar\Omega}[\text{fm}^2] \tag{C.16}$$

$$\hat{Q}_2 = \sqrt{\frac{16\pi}{5}}\sum_i \bar{r}_i^2 Y_2(\hat{r}_i)\,[\text{unitless}], r_i = b\bar{r}_i[\text{fm}] \tag{C.17}$$

$$\sigma_{\pm1} = \mp\frac{\sigma_x \pm i\sigma_y}{\sqrt{2}},\ \sigma_0 = \sigma_z, \tag{C.18}$$

where $\sigma_{x,y,z}$ are the Pauli spin matrices, $s_i = \sigma_i/2$, with $s_0\left|\frac{1}{2}s_z\right\rangle = s_z\left|\frac{1}{2}s_z\right\rangle$ (spin) and $\tau_0\left|\frac{1}{2}t_z\right\rangle = t_z\left|\frac{1}{2}t_z\right\rangle$ (isospin).

References

[1] K. D. Launey, T. Dytrych, and J. P. Draayer. Symmetry-guided large-scale shell-model theory. *Prog. Part. Nucl. Phys.*, 89:101 (review), 2016.

[2] T. Dytrych, K. D. Launey, J. P. Draayer, D. J. Rowe, J. L. Wood, G. Rosensteel, C. Bahri, D. Langr, and R. B. Baker. Physics of nuclei: Key role of an emergent symmetry. *Phys. Rev. Lett.*, 124:042501, Jan 2020.

[3] Kristina D Launey, Tomáš Dytrych, Grigor H Sargsyan, Robert B Baker, and Jerry P Draayer. Emergent symplectic symmetry in atomic nuclei. *The European Physical Journal Special Topics*, 229(14):2429–2441, 2020.

[4] Y Fukuda, T Hayakawa, E Ichihara, K Inoue, K Ishihara, H Ishino, Y Itow, T Kajita, J Kameda, S Kasuga, et al. Evidence for oscillation of atmospheric neutrinos. *Physical Review Letters*, 81(8):1562, 1998.

[5] J. M. Yao and J. Engel. Octupole correlations in low-lying states of ^{150}Nd and ^{150}Sm and their impact on neutrinoless double-β decay. *Phys. Rev. C*, 94:014306, Jul 2016.

[6] Nuria López Vaquero, Tomás R. Rodríguez, and J. Luis Egido. Shape and Pairing Fluctuation Effects on Neutrinoless Double Beta Decay Nuclear Matrix Elements. *Phys. Rev. Lett.*, 111:142501, Sep 2013.

[7] Juhani Hyvärinen and Jouni Suhonen. Nuclear matrix elements for $0\nu\beta\beta$ decays with light or heavy Majorana-neutrino exchange. *Phys. Rev. C*, 91:024613, Feb 2015.

[8] M. T. Mustonen and J. Engel. Large-scale calculations of the double-β decay of ^{76}**Ge**, ^{130}**Te**, ^{136}**Xe**, and ^{150}**Nd** in the deformed self-consistent skyrme quasiparticle random-phase approximation. *Phys. Rev. C*, 87:064302, Jun 2013.

[9] Dong-Liang Fang, Amand Faessler, and Fedor Simkovic. Partial restoration of isospin symmetry for neutrinoless double β decay in the deformed nuclear system of ^{150}Nd. *Phys. Rev. C*, 92:044301, Oct 2015.

[10] J. Barea, J. Kotila, and F. Iachello. $0\nu\beta\beta$. *Phys. Rev. C*, 91:034304, Mar 2015.

[11] Mihai Horoi and Andrei Neacsu. Shell model predictions for ^{124}Sn double-β decay. *Phys. Rev. C*, 93:024308, Feb 2016.

[12] J Menendez, A Poves, E Caurier, and F Nowacki. Disassembling the nuclear matrix elements of the neutrinoless β β decay. *Nuclear Physics A*, 818(3-4):139–151, 2009.

[13] A Belley, CG Payne, SR Stroberg, T Miyagi, and JD Holt. Ab initio neutrinoless double-beta decay matrix elements for ca 48, ge 76, and se 82. *Physical Review Letters*, 126(4):042502, 2021.

[14] J. M. Yao, B. Bally, J. Engel, R. Wirth, T. R. Rodríguez, and H. Hergert. Ab Initio Treatment of Collective Correlations and the Neutrinoless Double Beta Decay of ^{48}Ca. *Phys. Rev. Lett.*, 124:232501, Jun 2020.

[15] S. Novario, P. Gysbers, J. Engel, G. Hagen, G. R. Jansen, T. D. Morris, P. Navrátil, T. Papenbrock, and S. Quaglioni. Coupled-cluster calculations of neutrinoless double-β decay in ^{48}Ca. *Phys. Rev. Lett.*, 126:182502, May 2021.

[16] Jiangming Yao. Advances in modeling nuclear matrix elements of neutrinoless double beta decay. *Science Bulletin*, 66(1):3–5, 2021.

[17] Jonathan Engel and Javier Menéndez. Status and future of nuclear matrix elements for neutrinoless double-beta decay: a review. *Reports on Progress in Physics*, 80(4):046301, 2017.

[18] Krishna Kumar. *National Nuclear Physics Summer School*, 2017.

[19] Jonathan Engel. *Private communication*, 2017.

[20] M Włoch, David J Dean, Jeffrey R Gour, Morten Hjorth-Jensen, Karol Kowalski, Thomas Papenbrock, and Piotr Piecuch. Ab-initio coupled-cluster study of ^{16}O. *Physical review letters*, 94(21):212501, 2005.

[21] Koshiroh Tsukiyama, SK Bogner, and A Schwenk. In-medium similarity renormalization group for nuclei. *Physical review letters*, 106(22):222502, 2011.

[22] P Herczeg. Beta decay beyond the standard model. *Progress in Particle and Nuclear Physics*, 46(2):413–457, 2001.

[23] MG Sternberg, R Segel, ND Scielzo, G Savard, JA Clark, PF Bertone, F Buchinger, M Burkey, S Caldwell, A Chaudhuri, et al. Limit on tensor currents from ^{8}Li β decay. *Physical review letters*, 115(18):182501, 2015.

[24] Barry R. Holstein. Recoil effects in allowed beta decay: The elementary particle approach. *Rev. Mod. Phys.*, 46:789–814, Oct 1974.

[25] T Sumikama, K Matsuta, T Nagatomo, M Ogura, T Iwakoshi, Y Nakashima, H Fujiwara, M Fukuda, M Mihara, K Minamisono, et al. Test of the conserved vector current hypothesis by a β-ray angular distribution measurement in the mass-8 system. *Physical Review C*, 83(6):065501, 2011.

[26] Maria Goeppert Mayer. On Closed Shells in Nuclei. II. *Phys. Rev.*, 75:1969–1970, Jun 1949.

[27] R Machleidt. High-precision, charge-dependent Bonn nucleon-nucleon potential. *Physical Review C*, 63(2):024001, 2001.

[28] VGJ Stoks, RAM Klomp, CPF Terheggen, and JJ De Swart. Construction of high-quality NN potential models. *Physical Review C*, 49(6):2950, 1994.

[29] DR Entem and R Machleidt. Accurate charge-dependent nucleon-nucleon potential at fourth order of chiral perturbation theory. *Physical Review C*, 68(4):041001, 2003.

[30] AM Shirokov, VA Kulikov, P Maris, AI Mazur, EA Mazur, and JP Vary. NN interaction JISP16: Current status and prospect. In *EPJ Web of Conferences*, volume 3, pages 5–15. EDP Sciences, 2010.

[31] P Doleschall. Influence of the short range nonlocal nucleon-nucleon interaction on the elastic n-d scattering: Below 30 MeV. *Physical Review C*, 69(5):054001, 2004.

[32] A. Ekström, G. Baardsen, C. Forssén, G. Hagen, M. Hjorth-Jensen, G. R. Jansen, R. Machleidt, W. Nazarewicz, et al. An optimized chiral nucleon-nucleon interaction at next-to-next-to-leading order. *Phys. Rev. Lett.*, 110:192502, 2013.

[33] Susumu Okubo. Diagonalization of hamiltonian and tamm-dancoff equation. *Progress of Theoretical Physics*, 12(5):603–622, 1954.

[34] K. Suzuki and S. Y. Lee. *Prog. Theor. Phys.*, 64:2091, 1980.

[35] S. K. Bogner, R. J. Furnstahl, and R. J. Perry. Similarity Renormalization Group for Nucleon-nucleon Interactions. *Phys. Rev. C*, 75:061001(R), 2007.

[36] A. Bohr and B. R. Mottelson. *Nuclear structure*, volume 1. Benjamin, New York, 1969.

[37] J. P. Elliott. Collective Motion in the Nuclear Shell Model. I. Classification Schemes for States of Mixed Configurations. *Proc. Roy. Soc. A*, 245:128, 1958.

[38] J. P. Elliott. Collective Motion in the Nuclear Shell Model. II. The Introduction of Intrinsic Wave-Functions. *Proc. Roy. Soc. A*, 245:562, 1958.

[39] T. Dytrych. `LSU3shell` *code*. Louisiana State University, available under the GNU General Public License at the git repository, http://sourceforge.net/ projects/lsu3shell, 2013.

[40] J. P. Draayer, Y. Leschber, S. C. Park, and R. Lopez. Representations of U(3) in U(N). *Comput. Phys. Commun.*, 56:279, 1989.

[41] Y. Akiyama and J. P. Draayer. A User's Guide to FORTRAN Programs for Wigner and Racah Coefficients of SU(3). *Comput. Phys. Commun.*, 5:405, 1973.

[42] J. P. Draayer and Y. Akiyama. Wigner and Racah Coefficients for SU(3). *J. Math. Phys.*, 14:1904, 1973.

[43] G. H. Sargsyan, K. D. Launey, R. B. Baker, T. Dytrych, and J. P. Draayer. SU(3)-guided realistic nucleon-nucleon interactions for large-scale calculations. *Phys. Rev. C*, 103:044305, Apr 2021.

[44] KT Hecht and JP Draayer. Spectral distributions and the breaking of isospin and supermultiplet symmetries in nuclei. *Nuclear Physics A*, 223(2):285, 1974.

[45] J. B. French. *Phys. Lett.*, 23:248, 1966.

[46] J. B. French and K. F. Ratcliff. *Phys. Rev. C*, 3:94, 1971.

[47] F. S. Chang, J. B. French, and T. H. Thio. *Ann. Phys. (N.Y.)*, 66:137, 1971.

[48] V. K. B. Kota and R. U. Haq. *Spectral Distributions in Nuclei and Statistical Spectroscopy*. World Scientific Publishing Co., 2010.

[49] Kristina D Launey, S Sarbadhicary, Tomás Dytrych, and Jerry P Draayer. Program in c for studying characteristic properties of two-body interactions in the framework of spectral distribution theory. *Computer Physics Communications*, 185(1):254–267, 2014.

[50] David J. Rowe. Nuclear shape coexistence from the perspective of an algebraic many-nucleon version of the bohr-mottelson unified model. *Phys. Rev. C*, 101:054301, May 2020.

[51] F. Ajzenberg-Selove and J.H. Kelley. *Nucl. Phys. A*, 506:1, 1990.

[52] I. Tanihata, H. Hamagaki, O. Hashimoto, Y. Shida, N. Yoshikawa, K. Sugimoto, O. Yamakawa, T. Kobayashi, and N. Takahashi. Measurements of interaction cross sections and nuclear radii in the light p-shell region. *Phys. Rev. Lett.*, 55:2676–2679, Dec 1985.

[53] T. Dytrych, P. Maris, K. D. Launey, J. P. Draayer, J. P. Vary, M. Caprio, D. Langr, U. Catalyurek, and M. Sosonkina. Efficacy of the SU(3) scheme for *ab initio* large-scale calculations beyond the lightest nuclei. *Comput. Phys. Commun.*, 207, 2016.

[54] A. Bohr and B. R. Mottelson. *Nuclear Structure*, volume 1. Benjamin, New York, 1969.

[55] R. B. Wiringa, V. G. J. Stoks, and R. Schiavilla. Accurate nucleon-nucleon potential with charge-independence breaking. *Phys. Rev. C*, 51:38–51, Jan 1995.

[56] GK Tobin, MC Ferriss, KD Launey, T Dytrych, JP Draayer, AC Dreyfuss, and C Bahri. Symplectic no-core shell-model approach to intermediate-mass nuclei. *Physical Review C*, 89(3):034312, 2014.

[57] C Bahri, J Escher, and JP Draayer. Monopole-pairing and deformation in atomic nuclei. *Nuclear Physics A*, 592(2):171–193, 1995.

[58] Takaharu Otsuka, Toshio Suzuki, Rintaro Fujimoto, Hubert Grawe, and Yoshinori Akaishi. Evolution of nuclear shells due to the tensor force. *Phys. Rev. Lett.*, 95:232502, Nov 2005.

[59] M. Harvey. The Nuclear SU(3) Model. *Adv. Nucl. Phys.*, 1:67, 1968.

[60] R.D. Ratna Raju, J.R Draayer, and K.T. Hecht. *Nucl. Phys. A*, 202:433, 1973.

[61] A.P. Zuker, J. Retamosa, A. Poves, and E. Caurier. *Phys. Rev. C*, 52:1741(R), 1995.

[62] C.E. Vargas, J.G. Hirsch, and J.P. Draayer. *Nucl. Phys. A*, 690:409, 2001.

[63] G. Popa, J. G. Hirsch, and J. P. Draayer. *Phys. Rev. C*, 62:064313, 2000.

[64] T. Beuschel, J. P. Draayer, D. Rompf, and J. G. Hirsch. *Phys. Rev. C*, 57:1233, 1998.

[65] Andriana Martinou, Dennis Bonatsos, N Minkov, IE Assimakis, SK Peroulis, S Sarantopoulou, and J Cseh. Proxy-SU (3) symmetry in the shell model basis. *The European Physical Journal A*, 56(9):1–18, 2020.

[66] Jouni Suhonen. *From Nucleons to Nucleus*. Springer, 2007.

[67] Samuel SM Wong. *Introductory Nuclear Physics*. John Wiley & Sons, 2008.

[68] P. Ruotsalainen, J. Henderson, G. Hackman, G. H. Sargsyan, K. D. Launey, A. Saxena, P. C. Srivastava, S. R. Stroberg, T. Grahn, J. Pakarinen, G. C. Ball, R. Julin, P. T. Greenlees, J. Smallcombe, C. Andreoiu, N. Bernier, M. Bowry, M. Buckner, R. Caballero-Folch, A. Chester, S. Cruz, L. J. Evitts, R. Frederick, A. B. Garnsworthy, M. Holl, A. Kurkjian, D. Kisliuk, K. G. Leach, E. McGee, J. Measures, D. Mücher, J. Park, F. Sarazin, J. K. Smith, D. Southall, K. Starosta, C. E. Svensson, K. Whitmore, M. Williams, and C. Y. Wu. Isospin symmetry in $B(E2)$ values: Coulomb excitation study of ^{21}Mg. *Phys. Rev. C*, 99:051301, May 2019.

[69] Daniel Shanks. Non-linear transformations of divergent and slowly convergent sequences. *Journal of Mathematics and Physics*, 34(1-4):1–42, 1955.

[70] J. Williams, G. C. Ball, A. Chester, T. Domingo, A. B. Garnsworthy, G. Hackman, J. Henderson, R. Henderson, R. Krücken, Anil Kumar, K. D. Launey, J. Measures, O. Paetkau, J. Park, G. H. Sargsyan, J. Smallcombe, P. C. Srivastava, K. Starosta, C. E. Svensson, K. Whitmore, and M. Williams. Structure of ^{28}Mg and influence of the neutron pf shell. *Phys. Rev. C*, 100:014322, Jul 2019.

[71] W.J. Vermeer, M.T. Esat, J.A. Kuehner, R.H. Spear, A.M. Baxter, and S. Hinds. Electric quadrupole moment of the first excited state of ^{12}C. *Physics Letters B*, 122(1):23–26, 1983.

[72] J. P. Svenne and Raymond S. Mackintosh. Spin-orbit force and the deformation of ^{12}C. *Phys. Rev. C*, 18:983–990, Aug 1978.

[73] P. Maris, J. P. Vary, and A. M. Shirokov. Ab initio no-core full configuration calculations of light nuclei. *Phys. Rev. C*, 79:014308, Jan 2009.

[74] Rymond H Spear. Static quadrupole moments of first 2^+ states in the 2s-1d shell: A review of experiment and theory. *Physics Reports*, 73(5):369–390, 1981.

[75] U. Gayer, T. Beck, M. Bhike, J. Isaak, N. Pietralla, P. C. Ries, D. Savran, M. Schilling, W. Tornow, and V. Werner. Experimental $M1$ response of ^{40}Ar as a benchmark for neutrino-nucleus scattering calculations. *Phys. Rev. C*, 100:034305, Sep 2019.

[76] Alessandro Mirizzi, Irene Tamborra, H-Th Janka, Ninetta Saviano, Kate Scholberg, Robert Bollig, Lorenz Hüdepohl, and Sovan Chakraborty. Supernova neutrinos: production, oscillations and detection. *La Rivista del Nuovo Cimento*, 39:1–112, 2016.

[77] JH Kelley, JE Purcell, and CG Sheu. Energy levels of light nuclei A = 12. *Nuclear Physics A*, 968:71–253, 2017.

[78] D.R. Tilley, C.M. Cheves, J.H. Kelley, S. Raman, and H.R. Weller. Energy levels of light nuclei, A = 20. *Nuclear Physics A*, 636(3):249–364, 1998.

[79] CS Wu and SA Moszkowski. *Beta Decay, Interscience Monographs and Texts in Physics and Astronomy, Vol. 16*, volume 16. Interscience Publishers, New York, 1966.

[80] U. Fano. *Tables for the Analysis of Beta Spectra*. National Bureau of Standards, Washington, DC, 1951.

[81] A. Sirlin. Remarks concerning the $o(z\alpha^2)$ corrections to fermi decays, conserved-vector-current predictions, and universality. *Phys. Rev. D*, 35:3423–3427, Jun 1987.

[82] Sabin Stoica and Mihail Mirea. New calculations for phase space factors involved in double-β decay. *Physical Review C*, 88(3):037303, 2013.

[83] Vincenzo Cirigliano, Wouter Dekens, Jordy de Vries, Michael L. Graesser, Emanuele Mereghetti, Saori Pastore, and Ubirajara van Kolck. New Leading Contribution to Neutrinoless Double-β Decay. *Phys. Rev. Lett.*, 120:202001, May 2018.

[84] Vincenzo Cirigliano, Wouter Dekens, Emanuele Mereghetti, and André Walker-Loud. Neutrinoless double-β decay in effective field theory: The light-Majorana neutrino-exchange mechanism. *Phys. Rev. C*, 97:065501, Jun 2018.

[85] Vincenzo Cirigliano, Wouter Dekens, Jordy de Vries, Martin Hoferichter, and Emanuele Mereghetti. Toward Complete Leading-Order Predictions for Neutrinoless Double β Decay. *Phys. Rev. Lett.*, 126:172002, Apr 2021.

[86] W.-T. Chou, E. K. Warburton, and B. A. Brown. Gamow-teller beta-decay rates for $a \leq 18$ nuclei. *Phys. Rev. C*, 47:163–177, Jan 1993.

[87] G. Martínez-Pinedo, A. Poves, E. Caurier, and A. P. Zuker. Effective g_A in the pf shell. *Phys. Rev. C*, 53:R2602–R2605, Jun 1996.

[88] S. Pastore, A. Baroni, J. Carlson, S. Gandolfi, Steven C. Pieper, R. Schiavilla, and R. B. Wiringa. Quantum monte carlo calculations of weak transitions in $a = 6 - -10$ nuclei. *Phys. Rev. C*, 97:022501, Feb 2018.

[89] P Gysbers, Gaute Hagen, JD Holt, Gustav R Jansen, Titus D Morris, P Navrátil, T Papenbrock, S Quaglioni, A Schwenk, SR Stroberg, et al. Discrepancy between experimental and theoretical β-decay rates resolved from first principles. *Nature Physics*, 15(5):428–431, 2019.

[90] S. Pastore, J. Carlson, V. Cirigliano, W. Dekens, E. Mereghetti, and R. B. Wiringa. Neutrinoless double-β decay matrix elements in light nuclei. *Phys. Rev. C*, 97:014606, Jan 2018.

[91] Xiao Bao Wang, AC Hayes, J Carlson, GX Dong, Emanuele Mereghetti, Saori Pastore, and RB Wiringa. Comparison between variational Monte Carlo and shell model calculations of neutrinoless double beta decay matrix elements in light nuclei. *Physics Letters B*, 798:134974, 2019.

[92] V. Cirigliano, W. Dekens, J. de Vries, M. L. Graesser, E. Mereghetti, S. Pastore, M. Piarulli, U. van Kolck, and R. B. Wiringa. Renormalized approach to neutrinoless double-β decay. *Phys. Rev. C*, 100:055504, Nov 2019.

[93] R. A. M. Basili, J. M. Yao, J. Engel, H. Hergert, M. Lockner, P. Maris, and J. P. Vary. Benchmark neutrinoless double-β decay matrix elements in a light nucleus. *Phys. Rev. C*, 102:014302, Jul 2020.

[94] J. M. Yao, A. Belley, R. Wirth, T. Miyagi, C. G. Payne, S. R. Stroberg, H. Hergert, and J. D. Holt. Ab initio benchmarks of neutrinoless double-β decay in light nuclei with a chiral hamiltonian. *Phys. Rev. C*, 103:014315, Jan 2021.

[95] Robert Roth. Importance truncation for large-scale configuration interaction approaches. *Phys. Rev. C*, 79:064324, Jun 2009.

[96] S. R. Stroberg, H. Hergert, J. D. Holt, S. K. Bogner, and A. Schwenk. Ground and excited states of doubly open-shell nuclei from ab initio valence-space hamiltonians. *Phys. Rev. C*, 93:051301, May 2016.

[97] M Shamsuzzoha Basunia. Nuclear data sheets for $a = 22$. *Nuclear Data Sheets*, 127:69–190, 2015.

[98] T Iida, K Nakajima, S Ajimura, T Batpurev, WM Chan, K Fushimi, R Hazama, H Kakubata, BT Khai, T Kishimoto, et al. Status and future prospect of 48ca double beta decay search in candles. In *Journal of Physics: Conference Series*, volume 718, page 062026. IOP Publishing, 2016.

[99] K. D. Launey, A. Mercenne, and T. Dytrych. Nuclear dynamics and reactions in the ab initio symmetry-adapted framework. *Annu. Rev. Nucl. Part. Sci.*, page accepted, 2021.

[100] Richard P Feynman and Murray Gell-Mann. Theory of the Fermi interaction. *Physical Review*, 109(1):193, 1958.

[101] Eo CG Sudarshan and RE Marshak. Chirality invariance and the universal Fermi interaction. *Physical Review*, 109(5):1860, 1958.

[102] C. S. Wu, E. Ambler, R. W. Hayward, D. D. Hoppes, and R. P. Hudson. Experimental test of parity conservation in beta decay. *Phys. Rev.*, 105:1413–1415, Feb 1957.

[103] W. B. Herrmannsfeldt, D. R. Maxson, P. Stähelin, and J. S. Allen. Electron-neutrino angular correlation in the positron decay of argon 35. *Phys. Rev.*, 107:641–643, Jul 1957.

[104] CH Johnson, Frances Pleasonton, and TA Carlson. Precision measurement of the recoil energy spectrum from the decay of ^{6}He. *Physical Review*, 132(3):1149, 1963.

[105] X Fléchard, Ph Velten, E Liénard, A Méry, D Rodríguez, G Ban, D Durand, F Mauger, O Naviliat-Cuncic, and JC Thomas. Measurement of the β–ν correlation coefficient $a_{\beta\nu}$ in the β decay of trapped ^{6}He+ ions. *Journal of Physics G: Nuclear and Particle Physics*, 38(5):055101, 2011.

[106] G. Li, R. Segel, N. D. Scielzo, P. F. Bertone, F. Buchinger, S. Caldwell, A. Chaudhuri, J. A. Clark, J. E. Crawford, C. M. Deibel, J. Fallis, S. Gulick, G. Gwinner, D. Lascar, A. F. Levand, M. Pedretti, G. Savard, K. S. Sharma, M. G. Sternberg, T. Sun, J. Van Schelt, R. M. Yee, and B. J. Zabransky. Tensor interaction limit derived from the $\alpha-\beta-\overline{\nu}$ correlation in trapped ^{8}Li ions. *Phys. Rev. Lett.*, 110:092502, Mar 2013.

[107] Nathal Severijns, Marcus Beck, and Oscar Naviliat-Cuncic. Tests of the standard electroweak model in nuclear beta decay. *Reviews of Modern Physics*, 78(3):991, 2006.

[108] Frederik Wauters, Alejandro García, and Ran Hong. Limits on tensor-type weak currents from nuclear and neutron β decays. *Physical Review C*, 89(2):025501, 2014.

[109] Melvin Alexander Preston. *Physics of the Nucleus*. Addison-Wesley, 1962.

[110] L Grenacs. Induced Weak Currents in Nuclei. *Annual Review of Nuclear and Particle Science*, 35(1):455–500, 1985.

[111] L. De Braeckeleer, E. G. Adelberger, J. H. Gundlach, M. Kaplan, D. Markoff, A. M. Nathan, W. Schieff, K. A. Snover, D. W. Storm, K. B. Swartz, D. Wright, and B. A. Brown. Radiative decays of the 16.6 and 16.9 MeV states in ^{8}Be and tests of the conservation of the vector current in the A=8 multiplet. *Phys. Rev. C*, 51:2778–2788, May 1995.

[112] T Sumikama, K Matsuta, T Nagatomo, M Ogura, T Iwakoshi, Y Nakashima, H Fujiwara, M Fukuda, M Mihara, K Minamisono, et al. Search for the G-parity irregular term in weak nucleon currents extracted from mirror beta decays in the mass 8 system. *Physics Letters B*, 664(4-5):235–240, 2008.

[113] R. E. Tribble and G. T. Garvey. Induced weak currents and $\beta^{\pm}-\alpha$ angular correlations in $A = 8$. *Phys. Rev. C*, 12:967–983, Sep 1975.

[114] R. D. McKeown, G. T. Garvey, and C. A. Gagliardi. Beta-alpha angular correlations in mass 8. *Phys. Rev. C*, 22:738–749, Aug 1980.

[115] ND Scielzo, Gang Li, MG Sternberg, G Savard, PF Bertone, Fritz Buchinger, Salen Caldwell, JA Clark, John Crawford, CM Deibel, et al. The β-decay paul trap: A radiofrequency-quadrupole ion trap for precision β-decay studies. *Nuclear Instruments and Methods in Physics Research Section A: Accelerators, Spectrometers, Detectors and Associated Equipment*, 681:94–100, 2012.

[116] MT Burkey et al. Utilizing ^{8}Li β Decay to Limit Tensor Currents in the Weak Interaction. *Physical Review Letters,*, To be submitted, 2021.

[117] FC Barker, HJ Hay, and PB Treacy. 0+ states of 8be. *Australian Journal of Physics*, 21(3):239–258, 1968.

[118] FC Barker. 2+ states of 8be. *Australian Journal of Physics*, 22:293–316, 1969.

[119] FC Barker. Delayed alpha spectra from the beta decay of 8li and 8b. *Australian journal of physics*, 42(1):25–40, 1989.

[120] E. Caurier, P. Navrátil, W. E. Ormand, and J. P. Vary. Intruder states in ^{8}Be. *Phys. Rev. C*, 64:051301, Oct 2001.

[121] Pieter Maris. Ab initio calculations for be-isotopes with jisp16. In *Journal of Physics: Conference Series*, volume 445, page 012035. IOP Publishing, 2013.

[122] DM Rodkin and Yu M Tchuvil'sky. Description of alpha-clustering of 8be nucleus states in high-precision theoretical approach. *Chinese Physics C*, 44(12):124105, 2020.

[123] Michael Munch, Oliver Sølund Kirsebom, Jacobus Andreas Swartz, Karsten Riisager, and Hans Otto Uldall Fynbo. Measurement of the full excitation spectrum of the $^{7}\mathrm{Li}(p,\gamma)\alpha\alpha$ reaction at 441 kev. *Physics Letters B*, 782:779 – 784, 2018.

[124] Paulo F. Bedaque and Ubirajara van Kolck. EFFECTIVE FIELD THEORY FOR FEW-NUCLEON SYSTEMS. *Annu. Rev. Nucl. Part. Sci.*, 52(1):339–396, 2002.

[125] E. Epelbaum, A. Nogga, W. Glöckle, H. Kamada, U.-G. Meißner, and H. Witala. Three-nucleon forces from chiral effective field theory. *Phys. Rev. C*, 66:064001, 2002.

[126] D. R. Entem and R. Machleidt. Accurate charge-dependent nucleon-nucleon potential at fourth order of chiral perturbation theory. *Phys. Rev. C*, 68:041001, Oct 2003.

[127] Evgeny Epelbaum. Few-nucleon forces and systems in chiral effective field theory. *Prog. Part. Nucl. Phys.*, 57:654–741, 2006.

[128] K. A. Wendt, C. Forssén, T. Papenbrock, and D. Sääf. Infrared length scale and extrapolations for the no-core shell model. *Phys. Rev. C*, 91:061301, 2015.

[129] P. Navrátil, J. P. Vary, and B. R. Barrett. Properties of ^{12}C in the *Ab Initio* Nuclear Shell Model. *Phys. Rev. Lett.*, 84:5728, 2000.

[130] P. Navrátil, J.P. Vary, and B.R. Barrett. Large-Basis *Ab Initio* No-Core Shell Model and Its Application to ^{12}C. *Phys. Rev. C*, 62:054311, 2000.

[131] A. C. Dreyfuss, K. D. Launey, J. E. Escher, G. H. Sargsyan, R. B. Baker, T. Dytrych, and J. P. Draayer. Clustering and α-capture reaction rate from ab initio symmetry-adapted descriptions of ^{20}Ne. *Phys. Rev. C*, 102:044608, Oct 2020.

[132] A. Ekström, G. R. Jansen, K. A. Wendt, G. Hagen, T. Papenbrock, B. D. Carlsson, C. Forssén, M. Hjorth-Jensen, P. Navrátil, and W. Nazarewicz. Accurate nuclear radii and binding energies from a chiral interaction. *Phys. Rev. C*, 91:051301, May 2015.

[133] R. B. Baker, K. D. Launey, S. Bacca, N. Nevo Dinur, and T. Dytrych. Benchmark calculations of electromagnetic sum rules with a symmetry-adapted basis and hyperspherical harmonics. *Phys. Rev. C*, 102:014320, Jul 2020.

[134] M. Burrows, Ch. Elster, S. P. Weppner, K. D. Launey, P. Maris, A. Nogga, and G. Popa. Ab initio folding potentials for nucleon-nucleus scattering based on no-core shell-model one-body densities. *Phys. Rev. C*, 99:044603, Apr 2019.

[135] Callum McCracken, Petr Navrátil, Anna McCoy, Sofia Quaglioni, and Guillaume Hupin. Microscopic investigation of the ^{8}Li$(n,\gamma)^{9}$Li reaction. *Phys. Rev. C*, 103:035801, Mar 2021.

[136] D. Borremans, D. L. Balabanski, K. Blaum, W. Geithner, S. Gheysen, P. Himpe, M. Kowalska, J. Lassen, P. Lievens, S. Mallion, R. Neugart, G. Neyens, N. Vermeulen, and D. Yordanov. New measurement and reevaluation of the nuclear magnetic andquadrupole moments of ^{8}Li and ^{9}Li. *Phys. Rev. C*, 72:044309, Oct 2005.

[137] GH Sargsyan, KD Launey, MT Burkey, AT Gallant, ND Scielzo, G Savard, A Mercenne, T Dytrych, D Langr, L Varriano, et al. Impact of clustering on the ^{8}Li β decay and recoil form factors. *arXiv preprint arXiv:2107.10389, submitted to Phys. Rev. Lett.*, 2021.

[138] Mary Terese Burkey. *Searching for tensor currents in the weak interaction using lithium-8 β decay.* PhD thesis, Chicago U., 2019.

[139] WJ Huang, Meng Wang, FG Kondev, G Audi, and S Naimi. The AME 2020 atomic mass evaluation (I). Evaluation of input data, and adjustment procedures. *Chinese Physics C*, 45(3):030002, 2021.

[140] A. C. Dreyfuss, K. D. Launey, T. Dytrych, J. P. Draayer, and C. Bahri. Hoyle state and rotational features in Carbon-12 within a no-core shell model framework. *Phys. Lett. B*, 727:511, 2013.

[141] Petr Navrátil, Robert Roth, and Sofia Quaglioni. Ab initio many-body calculations of nucleon scattering on ^{4}He, ^{7}Li, ^{7}Be, ^{12}C, and ^{16}O. *Phys. Rev. C*, 82:034609, Sep 2010.

[142] D.R. Tilley, J.H. Kelley, J.L. Godwin, D.J. Millener, J.E. Purcell, C.G. Sheu, and H.R. Weller. Energy levels of light nuclei A=8,9,10. *Nuclear Physics A*, 745(3):155–362, 2004.

[143] O Castaños, JP Draayer, and Y Leschber. Shape variables and the shell model. *Zeitschrift für Physik A Atomic Nuclei*, 329(1):33–43, 1988.

[144] M. T. Mustonen, C. N. Gilbreth, Y. Alhassid, and G. F. Bertsch. Statistical theory of deformation distributions in nuclear spectra. *Phys. Rev. C*, 98:034317, Sep 2018.

[145] Konstantinos Kravvaris and Alexander Volya. Study of nuclear clustering from an ab initio perspective. *Phys. Rev. Lett.*, 119:062501, Aug 2017.

[146] Konstantinos Kravvaris, Sofia Quaglioni, Guillaume Hupin, and Petr Navratil. Ab initio framework for nuclear scattering and reactions induced by light projectiles. *arXiv preprint arXiv:2012.00228*, 2020.

[147] Serdar Elhatisari, Dean Lee, Gautam Rupak, Evgeny Epelbaum, Hermann Krebs, Timo A Lähde, Thomas Luu, and Ulf-G Meißner. Ab initio alpha–alpha scattering. *Nature*, 528(7580):111–114, 2015.

[148] E. K. Warburton. R-matrix analysis of the $\beta^{\mp}$-delayed alpha spectra from the decay of ^{8}Li and ^{8}B. *Phys. Rev. C*, 33:303–313, Jan 1986.

[149] Ian J Thompson and Filomena M Nunes. *Nuclear reactions for astrophysics: principles, calculation and applications of low-energy reactions*. Cambridge University Press, 2009.

[150] Yoshinori Akaishi. *Cluster models and other topics*. World Scientific, 1986.

[151] Kiyomi Ikeda, Toshio Marumori, Ryozo Tamagaki, and Hajime Tanaka. Chapter i. formation of the viewpoint, alpha-like four-body correlations and molecular aspects in nuclei. *Progress of Theoretical Physics Supplement*, 52:1–24, 1972.

[152] Hisashi Horiuchi. Generator Coordinate Treatment of Composite Particle Reaction and Molecule-like Structures. *Progress of Theoretical Physics*, 43(2):375–389, 02 1970.

[153] I. Brida, Steven C. Pieper, and R. B. Wiringa. Quantum monte carlo calculations of spectroscopic overlaps in $a \leqslant 7$ nuclei. *Phys. Rev. C*, 84:024319, Aug 2011.

[154] Sofia Quaglioni and Petr Navrátil. Ab Initio Many-Body Calculations of $n-^{3}$H, $n-^{4}$He, $p-^{3,4}$He, and $n-^{10}$Be Scattering. *Phys. Rev. Lett.*, 101:092501, Aug 2008.

[155] Sofia Quaglioni and Petr Navrátil. Ab initio many-body calculations of nucleon-nucleus scattering. *Phys. Rev. C*, 79:044606, Apr 2009.

[156] Simone Baroni, Petr Navrátil, and Sofia Quaglioni. Ab initio description of the exotic unbound ^{7}He nucleus. *Phys. Rev. Lett.*, 110:022505, Jan 2013.

[157] Pierre Descouvemont and D Baye. The r-matrix theory. *Reports on progress in physics*, 73(3):036301, 2010.

[158] Kenneth M. Nollett and R. B. Wiringa. Asymptotic normalization coefficients from ab initio calculations. *Phys. Rev. C*, 83:041001, Apr 2011.

[159] Petr Navrátil. Cluster form factor calculation in the ab initio no-core shell model. *Phys. Rev. C*, 70:054324, Nov 2004.

[160] Martin Asplund, David L Lambert, Poul Erik Nissen, Francesca Primas, and Verne V Smith. Lithium isotopic abundances in metal-poor halo stars. *The Astrophysical Journal*, 644(1):229, 2006.

[161] A. H. Wuosmaa, J. P. Schiffer, K. E. Rehm, J. P. Greene, D. J. Henderson, R. V. F. Janssens, C. L. Jiang, L. Jisonna, J. C. Lighthall, S. T. Marley, E. F. Moore, R. C. Pardo, N. Patel, M. Paul, D. Peterson, Steven C. Pieper, G. Savard, R. E. Segel, R. H. Siemssen, X. D. Tang, and R. B. Wiringa. Structure of ^{7}He by proton removal from ^{8}Li with the $(d, ^{3}\mathrm{He})$ reaction. *Phys. Rev. C*, 78:041302, Oct 2008.

[162] Su Jun, Li Zhi-Hong, Guo Bing, Bai Xi-Xiang, Li Zhi-Chang, Liu Jian-Cheng, Wang You-Bao, Lian Gang, Zeng Sheng, Wang Bao-Xiang, et al. Neutron spectroscopic factors of ^{7}Li and astrophysical ^{6}Li(n, γ)^{7}Li reaction rates. *Chinese Physics Letters*, 27(5):052101, 2010.

[163] T Kajino and RN Boyd. Production of the light elements in primordial nucleosynthesis. *The Astrophysical Journal*, 359:267–276, 1990.

[164] Thomas Rauscher, James H Applegate, John J Cowan, Friedrich-Karl Thielemann, and Michael Wiescher. Production of heavy elements in inhomogeneous cosmologies. *The Astrophysical Journal*, 429:499–530, 1994.

[165] J. P. Schiffer, G. C. Morrison, R. H. Siemssen, and B. Zeidman. Study of the (d, p) Reaction in the $1p$ Shell. *Phys. Rev.*, 164:1274–1284, Dec 1967.

[166] A. H. Wuosmaa, K. E. Rehm, J. P. Greene, D. J. Henderson, R. V. F. Janssens, C. L. Jiang, L. Jisonna, E. F. Moore, R. C. Pardo, M. Paul, D. Peterson, Steven C. Pieper, G. Savard, J. P. Schiffer, R. E. Segel, S. Sinha, X. Tang, and R. B. Wiringa. Neutron Spectroscopic Factors in ^{9}Li from $^{2}\mathrm{H}(^{8}\mathrm{Li}, p)^{9}\mathrm{Li}$. *Phys. Rev. Lett.*, 94:082502, Mar 2005.

[167] Robert J Schmidt. Xxxii. on the numerical solution of linear simultaneous equations by an iterative method. *The London, Edinburgh, and Dublin Philosophical Magazine and Journal of Science*, 32(214):369–383, 1941.

[168] IR Gulamov, AM Mukhamedzhanov, and GK Nie. Method for selecting peripheral reactions dominated by the pole mechanism: Analysis of (d, t) reactions on 1p-shell and 19 f nuclei. *Physics of Atomic Nuclei*, 58(10):1689–1695, 1995.

[169] L. Trache, A. Azhari, F. Carstoiu, H. L. Clark, C. A. Gagliardi, Y.-W. Lui, A. M. Mukhamedzhanov, X. Tang, N. Timofeyuk, and R. E. Tribble. Asymptotic normalization coefficients for $^{8}\mathrm{b} \overset{\rightarrow}{} ^{7}\mathrm{Be} + p$ from a study of $^{8}\mathrm{li} \overset{\rightarrow}{} ^{7}\mathrm{Li} + n$. *Phys. Rev. C*, 67:062801, Jun 2003.

[170] B. Guo, Z.H. Li, W.P. Liu, X.X. Bai, G. Lian, S.Q. Yan, B.X. Wang, S. Zeng, J. Su, and Y. Lu. The $^{8}\mathrm{Li}(d, p)^{9}\mathrm{Li}$ reaction and astrophysical $^{8}\mathrm{B}(p, \gamma)^{9}\mathrm{C}$ reaction rate. *Nuclear Physics A*, 761(1):162–172, 2005.

[171] AJ Koning and JP Delaroche. Local and global nucleon optical models from 1 keV to 200 MeV. *Nuclear Physics A*, 713(3-4):231–310, 2003.

[172] A. E. Lovell and F. M. Nunes. Constraining transfer cross sections using bayes' theorem. *Phys. Rev. C*, 97:064612, Jun 2018.

[173] E. A. Coello Pérez and T. Papenbrock. Effective field theory for nuclear vibrations with quantified uncertainties. *Phys. Rev. C*, 92:064309, Dec 2015.

[174] Sarah Wesolowski, Natalie Klco, RJ Furnstahl, DR Phillips, and A Thapaliya. Bayesian parameter estimation for effective field theories. *Journal of Physics G: Nuclear and Particle Physics*, 43(7):074001, 2016.

[175] J. A. Melendez, S. Wesolowski, and R. J. Furnstahl. Bayesian truncation errors in chiral effective field theory: Nucleon-nucleon observables. *Phys. Rev. C*, 96:024003, Aug 2017.

[176] N Schunck, JD McDonnell, D Higdon, J Sarich, and SM Wild. Uncertainty quantification and propagation in nuclear density functional theory. *The European Physical Journal A*, 51(12):1–14, 2015.

[177] Raditya Utama, Wei-Chia Chen, and Jorge Piekarewicz. Nuclear charge radii: density functional theory meets bayesian neural networks. *Journal of Physics G: Nuclear and Particle Physics*, 43(11):114002, 2016.

[178] N. Dudeck et al. Uncertainty quantification of *ab initio* based optical potentials through bayesian analysis. *Physical Review C*, In preparation, 2021.

[179] Jutta Escher. *Electron Scattering Studies in the Framework of the Symplectic Shell Model.* PhD thesis, Louisiana State University, 1997.

[180] M.E. Rose. *Elementary Theory of Angular Momentum.* John Wiley, New York, 1957.

[181] V. K. Khersonskii D. A. Varshalovich, A.N. Moskalev. *Quantum Theory of Angular Momentum.* World Scientific, 1988.

Vita

Grigor Sargsyan is a native of Yerevan, Armenia. He earned a bachelor's degree from Yerevan State University, majoring in physics. Always a fan of subatomic physics, he decided to pursue a doctorate in theoretical nuclear physics at LSU in the fall of 2015.